Tribosurface Interactions involving Particulate Media with DEM-calibrated Properties: Experiments and Modeling

Submitted in partial fulfillment of the requirements for

the degree of

Doctor of Philosophy

in

Mechanical Engineering

Prathamesh S. Desai

B.E., Civil Engineering, University of Mumbai
M.S., Computational Mechanics, Civil and Environmental Engineering, Carnegie Mellon University

Carnegie Mellon University
Pittsburgh, PA
December, 2017

To my grandparents

Abstract

While tribology involves the study of friction, wear, and lubrication of interacting surfaces, the tribosurfaces are the pair of surfaces in sliding contact with a fluid (or particulate) media between them. The ubiquitous nature of tribology is evident from the usage of its principles in all aspects of life, such as the friction promoting behavior of shoes on slippery water-lubricated walkways and tires on roadways to the wear of fingernails during filing or engine walls during operations. These tribosurface interfaces, due to the small length scales, are difficult to model for contact mechanics, fluid mechanics and particle dynamics, be it via theory, experiments or computations. Also, there is no simple constitutive law for a tribosurface with a particulate media. Thus, when trying to model such a tribosurface, there is a need to calibrate the particulate media against one or more property characterizing experiments. Such a calibrated media, which is the "virtual avatar" of the real particulate media, can then be used to provide predictions about its behavior in engineering applications. This thesis proposes and attempts to validate an approach that leverages experiments and modeling, which comprises of physics-based modeling and machine learning enabled surrogate modeling, to study particulate media in two key particle matrix industries: metal powder-bed additive manufacturing (in Part II), and energy resource rock drilling (in Part III).

The physics-based modeling framework developed in this thesis is called the Particle-Surface Tribology Analysis Code (P-STAC) and has the physics of particle dynamics, fluid mechanics and particle-fluid-structure interaction. The Computational Particle Dynamics (CPD) is solved by using the industry standard Discrete Element Method (DEM) and the Computational Fluid Dynamics (CFD) is solved by using finite difference discretization scheme based on Chorin's projection method and staggered grids. Particle-structure interactions are accounted for by using a state-of-the art Particle Tessellated Surface Interaction Scheme and the fluid-structure interaction is accounted for by using the Immersed Boundary Method (IBM). Surrogate modeling is carried out using back propagation neural network.

The tribosurface interactions encountered during the spreading step of the powder-bed additive manufacturing (AM) process which involve a sliding spreader (rolling and sliding for a roller) and particulate media consisting of metal AM powder, have been studied in Part II. To understand the constitutive behavior of metal AM powders, detailed rheometry experiments have been conducted in Chapter 5. CPD module of P-STAC is used to simulate the rheometry of an industry grade AM powder (100-250μm Ti-6Al-4V), to determine a calibrated virtual avatar of the real AM powder (Chapter 6). This monodispersed virtual avatar is used to perform virtual spreading on smooth and rough substrates in Chapter 7. The effect of polydispersity in DEM modeling is studied in Chapter 8. A polydispersed virtual avatar of the aforementioned AM powder has been observed to provide better validation against single layer spreading experiments than the monodispersed virtual avatar. This experimentally validated polydispersed virtual avatar has been used to perform a battery of spreading simulations covering the range of spreader speeds. Then a machine learning enabled surrogate model, using back propagation neural

network, has been trained to study the spreading results generated by P-STAC and provide much more data by performing regression. This surrogate model is used to generate spreading process maps linking the 3D printer inputs of spreader speeds to spread layer properties of roughness and porosity. Such maps (Chapters 7 and 8) can be used by a 3D-printer technician to determine the spreader speed setting which corresponds to the desired spread layer properties and has the maximum spread throughout.

The tribosurface interactions encountered during the drilling of energy resource rocks which involve a rotary and impacting contact of the drill bit with the rock formation in the presence of drilling fluids have been studied in Part III. This problem involves sliding surfaces with fluid (drilling mud) and particulate media (intact and drilled rock particles). Again, like the AM powder, the particulate media, viz. the rock formation being drilled into, does not have a simple and a well-defined constitutive law. An index test detailed in ASTM D 5731 can be used as a characterization test while trying to model a rock using bonded particle DEM. A model to generate weak concrete-like virtual rock which can be considered to be a mathematical representation of a sandstone has been introduced in Chapter 10. Benchtop drilling experiments have been carried out on two sandstones (Castlegate sandstone from the energy rich state of Texas and Crab Orchard sandstone from Tennessee) in Chapter 11. Virtual drilling has been carried out on the aforementioned weak concrete-like virtual rock. The rate of penetration (RoP) of the drill bit has been found to be directly proportional to the weight on bit (WoB). The drilling in dry conditions resulted in a higher RoP than the one which involved the use of water as the drilling fluid. P-SATC with the bonded DEM and CFD modules was able to predict both these findings but only qualitatively (Chapter 11).

Acknowledgements

"Whatever specialization you choose, try to be the best at it!", was the straightforward and simple, yet difficult to achieve, reply given by Dr. Hegde to an undergraduate me when approached for an advice on the research field to choose for a PhD.

My PhD journey at Carnegie Mellon University (CMU), beginning with a Master's program, has been nothing short of a major step towards trying to execute the advice given by Dr. Hegde. This humongous effort would have never been feasible without getting the support and guidance from the various quarters of the society, right from the very best teachers to extremely smart students to efficient support staff to my beloved family and friends. I would like to take this moment to express my gratitude to the people who have stood by me, individuals who have celebrated my highs and encouraged me during my lows over the period of this doctoral journey.

"The most important relationship that you will form during your PhD will be the one with your advisor", were the words of late Dr. Jeremiah Mpagazehe and as with most of his technical thoughts, this thought was absolutely correct. My PhD advisor, Prof. C. Fred Higgs III, has been like a fatherly advisor to me, guiding

me technically as well as philosophically, right from my pre-PhD internship with his Particle Flow and Tribology Lab (PFTL). Himself a perfectionist, Prof. Higgs pushed me to my very limits of technical knowledge and creative thinking, only for me to discover that I can go beyond the limits which I had created for myself. I will always be in awe of his work ethics and strive to implement that myself. He has nurtured my progress from a naive researcher to a clear-thinking scholar. The projects in this thesis were sponsored by the funds secured by Prof. Higgs from America Makes and Rice University. I was the last PhD student of Prof. Higgs at Carnegie Mellon University before he moved to Rice University.

Next I would like to acknowledge the past and present members of the PFTL family: Dr. John Shelton, Dr. Jonathan Sierra, Dr. Randyka Pudjoprawoto, Dr. Kristin Warren, Dr. Gagan Srivastava, Joshua Wagner, Jordan Wagner, Lynnora Grant and Funto Faweya, for their inputs during the weekly research meetings and feedback during mock presentations. In particular, I would like to thank late Dr. Jeremiah Mpagazehe for mentoring me during my initial days at the PFTL and showing me how to conduct research. His envisioned multi-purpose and multiphysics software Particle-Surface Tribology Analysis Code (P-STAC) has been the crux of this thesis. I hope, looking down, he is pleased at the developments contributed by this thesis to the P-STAC. I am especially thankful to the in-house powder expert, Dr. Patrick Dougherty, for his valuable training on powder rheometer. I would like to express my gratitude towards my friend and lab-mate Dr. Deepak Patil for helping me with a smooth transition from Pittsburgh to Houston during my research-related visits to the Rice University. I would like to acknowledge the help of Joshua Wagner with the drilling study. These acknowledgments would be incomplete without the mention of the BS and MS members of the PFTL family who

have assisted me on various projects. I would like to thank Wang Zhang and Akash Mehta for their help with GPU programming, Alec Merivs for his dedication towards the development of the heavy duty yet elegant GPU workstations (COBRA and MonGOOSE) which were envied by the non-PFTL CMU Mechanical Engineering students, Wentai Zhang for his assistance with Machine Learning, Natalie Kuang for her help with conducting experiments on powder rheometry and Nicholas Wolf for his every-willing nature to conduct experiments related to 3D printing and rock drilling. Other PFTL students who have assisted me include Gautham Nagaraju, Sanjay Adhikari, Gloriana Redendo, Jeffery Cole, Andrew Bouma and Emma Baker.

I would like to thank my thesis committee members: Prof. Jack Beuth, Prof. Shelley Anna and Prof. Anthony Rollett for providing valuable inputs and challenging me to develop a better and more sophisticated modeling framework. I would also like to thank Dr. Sandra DeVincent Wolf, researchers from Prof. Beuth's lab: Dr. Sneha Prabha Narra, Luke Scime, Brian and Colt Montgomery, and Prof. Rollet's PhD student Ross Cunningham, who were always available to provide succinct technical replies to my questions on metal additive manufacturing, be it via E-mail, over call or in-person. I would like to mention the contribution of Recep Onler and Iyabo Lawal for the profilometry scans of 3D printed objects.

I would like to thank the highly efficient support staff at CMU Mechanical Engineering comprising of Chris Hertz, Melissa Brown and Ginny Barry; Maxine Leffard, from Civil and Environmental Engineering, for helping me to sort out my graduate student responsibilities and purchase orders. Support staff at Rice University: Kacey Danner, Thea Heaviland and Mari Allen, has been equally helpful with the filing of research related purchase orders and reimbursements, during my visits to conduct research at Rice University.

On a personal front, I would like to thank Christine Frechard for hosting me in her beautiful abode, located in the scenic neighborhood of Highland Park. I would like to thank Christine's daughters, Sara and Lulan, for treating me as their beloved brother. While staying thousands of miles away from my hometown of Mumbai, I developed a special bond with the Frechards which helped me to never feel homesick.

A thumbs-up goes out to the unique set of friends I found at CMU: Muhammad, Sandeep, Argha, Jha, Agniv, Adi, Vaibhav and Ashesh. The many lunch breaks and poker nights we shared over different cuisines are one of my fondest Pittsburgh memories. I would like to thank Jingyi Zhang and Ms. Gu for their loving care, companionship and support during my MS and PhD days.

After my friends from America (as they call it in India), it is now the time to thank a strong group of friends I have back home, in India: Sion, Harshad, Deepak, Mukesh, JD, Mali and Kudchi. This is the group with whom I can restart a conversation which was dropped off months before. These brothers from different mothers, help me to feel secure about the wellbeing of my family, in India, if anything were to go wrong.

I would like to thank my extended-family members, who have now settled in the US, my uncle Dr. Milind Kunchur, aunt Dr. Varsha Kulkarni and cousin Caitlin, for providing me with a family blanket in the US and research ideas like the development of personalized workstations.

I would like to convey my heartfelt thanks to my loving sister Dr. Mrs. Prajakta Karkare for her never-settle-for-anything-less-than-what-you-can-achieve motivation. Coming from a middle-class family with both parents working, my paternal and maternal grandparents strove hard to provide me and my sister with uncon-

ditional love and care. They are always present in my thoughts. Finally, I would like to convey my love, respect and namaskar to my parents, Dr. Mrs. Pradnya Desai and Sanjay Desai, for their immense hard work, sacrifices and showering of bottomless love on me and my sister. They made sure that my sister and I got the best possible education and have always been supportive of most of our decisions.

The self-portrait in Fig. 1 comprises of the names of all the individuals who have contributed to who I am today.

Figure 1: Self-portrait of the author

Contents

List of Figures

List of Tables

Part I

Introduction and Research Philosophy

I spent all morning putting in a comma and all afternoon taking it out.
-Oscar Wilde

Chapter 1

Introduction

This chapter begins by introducing the meaning of tribology and the ubiquitous nature of tribological phenomena. A brief description of the paradoxical situation related to a tribosurface follows. Lastly the elephant in the room with respect to studying particle flow and tribology problems is introduced.

1.1 Meaning and Ubiquitous Nature of Tribology

Knowingly or unknowingly, each one of us makes use of the teachings of tribology. The computer or tablet or cellphone or paper on which you are reading this text is held in its place by using the principles of tribology. The tradition of filing our finger nails after clipping them displays one aspect of tribology. While the feeling of "Oh no, the time is up!" which many of us would have experienced when the puck of the air hockey table refuses to glide smoothly to our opponents goal slit, makes use of another aspect of tribology.

So, what is tribology?

Tribology is the study of friction (which helps to keep the computer on table or tablet, cellphone or paper, on which this text is displayed, in hand), wear (which is useful in case of filing of our fingernails to avoid the sharp corners after clipping them) and lubrication (which is offered by the thin air film on which the air hockey puck glides smoothly) of interacting surfaces [1]. The pair of such surfaces in sliding contact is referred to as the tribosurfaces and the these tribosurfaces together with the intervening media is referred to as the tribosystem [1].

Though seemingly easy to define, a mastery of tribology is necessary to tackle many important problems faced by mankind. To name a few, the design of artificial hip joints which can have lifetime comparable to the ones we are born with, chemical-mechanical polishing of silicon wafers for semiconductor industry and design of lubricious oils to decrease friction in an automobile all have tribology at their heart. Significant strides have been made over the last many decades to understand tribology from theoretical, experimental and computational perspectives [2–6] but the length scales of the interacting surfaces, which can have forced or unwanted particle entrapment, where the phenomenon of friction, wear and lubrication are to be studied are many orders of magnitude smaller than the length scale of the entire problem geometry and make the study of these phenomena challenging. These interfaces are notoriously difficult to model for contact mechanics, fluid mechanics and particle dynamics, be it via theory, experiments or computational models.

Therefore, it is important to continue the research in tribology.

1.2 *Catch-22* situation of the tribosurface interactions

As mentioned in the previous section, the length scale of the tribosurface interactions is many orders of magnitude smaller than the length scale of the entire problem geometry. While on one hand there is a need to understand almost all the physics occurring in the tribosurface, on the other hand it is mandatory to predict the influence of this physics on the net outcome of the entire problem in realistic times. The former can be achieved by developing a high fidelity theory or experiment or model while the later mandates an economical or scalable theory or experiment or model. Thus is the *catch-22* situation of the tribosurface interactions.

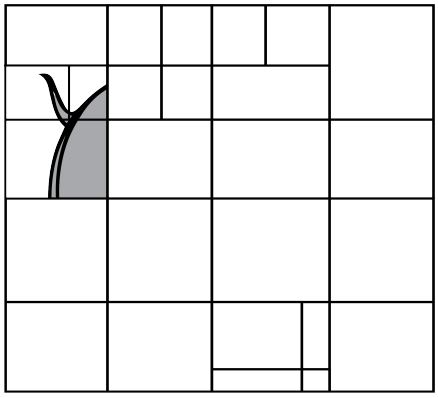

(a) Tail of the unknown animal

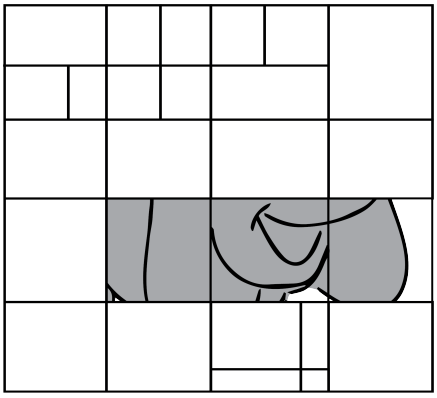

(b) Face of the unknown animal

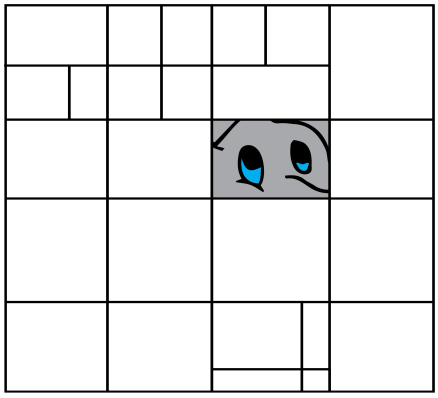

(c) Eyes of the unknown animal

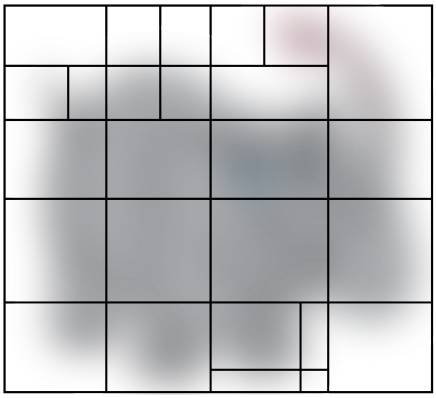

(d) The unknown animal from a far distance

Figure 1.1: Predicting the animal (a)-(c) By zooming in using a large magnifying glass or (d) By zooming out using a telescope

1.2.1 The game of prediction

Another way to understand this aforementioned catch-22 situation is by trying *to predict* the animal, shown in Fig. 1.1 and *guess* its age by using a very large magnifying glass to zoom-in and examine the tail, face and eyes of this unknown animal, shown in Fig. 1.1a through Fig. 1.1c or a telescope to zoom-out and look at the entire animal as shown in Fig. 1.1d.

Now, without turning over the pages:

1. Can you guess which animal is depicted in Fig. 1.1?

2. Is this a cub or a fully grown animal?

3. Do the anatomical parts depicted in Fig. 1.1a through Fig. 1.1c prove any less abstract than the entire blurred blob shown in Fig. 1.1d while you try to predict the animal?

The answers to the first question can vary from pig to puppy to cat to also a rhino while the answer to the second question is a definitive 'cub' and that for the third is a resounding NO.

However a better prediction for this unknown animal can be achieved by directing the very large magnifying glass at the anatomical features or *attributes* which best describe this animal, like the ones shown in Fig. 1.2. Now, you can immediately see that the unknown animal resembles an elephant. Yet there is a large chunk of information missing. We still can not guess the age of this elephant by only looking at attributes in Fig. 1.2. There is a need for some information from the previously explored less important attributes to completely answer the first two questions.

A superposition of the most important attributes, shown in Fig. 1.2, obtained by using a very large magnifying glass and the blurred, less important attributes, as shown in Fig. 1.1d, obtained by using a telescope, is the desired image which can answer the aforementioned first two questions. Such an image is shown in Fig. 1.3.

It is a baby elephant!

The aim of this thesis is to generate such an image where there is a balance between zoom-in and zoom-out. The different physics involved in a tribosurface

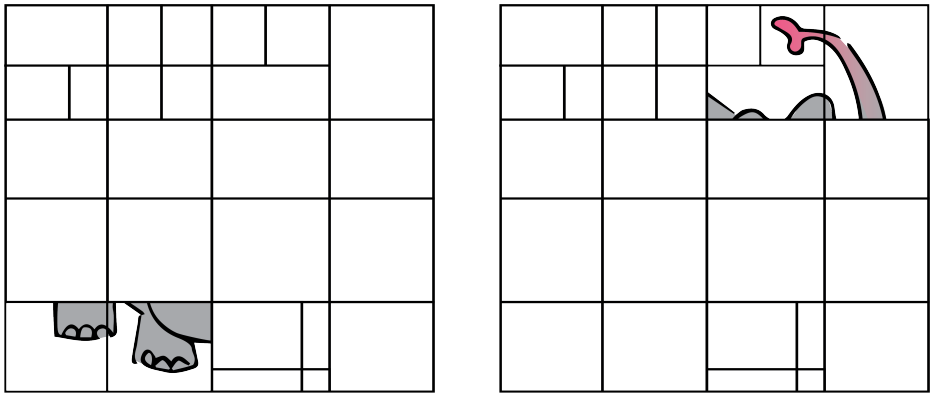

(a) Attribute #1 (b) Attribute #2

Figure 1.2: Predicting the animal by zooming in at the most imporatnat attributes using a *large magnifying glass*

are analogous to the different tiles which makeup the image of the baby elephant and the fidelity of this physics refers to the clarity of these image tiles.

1.3 Elephant in the room

A tribosystem involves *myriad phenomena or physics* of contact mechanics, fluid mechanics, particle mechanics and wear. Each of these phenomena involves *multiple attributes* which may or may not be important to the problem at hand.

One can develop a theory or model by accounting for all the attributes of all the phenomena. Then the theory or the model can be commanded to omit one attribute or the other to see its effect on the net outcome. Thus, an iterative approach can result in omission of all the less important attributes. Such an approach though logical and simple to state on paper requires tremendous effort from the developer of theory or a computational model. This approach can come to fruition in an ideal world with infinite time. Even if a model accounts for all the attributes, it might be

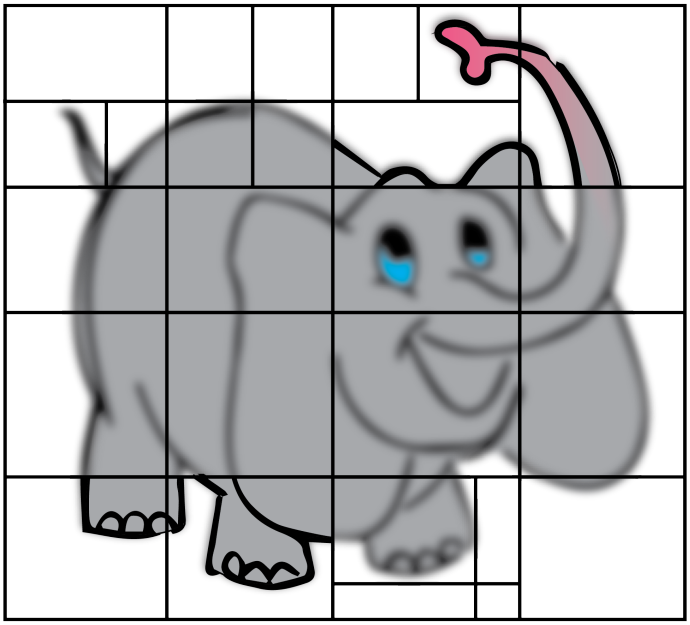

Figure 1.3: Desired balance between zoom-in and zoom-out to predict the animal

too slow, computationally, to provide any insights about the effect of tribosurface interactions on the entire problem geometry in realistic times. This case is the one in which you have all the tiles, including the tiles of less important anatomical parts, of the elephant image in Fig. 1.3 as crisp as possible and then you iteratively decay the resolution of tiles which makeup less important anatomical parts. However, in reality no such theory or model exists. But certainly there are theories or models which incorporate most of the attributes of one particular phenomenon, the crisp image tiles in Fig. 1.1a through Fig. 1.1c or Fig. 1.2, and can answer one or the other question, like name of animal or its age, but not both questions.

On the other end of spectrum, there can be a theory or model which simplifies almost all the phenomena and predicts the behavior of a tribosystem in concert with

the entire problem geometry in realistic times but in the same abstract manner as done by the earlier high-fidelity model. This case is the one depicted in Fig. 1.1d.

For example, if there are forced or unwanted debris particles in between a pair of surfaces in sliding contact, then these particles have the following attributes:

1. Particle size and its distribution
2. Particle shape and its roughness
3. Hydrophilic or hydrophobic nature of the particles
4. Magnetic and electrostatic response of the particles
5. Physical properties like density, hardness and elastic modulus
6. And so on...

But to study the effect of particles in a tribosystem, one need not account for all these attributes. In other words, all the attributes might not contribute in an equally weighted manner towards the effect of presence of particles in the tribosurface of interest. A trained tribologist might be able to discern the most important attributes, based on the nature of particles and forces these particles might experience, which should be accounted for while studying the effect of these particles in the tribosystem of interest.

Thus the elephant in the room is to try to find a balance between zoom-in and zoom-out or in other words, trying to answer the question:

Which physics *of the tribosurface interactions involving fluid/particulate media must be treated with* ***what level of fidelity*** *so as to provide engineering predictions about the net problem in realistic times?*

This thesis tries to find answers to the above question for two such tribosystems, one encountered in powder-bed metal additive manufacturing (Part II) and the

other related to energy resource rock drilling (Part III). Chapter 2 provides existing methodologies to study these two tribosystems. This is followed by Chapter 3 which lays down the research philosophy of the author to study the two aforementioned tribosystems.

Imagination is more important than knowledge.
-Albert Einstein

Chapter 2

Historical Review

As was seen in Chapter 1, there are many interesting problems to be explored using the knowledge of tribology but this thesis will be focused on two problems, one involving sliding surfaces or tribosurface interactions with intervening media comprising of metal powder particles and the other involving sliding surfaces with entrained rock particles immersed in fluids. The first problem is related to the powder-bed metal additive manufacturing (AM) while the second one is related to energy resource rock drilling. This chapter presents existing methodologies to study these problems and highlights the gap in literature which this thesis aims to fill.

2.1 Application #1: *Spreadability* of metal Additive Manufacturing (AM) powders

A literature tree listing works related to AM is shown in Fig. 2.1. Powder-bed Additive Manufacturing (AM), more commonly known as three - dimensional (3D) printing, involves repetitive spreading of metal powder and fusing or binding of

the spread layer until the entire geometry is 3D printed [7–9]. AM offers many advantages over the traditional manufacturing techniques of molding, casting and subtractive manufacturing like manufacturing of highly customized parts having intricate details and use of materials that maybe hazardous to use with traditional manufacturing techniques [10]. AM allows an engineer to rapidly manufacture the prototypes and check their functionality and feasibility. This truly gives the engineer the power to design and fabricate the creation in totality. Parts created using AM have found wide ranging applications like prosthetic implants and aerospace components. Creating parts through AM within acceptable tolerances for porosity, strength and roughness is contingent upon many process variables. One of these is the ability to spread layers of loose powder, with predetermined roughness, for a given thickness over a given coverage area under a given load, in other words the spreadability of metal powders. This is related to the "powder rheology" or the study of flow and spread of powders under a giving loading. Powders made of same material but having different morphology as well as those made up of different materials exhibit varying rheological behaviors [2, 11–15].

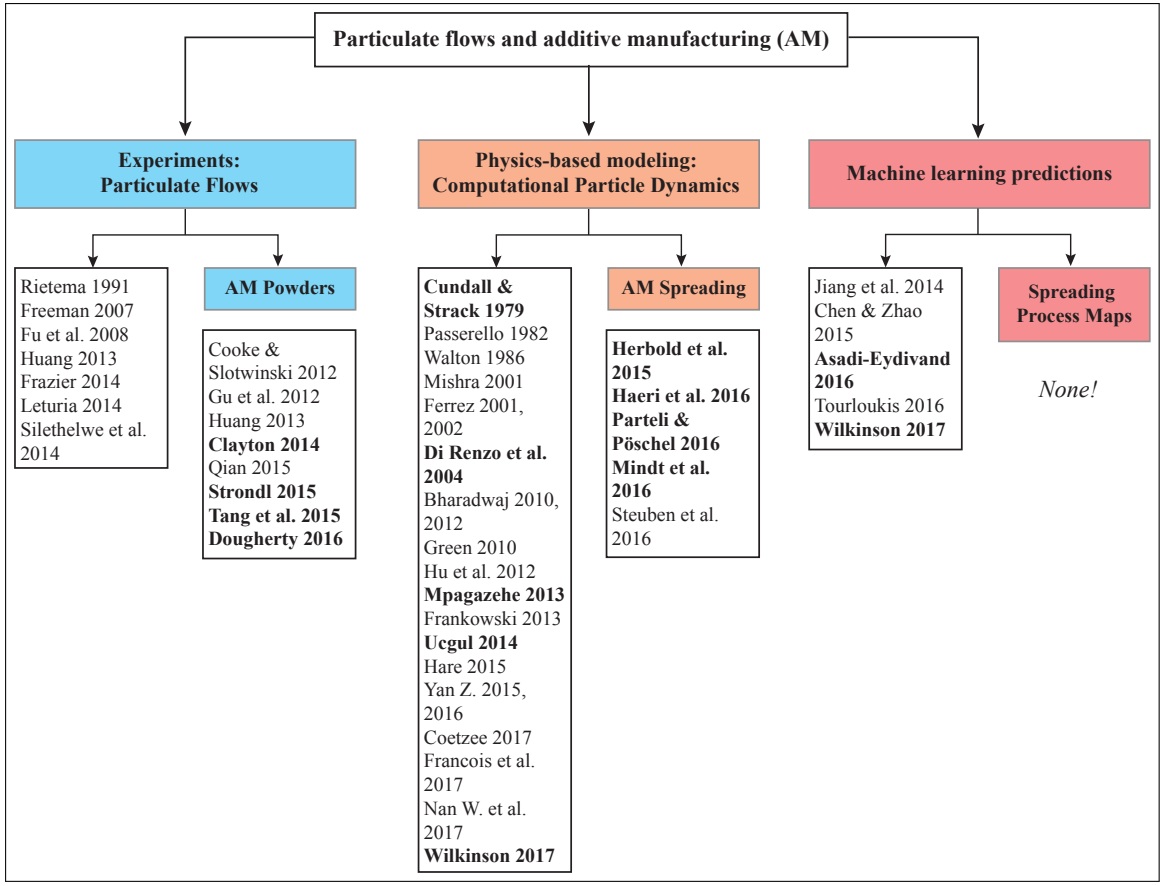

Figure 2.1: Literature tree showing relevant works on experiments, physics-based modeling and machine learning predictions for *spreadability* of metal AM powders

2.1.1 Experiments

Metal powders used in AM can range from 10's of μm to a few 100's of μm in size and can behave as a highly cohesive media comprising of clumps or a free-flowing fluid depending on the particle sizes, particle size distribution, nature of stress these powders experience and the packing efficiency [2, 11]. Powders exhibit complex behavior and characterizing the differences from powder to powder with respect to dynamic behavior of powders requires a sophisticated experimental equipment like a powder rheometer as opposed to a simple flow meter like Hall flow meter [10, 16, 17]. A lack of understanding of powder rheology forces the current 3D printer industry to print parts with a limited number of powders which require strict adherence with respect to particle size and particle size distribution. **A Freeman FT4 powder rheometer will be used in this thesis to characterize typical existing AM powders and also newer variants of these powders** obtained from different manufacturers. Such a rheometer has been extensively used in pharmaceutical and food industry [11, 12, 18] but only a few studies exist in the AM world [2, 9, 10, 19].

2.1.2 Physics-based modeling

The problem to study the spreadability of AM powders is twofold, firstly, it is difficult to study this problem experimentally inside a real 3D printer which often works in an inert atmosphere, due to the difficulty involved in characterizing the spread layer properties without interfering with the inert conditions. The safety issues associated with the handling of AM powders like toxicity, flammability and explosivity make a trial-and-error approach, common with experimental studies,

unrealistic and unsafe [20]. Secondly, a computational study of this problem is also not trivial as Discrete Element Method (DEM), developed by [21], which is most well suited among other computational techniques [22], is based on Lagrangian principles and has no simple constitutive laws for AM powders [18, 23–28]. The virtual powder must behave in ways similar to a real powder. This can be achieved by using a **simple linear spring-dashpot contact model**, as opposed to a computationally expensive non-linear contact model, provided there is a **robust calibration algorithm** [18, 23–26, 29]. In addition to there being no simple constitutive law, particle sizes for metal AM powders are in the orders of 10's of μm to a few 100's of μm while the build area is in the order of a few cm's. Thereby the number of DEM entities can easily reach millions. So, one of the aims of this thesis is to develop a **fast DEM solver by making use of GPU computing** [30]. Lastly, the previously built layer and the spreader geometry need to be represented accurately so that the layer spread using such a simulation can be safely assumed to have been caused by correct representation of the involved solid geometries. A state-of-the-art **Particle Tessellated Surface Interaction Scheme**, inspired from [31, 32] will be introduced in this thesis.

2.1.3 Machine Learning Predictions

Machine learning has two applications in DEM modeling of AM spreading process. Firstly, as done by Wilkinson et al. in 2017 [24], machine learning can be used to identify the parameters for which the bulk behavior of DEM entities is most sensitive to, in other words the principal components of a multi-dimensional DEM assembly. This approach, though highly effective in finding the most sensitive parameters in a DEM contact model, requires to carry out a lot of DEM runs to

ensure that a wide range of DEM parameters has been covered. This approach becomes computationally expensive while dealing with hundreds of thousands of particles. Wilkinson et al. in 2017 [24] used machine learning for generating virtual DEM medium and did not provide any experimental validation. Second use of machine learning is to relate the input parameters of a 3D printer to the resulting 3D printed part. This is a more useful application of machine learning than the first one as it can significantly reduce the number of experimental runs, numerical experiments or physical experiments, required to obtain process maps or parametric studies which can minutely cover the entire range of variables. Few studies [33–36] have made use of machine learning in this second way to provide predictions for non-metal 3D printers but the input data to the machine learning algorithm was obtained by performing real experiments. No study exists, till this point, which has tried **to generate spreading process maps for metal 3D printers**.

The above-mentioned studies, shown in the literature tree in Fig. 2.1, have tried to solve particle flow problems related to metal powders either via experimentation alone or machine learning based on experimentation. The latter solution cannot be used for metal 3D printers considering the difficulty in characterizing the spread layer experimentally with assured safety. No study exists which closes the loop from experimental validation to physics-based modeling and process map generation to study, and thereby improve, the *spreadability* of metal AM powders. Present thesis tries to solve this problem in Part II by applying the triadic formulation to be introduced in Chapter 3.

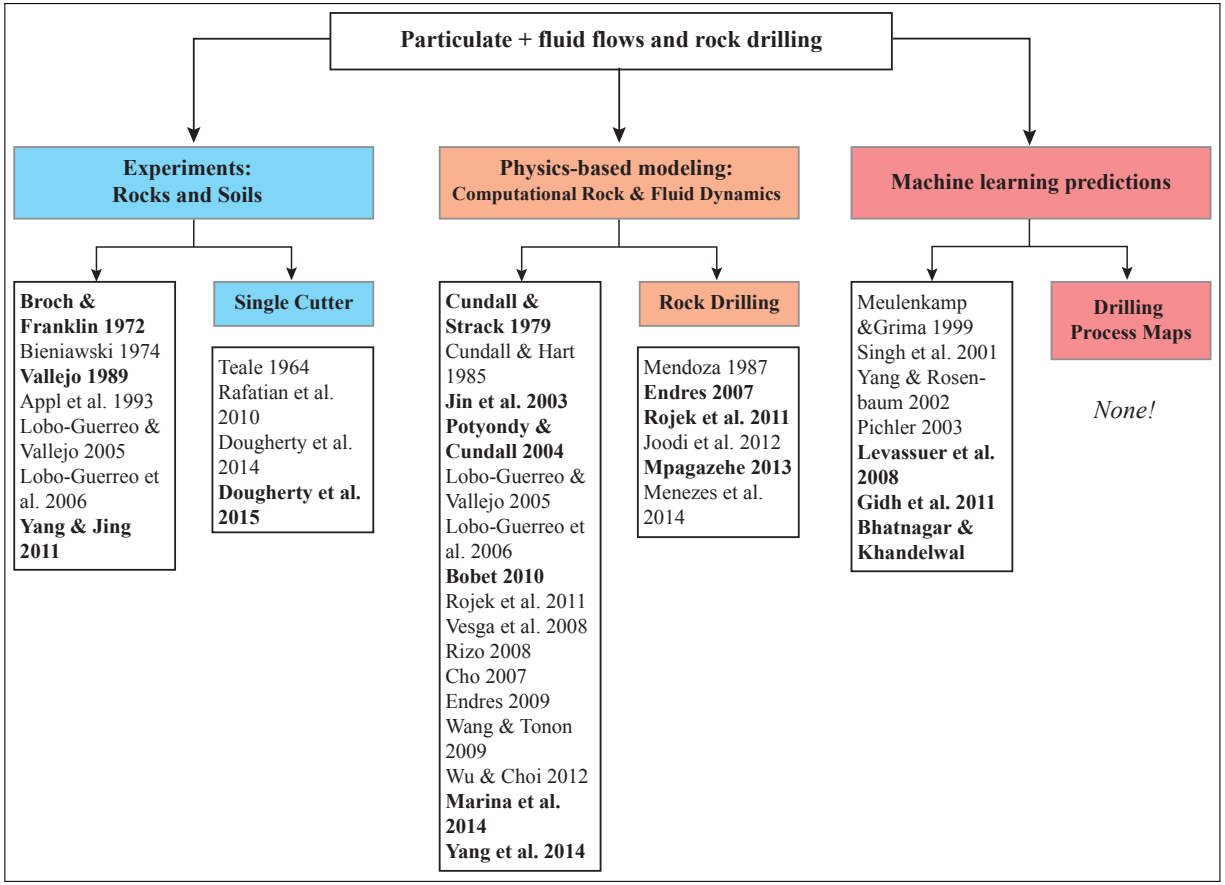

Figure 2.2: Literature tree showing relevant works on experiments, physics-based modeling and machine learning predictions for *sustainability* of cutters used in rock drilling

2.2 Application #2: *Sustainability* of cutters used in energy resource rock drilling

A literature tree listing works related to rock drilling is shown in Fig. 2.2. Over the last many years, petroleum companies have been trying to find ways to efficiently drill through the rocks to reach the fossil fuel rich geologic formations. In the present day, with the steep fall in oil prices, it becomes all the more relevant to optimize this rock drilling process. The energy rich geologic formations are usually located deep inside the earths crust and drilling a hole to reach these formations consumes significant portion, as high as 50%, of the entire crude oil extraction time [37], a practice which is prevalent in the petroleum industry, is exorbitantly high. Drilling action involves high impact between the drill bit and the rock formation and can result in the fracture of individual cutters which makeup the bit. If a significant number of cutters break mid-way to the drilling process, to reach the energy rich geologic formation, then the drill bit can no longer penetrate through the rock formation. This results in stalling of the drilling action and considerable time and money is lost in replacing the drill bit [37]. Thus, there is a need to optimize the drill bit's penetrating action which is controlled by the material composition of the bit, weight on the bit and revolutions per minute (rpms) of the bit, to drill to the energy rich geologic formation consuming the least amount of time. This optimization process is highly dependent on the rock formation which is being drilled into. The rock formations vary a lot based on geographical position of the oil well and even vary significantly with depth at any given well location, as is indicated by rock core sampling data [38]. In other words, there is no single, ‘strongest’ drill bit that can work best anywhere on the earth. There is a need to understand the wear mechanism

of both, rocks and cutters, and predict the lifetime of a bit comprising of these cutters, in other words the sustainability of cutters making up the drill bit.

2.2.1 Experiments

The present drill bit research is focused around drilling muds, vertical turret lathe testing of cutters and bit-on-rock tribometry [39–44]. While this is easy to perform, it is far from the real conditions seen by a drill bit which has a rotary action as opposed to the translation loading in a vertical turret lathe, very high weight on bit as opposed to bit-on-rock tribometry and occurs in a high temperature and high pressure subsurface environment. The wear of a bit caused directly by the rotary action should be considered in concert with the impacts of the drilled rock pieces as these are being carried out by the drilling fluids. This problem has a cutter-on-rock interface filled with drilling fluids and rock cuttings. This is a particle-fluid-structure interaction problem. This problem is rich in multi-physics covering tribological phenomena like three body wear and hydrodynamic lubrication, fracture mechanics of rocks and fluid mechanics and cooling efficiency of the drilling mud. Data from real oil wells can be analyzed for studying this multi-physics problem but experiments at the mega-scale of oil well are not practically and economically possible. No known experimental benchtop apparatus can provide insights into the real rock drilling problem. However, **a drilling simulator by Grace industries** comes very close to provide a picture of possible particle-fluid-structure interactions seen in rock drilling. This **benchtop drilling simulator will be used to conduct experiments on different types of rocks**, which can be characterized for strength and angle of crack propagation using known methods [45–48]. This study will use the widely prevalent data from rock characterization experiments like the point load

test, uniaxial compressive strength test and angle of crack propagation presented in literature [45, 46, 49, 50] and does not intend to conduct these experiments as opposed to aforementioned AM powder characterization study.

2.2.2 Physics-based modeling

Bobet in 2010 [51] provides a thorough review of the existing computational methods used to model rocks and soils. The cutter-and-rock interface has rock cuttings along with fluids which need to be accounted for. Rock cuttings can be better modeled by following a Lagrangian modeling approach [21, 52, 53]. Some researchers have tried using explicit finite element method to model the rock cuttings [54], but the unavailability of known simple constitutive law for different rock types makes this approach difficult to implement. While some researchers have modeled the crushability of rocks [55–57], mass and volume conservation of these crushable particles is not trivially possible. Most of the drilling simulation studies have focused on drilling action of a single cutter [55, 58] rather than the entire drill bit. Endres in 2007 [59] has proposed another continuum-like model for simulating rock drilling using an entire bit. The added complexity by usage of models based on continuum and introduction of crushable particles with nonlinear contact models in DEM does not provide any better predictions than simpler DEM models which make use of uncrushable particles having uniform size and which are bound together by weak concrete-like bonds, if a **robust calibration and validation process** is generated on the lines of that done in the problem of AM metal powder spreading. Such a model, when **optimized to work on a GPU**, will also be much faster than other complex models and will be able to capture the mega-scale of the problem while still modeling the tribological interface at the micro-scale. This thesis proposes

to develop a calibration process to generate virtual rocks in concert with machine learning to result in the formation of repository of virtual rocks. These rocks can then be made available to do virtual drilling similar to the one seen in a benchtop drilling simulator by incorporating drilling mud behavior via computational fluid dynamics [42, 60]. The **wear of drill bit** can be modeled and validated with the benchtop experimental findings. Only a few studies have modeled the physics of drilling fluid along with rock dynamics [4, 61]. Parametric charts can be generated using machine learning approach described below, based on a few physics-based simulations to optimize the wear and lifetime or *sustainability* of cutters.

2.2.3 Machine Learning Predictions

As in the case of the first problem on spreadability of metal AM powders, machine learning has two applications; a principal component analysis on the micro-properties in a DEM model to identify the most sensitive parameters which affect the formation of virtual rock and drilling predictions based on operational inputs to drill bit and outputs of drilling rates and wear of drill bit. The first application of machine learning, which has been carried out by [62–65], though computationally expensive is all the more relevant for drilling in rocks than in spreading metal powders as the rock formations change much more frequently, based on geographic location of a well and also with the depth of a well. This calls for a repository of virtual rocks which maps the micro-properties to bulk properties for various types of rock. The second application of machine learning for drilling process predictions has been seen in the past [66, 67] but required real drilling to provide the experimental data as input to a machine learning algorithm. This limits the use of power of machine learning in the sense that such an approach can only change the rotary action for a

drill bit which is already drilling on a site and not generate a rock-formation specific drill bit geometry which can be obtained by performing virtual drilling. The risk associated with the experiments - to - machine learning approach is a possible failure of a drill bit while drilling in newer rock formations. Pichler in 2003 [68] made predictions by assuming the rock formation to behave as a continuum. Treatment of rock as discrete medium is more realistic than continuum assumption [51].

The above-mentioned studies, shown in the literature tree in Fig. 2.2, have tried to solve particle flow problems related rock drilling either via experimentation alone or modeling alone or machine learning based on experimentation. The last solution cannot be safely and economically used for optimizing the drilling action of bit. No study exists which closes the loop from experimental validation to physics-based modeling and process map generation to study and thereby improve the sustainability of cutters used in rock drilling by **generating drilling process maps**. Present thesis proposes to solve this problem in Part III.

The scientists of today think deeply instead of clearly. One must be sane to think clearly, but one can think deeply and be quite insane.
-Nikola Tesla

Chapter 3

Research Philosophy

This chapter introduces the research philosophy to be followed in this thesis to solve the two problems introduced in Chapter 2.

3.1 The Triadic Formulation

The author of this work believes that with the availability of supercomputer-like computational power via GPU computing on a desktop level machine, it is possible to better model the sophisticated experiments, which are in turn made available by the advances in instrumentation, and conduct parametric studies to generate design guides regressed using machine learning to solve the particle flow and tribology problems in realistic times. This can be achieved by following what is referred to from hereon as the *triadic formulation*. The triadic formulation can be understood from the schematic structure shown in Fig. 3.1 and can be explained by answering the question:

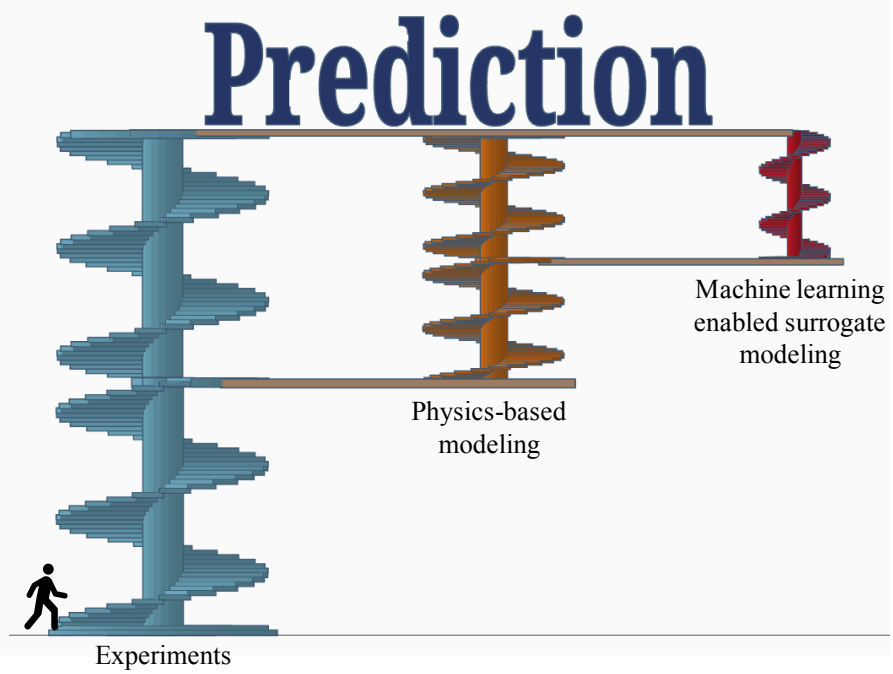

Figure 3.1: Pictorial diagram of the differences between three predictive approaches based on experiments, physics-based modeling and machine learning

"Which predictive approach (or a combination of one or more approaches)

must the stick-man follow ***to reach the desired prediction(s)****,*

located at the top of the structure, ***fastest****?"*

The blue staircase, in Fig. 3.1, represents experiments, the orange staircase represents the physics-based modeling and finally the red staircase represents the machine learning predictions. These staircases have decreasing helix diameters and thus are associated with decreasing times to climb a particular height. In general, experiments take the longest time followed by GPU accelerated physics-based modeling. The machine learning predictions are the fastest. Also, a point to be noted is the starting location of these staircases. The blue or 'experiments' staircase

begins from the base, the orange or the "physics-based simulations" staircase begins only after one climbs a certain height on the blue staircase. Similarly the fastest red or "machine learning predictions" staircase is available only after one climbs some height using the orange staircase.

There are three ways to reach the pinnacle of the structure. Firstly, the stick-man can reach the solutions at the top of the structure by taking experiments staircase all along but that will take a long time due to the fact that this staircase has the largest helical diameter. The first speed-up can be obtained by taking the bridge between the blue and the orange staircases and then continuing only on the orange staircase to reach the pinnacle. This though faster than the first way is still taxing when one knows that there is an additional speed-up possible if one takes the bridge between the orange and red staircases. So finally the third and fastest way to reach the top is to make use of the red staircase following the blue and orange ones. This fastest way from blue-to-orange-to-red-to-top is the triadic formulation proposed in this research and elaborated in details in subsequent sections. This triadic formulation is applied to study tribosurface interactions involving particulate media related to *spreadability* of metal AM powders (Part II) and *sustainability* of cutters used in energy resource rock drilling (Part III).

Thus the three main ingredients of the triadic formulation are:

1. Experiments
2. Physics-based modeling
3. Machine learning enabled surrogate modeling

A work flow showing the usage of triadic formulation to study any tribosurface interactions involving particulate media is shown in Fig. 3.2. The three ingredients

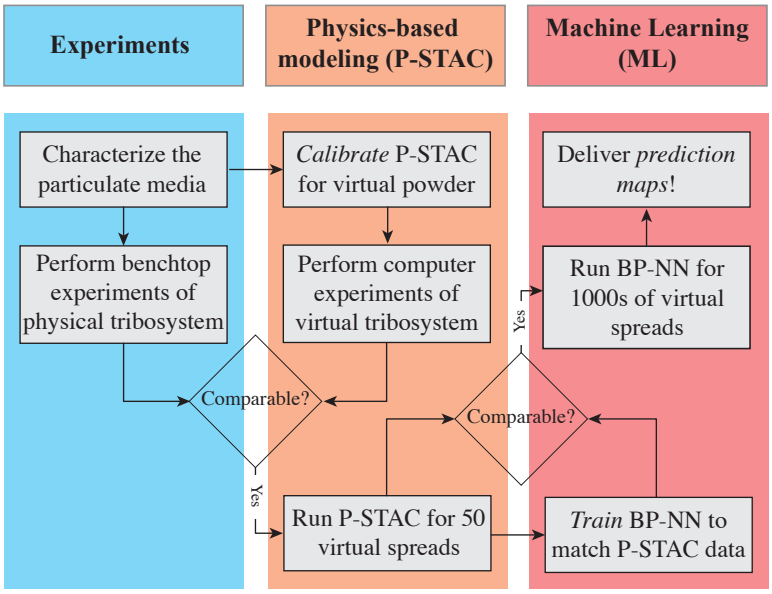

Figure 3.2: The triadic formulation as applied to study the tribosurface interactions involving particulate media

are shown in the same blue, orange and red colored blocks respectively as were the three staircases shown Fig. 3.1.

3.2 Experiments

Most often than not, it is difficult to conduct experiments in the real settings and at real scales involved in spreading of metal powders in AM (micro-scale) and wear of dill bits used to drill into rocks for energy purposes (mega-scale). The trial-and-error approach, associated with most of the experimental studies, cannot be used to study these problems as any failure of the system, AM printer or drilling rig, can be injurious or even fatal and highly expensive. This approach also has the biggest overburden of time associated with it. Alternatively, benchtop experiments which

mimic the physics seen in these problems can be conducted to provide insights about the problem at hand. The benchtop experimental rigs used in these two problems are a powder rheometer and a drilling simulator respectively and are described in Parts II and III respectively. Such benchtop experimental rigs provide following advantages:

1. Relatively quick, safe and simple usage when compared to conducting the experiments at real scales, micro-scale for problem #1 and mega-scale for problem #2

2. The results from these rigs serve dual nature, one to provide insights into the physics which might occur in the real problems and second, these serve as a validation platform for a physics-based computational model.

A computational model validated on these benchtop rigs can future be used to study the real problem at real scales, micro or mega.

3.3 Physics-based modeling

Broadly, computational mechanics models can be divided into two types, continuum based Eulerian models and discrete models based on Lagrangian principles. Each modeling technique has its own advantages and disadvantages with respect to the assumptions and computational efficiency. In general, continuum models are faster and discrete element models are slower [42]. Each class of models are better suited for a particular class of problems. While some problems require a hybrid modeling approach making use of both Eulerian and Lagrangian modeling to simulate different physics involved.

3.3.1 Lagrangian modeling

In this modeling approach, the individual components making up the medium or system are modeled as separate entities and solved for their motion using the Newton's second law of motion:

$$\sum \underline{F} = m\underline{a} \tag{3.1}$$

Here, $\underline{F}$ is any force (body or surface) acting on an entity which has a mass m. The resulting acceleration of the entity is given by $\underline{a}$.

If the discrete entities are modeled at the atomic level or in other words if the discrete entities are atoms, then this modeling is referred to as Molecular Dynamics. If the entities are modeled as particles whose sizes can vary from a few hundred microns to a few centimeters, then this modeling is referred to as Particle Dynamics.

3.3.2 Eulerian modeling

This modeling approach is based on the assumption of continuum. This modeling approach works at a macroscopic level where it can be safely assumed that the number of atoms making up the medium at hand, a gas or liquid or solid, is large enough to treat the medium to be a continuum. The number of these atoms is based on the mean free path and the characteristic length of the medium. In a continuum, say for fluids, the macroscopic properties such as fluid pressure and fluid velocity change in a uniform fashion and can be calculated by solving conservation of mass and momentum equations as given below:

$$\nabla \cdot \underline{V} = 0 \tag{3.2}$$

$$\rho \frac{D\underline{V}}{Dt} = \nabla \cdot \underline{\underline{\sigma}} + \underline{f} \tag{3.3}$$

Here, $\underline{V}$ is the fluid velocity field, ρ is the fluid density, $\underline{\underline{\sigma}}$ is the fluid stress tensor and $\underline{f}$ is the body force vector.

3.3.3 Hybrid modeling

For solving the complex physics involved in the particle flow and tribology problems, a hybrid modeling approach, combining Eulerian and Lagrangian modeling, is used in this research [4]. Lagrangian modeling is used to model the particle flows using discrete element method as proposed by Cundall & Strack in 1979 [21]. This Computational Particle Dynamics (CPD) scheme has been applied to study the problem of *spreadability* of metal AM powders. Then continuum modeling is used to simulate the fluid flows by solving the 3D Navier Stokes equations using finite difference discretization schemes as done in [60]. This Computational Fluid Dynamics (CFD) scheme is used to study the physics of drilling fluids. CFD in concert with CPD for rocks [52, 53] is used to study the problem of *sustainability* of cutters used in rock drilling for energy purposes.

This CPD-CFD model, in totality, is the in-house multi-purpose, multi-physics software called **Particle-Surface Tribology Analysis Code (P-STAC)**. P-STAC involves solving high-fidelity physics which is often accompanied by exceptionally high computational times. One way around this is to make simplifying assumptions and solve for simplified physics as done by Srivastava in 2015 [5]. Another option is to make the high-fidelity physics modeling computationally efficient by utilizing parallel computing for CPD and mesh refinement for CFD. In this research,

GPU-based parallelization has been employed by using Compute Unified Device Architecture (CUDA) developed by nVIDIA. The challenges, computational or otherwise, associated with this modeling scheme are described in details in the subsequent chapters.

3.4 Machine learning enabled surrogate modeling

In the triadic formulation, the last speed up to obtain the prediction maps, shown in the red block in Fig. 3.2 is obtained by using machine learning enabled surrogate modeling. In particular, back-propagation neural networks [69] are used as regression tools to regress between the highly non-linear data generated using the physics-based modeling. This avoids having to run the physics-based model over a larger set of parameter values and thereby saves considerable time in obtaining the process maps which can be made available to the system operators, a 3D printer operator or a drill rig operator, for each of the two problems.

Thus is the research methodology, philosophized as a triadic formulation, based on experiments, physics-based modeling and machine learning predictions.

Part II

Application #1:

Spreadability of metal additive manufacturing (AM) powders

An expert knows all the answers - if you ask the right questions.
-Levis Strauss

Chapter 4

Introduction to Powder Spreadability

Part II is based on the invention disclosure: Higgs, C. F., and Desai P. S., *A Rheometry-Validated Model for predicting Spreading Process Maps in Powder-Bed Additive Manufacturing (AM) Techniques*.

The technology of powder-bed Additive Manufacturing (AM), more commonly known as "three-dimensional (3D) printing", has been evolving rapidly over the last few years. The rise of mass-customization through the deployment of AM technologies is promising a landscape where parts can be produced faster, cheaper, yet while expending less energy and wasting less resources. AM consists of the technologies that produce parts or components, slice by slice, by spreading a layer of the desired material in powder form and using different techniques to bind the powder together into a solid, cohesive, 3D final form. Unfortunately, the lack of understanding of the powder spreading process leads to a very limited selection of powder

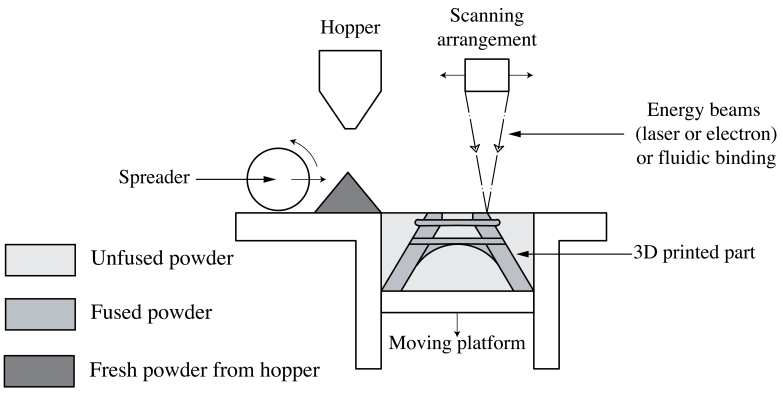

Figure 4.1: Schematic of powder-based AM

materials used to make parts, part defects due to non-uniform layers and porosity, and highly empirical process tuning which is costly and time-consuming. The final solutions often feature slow 'printing' speeds and machine default spreading values.

In powder-bed AM, there are two key overall steps: (i) the spreading step where a heap of powder is pushed across a plate in order to spread a thin powder layer, and (ii) the binding step, where the powder particles are selectively bound through a beam-based (laser or electron beam) fusion process or a fluidic binding process. A schematic of metal powder-based AM process is shown in Fig. 4.1. At first, the powder is discharged from the hopper, then a spreader is used to spread it in a fine layer. This is followed by the fusion or the binding process using the scanning arrangement (refer Fig. 4.1). The moving platform then descends by a distance equal to a single powder layer thickness and the process is repeated until the entire geometry is 3D printed [9]. For example, Fig.4.1 shows a geometry of Eiffel Tower being 3D printed. Most additive manufacturing (AM) research is aimed at the second step, powder binding, effectively declaring the powder spreading step to be perfect or ideal. However, the powder spreading step is far from ideal and is often

the central cause to two powder layer defects: varying heights (or high roughness) and high porosity.

Referring to the terminology introduced in Section 1.3, Figure 4.2 shows an exploded view of all the attributes of all the phenomena or physics of contact mechanics, particle mechanics and fluid mechanics which can be encountered while trying to understand the powder's *flowability* or the ability to flow under gravimetric loading (e.q., delivery of powder from the hopper) and *spreadability* or the ability of an AM powder to spread under a giving load (e.g., the confined loading of the AM powder in front of the spreader). The particle mechanics attributes of shape, hydrophilic or hydrophobic behavior, specific energy (to be introduced in Chapter 5) and fluid mechanics attributes like aeration ability of powder particles or the ease at which the powder particles can enter the airflow of a room, are important during the powder delivery step.

Then during the spreading step, as can be seen in the side and top views of layer *i*, particle mechanics attributes like particle roughness, particle size distribution, particle cohesion and electro-magnetic behavior of the powder particles can be of significance to understand the spread layer roughness and layer porosity or partial coverage.

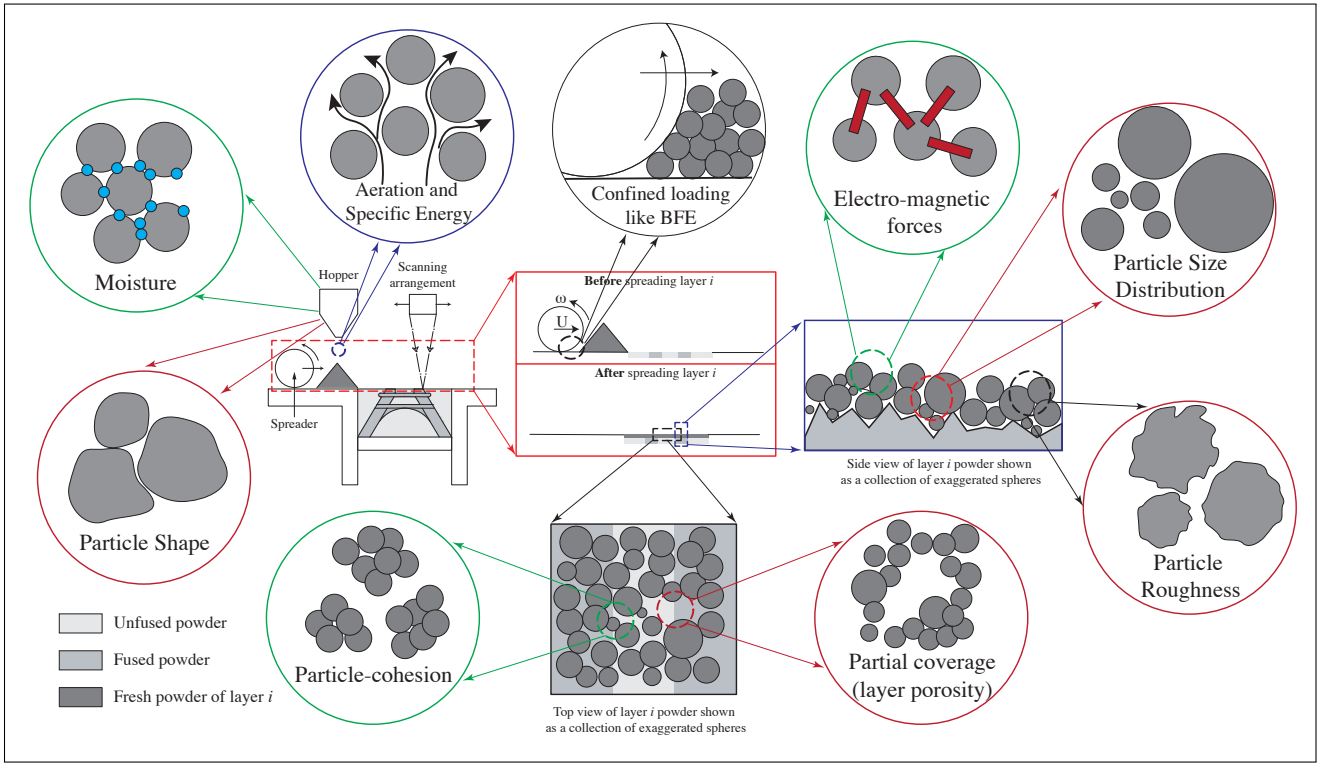

Figure 4.2: Multi-physics involved in *flowability* and *spreadability* of metal AM powders

Contact mechanics which occurs between the trapped particles of layer *i* while these interact with the spreader and the previously spread-and-fused layer, is highly sensitive to the true geometry of spreader and the previously spread-and-fused layer *(i-1)*. In other words, it is mandatory to account for the true roughness of the previously spread-and-fused layer, shown as peaks and valleys in the rectangular inset (in Fig. 4.2) showing the side view of layer *i* with exaggerated spheres. This roughness of the spread-and-fused layer is of the order of particle sizes and should not be excluded while trying to model the spreading step.

A theory or model which accounts for all the attributes shown in the Fig. 4.2 does not exist in literature. The multiphysics of this tribosystem is analogous to the different tiles which made up the baby elephant of Fig. 1.3 and the inclusion or approximation of the attributes, shown in circles or bubbles in Fig. 4.2, is analogous to the clarity of the tiles making up the aforementioned baby elephant. The aim is to answer questions about the roughness and porosity of the spread layer (question about guessing the animal name in Section 1.2.1) and the throughput of the spread (question about predicting the animal age in Section 1.2.1) in the least amount of time.

To this effect, a closed-loop, synergistic solution combining experiments and modeling, which comprises of physics-based modeling and machine learning enabled surrogate modeling, is proposed in this thesis to obtain spreading process maps relating the spreader shape, the spreader speeds, the height of the spreader from the substrate and the roughness of the substrate to the roughness and the porosity of the spread layer and the volume of powder spread per unit time per unit width of the spreader. The latter is an indicator of 'printing' speed or throughput. Such spreading process maps can widely increase the capabilities of AM printers to

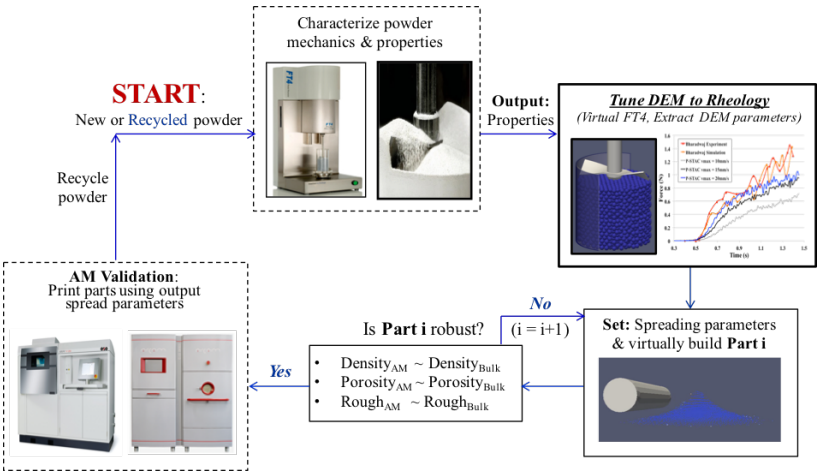

Figure 4.3: Process flow to study the *spreadability* of metal AM powders

print parts with desired properties using existing or newer powders. These maps can also serve the function of purposely introducing roughness in the spread layer to offset the uneven temperature distribution which is often encountered in the electron or laser beam based binding processes and thereby result in a smooth and uniform build or 3D printed layer.

Figure 4.3 shows the process flow to study the *spreadability* of metal AM powders. The metal AM powder is characterized for its rheology by using a powder rheometer. Chapter 5 describes the experimental investigations associated with metal AM powders. Chapter 6 describes the one to one physics-based modeling of the powder rheometer and calibration of particulate media properties. Chapter 7 uses virtual spreading and machine learning to predict the *spreadability* of metal AM powders and delivers sample spreading process maps. Finally, the effect of polydispersity in modeled AM powder is considered in Chapter 8 and virtual single layer spreading is validated against single layer spreading experiments. A spreading process map displaying hybrid layer properties is delivered at the end of Chapter 8.

Any product that needs a manual to work is broken.
-Elon Musk

Chapter 5

Experiments on Powder Rheometry to measure Powder Properties

A similar version of this chapter appears in the final America Makes report 4028.001 A Database Relating Powder Properties to Process Outcomes for Direct Metal AM submitted by Jack Beuth, Anthony Rollett, Fred Higgs, Sandra DeVincent Wolf, Luke Scime, Ross Cunningham, Prathamesh Desai in March 2017.

Abstract

The technology of powder-bed Additive Manufacturing (AM), more commonly known as “three-dimensional (3D) printing”, has been evolving rapidly over the last few years. Due to the complex nature of powders, there are only a few powders, having a strict morphology control, which are used in the current state-of-the-art 3D printers thereby limiting the use of this technology. Creating parts through additive manufacturing within acceptable tolerances for porosity, strength and roughness is contingent upon many process variables. One of these is the ability to spread layers of loose powder, with predetermined roughness of spread layer, for a given thickness over a given coverage area. This is related to the “powder rheology” or the study of flow and spread of powders under a giving loading. This project involves the measurement of powder properties and relating these measured powder properties to the ability to use these powders with direct metal AM machines (EOS and Arcam). An FT4 powder rheometer which can measure a wide range of flow, shear and bulk properties of powders is employed in this study to characterize 7 Ti-6Al-4V powders and 1 IN718 powder. Such a characterization is helpful to better understand the behavior of existing powders in 3D printers and also check the usability of newer powders in existing 3D printers.

Nomenclature

Term	Symbol	Meaning
Additive Manufacturing	AM	ASTM definition: Process of joining materials to make objects from 3D model data [7]
Flow energy (mJ)		Work done by all the forces acting on a rheometer blade as it displaces the powder
Angle of helix (°)	α	Angle from horizontal along which the blade moves
Downward testing		Recording the test data as the blade moves along the helical path from the top to the bottom of the cylindrical test vessel
Upward testing		Recording the test data as the blade moves along the helical path from the bottom to the top of the cylindrical test vessel
Conditioning		Gentle disturbance of the powder sample to ensure uniform packing prior to any test by using a slicing helical motion of blade from top to bottom and lifting helical motion from bottom to top of cylindrical test vessel
Basic Flowability Energy (mJ)	BFE	The energy needed to displace a conditioned powder sample during downward testing at specific consolidation conditions
Specific Energy (mJ/g)	SE	The energy per gram needed to displace conditioned powder during upwards testing using a -5° helix
Stability Index	SI	The factor by which the measured flow energy changes during repeated testing or processing
Flow Rate Index	FRI	The factor by which the flow energy is changed when the flow rate (blade tip speed) is reduced by a factor of 10
Aeration Energy	AE	Flow energy at maximum airflow rate of 10mm/s through the powder bulk
Aeration Ratio	AR	The ratio of BFE to AE
Conditioned Bulk Density (g/mL)	CBD	Bulk density of a conditioned powder sample
Cohesion		Shear strength at zero normal stress
Angle of internal friction (°)	AIF	Angle between the axis of normal stress and the tangent to the yield locus
Angle of wall friction (°)		The arctan of the ratio of the wall shear stress to the wall normal stress
Compressibility percentage		Change in the volume of powder bulk after compression under normal stress of 15kPa, expressed in percentage

5.1 Introduction

Powder-bed Additive Manufacturing (AM), more commonly known as three-dimensional (3D) printing, involves repetitive spreading of metal powder and fusing or binding of the spread layer until the entire geometry is 3D printed [7–9]. AM offers lots of advantages over the traditional manufacturing techniques of molding, casting and subtractive manufacturing like manufacturing of highly customized parts having intricate details and use of materials that maybe hazardous to use with traditional manufacturing techniques [10]. Parts created using AM have found wide ranging applications like prosthetic implants and aerospace components. Creating parts through AM within acceptable tolerances for porosity, strength and roughness is contingent upon many process variables. One of these is the ability to spread layers of loose powder, with predetermined roughness, for a given thickness over a given coverage area. This is related to the "powder rheology" or the study of flow and spread of powders under a giving loading. Powders made of same material but having different morphology as well as those made up of different materials exhibit varying rheological behaviors [2, 11–14].

Powder properties breakdown into two types- *static and dynamic (flow) properties*. *Static properties* include particle size, shape and statistical distribution of particle sizes in powder lots. Static properties can affect both powder spreading and powder fusion steps in direct metal AM. *Dynamic or flow properties* relate specifically to how easily AM powders flow, with relevance to the ability to effectively spread powder over the top of the part surface. Maintaining powder 'spreadability', the ability of AM powder to spread under a given load, is central to the goal of allowing a larger range of powder types to be used in direct metal AM machines.

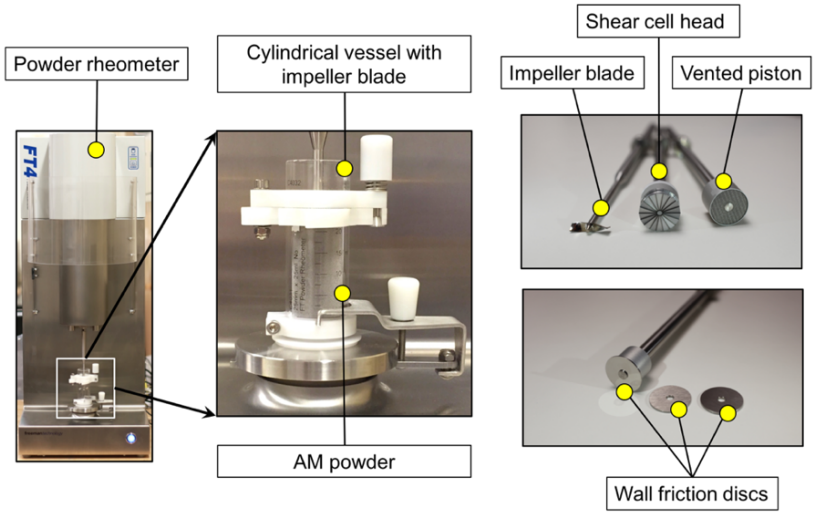

Figure 5.1: Freeman FT4 Powder Rheometer and the associated accessories

The goal of this project is to relate fundamental powder flow properties to powder spreading behavior in state-of-the-art 3D printers by EOS and Arcam.

5.2 Methodology

This project employs a Freeman Technologies FT4 powder rheometer [11, 12, 15, 17], shown in Fig. 5.1, to measure AM powder flow properties. The FT4 has the widest range of capabilities among current commercially available powder rheometers. The machine itself has seen extensive use for powder characterization in a wide array of industries in which powder flow is a prime concern such as powder metallurgy, pharmaceuticals, and food processing [15, 22]. This machine has several advantages over simpler devices such as the Hall flow meter, [10], in that it has the ability for highly precise *in situ* data capture, and the ability to impose a variety of different stress states. This last advantage is crucial for capturing data

relevant to AM, as powders will behave very differently under different stress states, and a hall flow meter test in which simple gravimetric flow is monitored may not be enough to describe the variety of flows in the AM process [10, 16]. For example, the flow of powder under the action of a spreader blade (or roller) is an essential feature of all powder bed systems and the flow of powder under this circumstance is a confined flow, not a free flow as measured by the Hall flow meter.

It is the aim of this work to carry out extensive testing on the available powder systems (PSs) with regards to the following:

1. Flow properties (Section 5.3)
    (a) Measurement of Basic Flowability Energy (BFE) and Specific Energy (SE): Flow properties of AM powders under downward and upward testing respectively
    (b) Aeration testing: Flow energy of AM powders under compressive stress at varying air flow rates
2. Shear properties (Section 5.4)
    (a) Shear and wall-friction testing
3. Bulk properties (Section 5.5)
    (a) Compressibility of AM powders

The following sections describe the methodology, results and relevance of the test results to the AM process for the above-mentioned tests for all the available PSs listed in Table 5.1. Except for PS 7 all other PSs are Ti-6Al-4V powders having different morphologies. PS 7 is IN718 alloy

Table 5.1: Range of particle sizes in μm for different PSs

PS 0	PS 1	PS 2	PS 3	PS 4	PS 5	PS 7	PS 8
45-105	50-80	100-250	<88	44-74	44-105	<88	<63

5.3 Flow properties

5.3.1 Measurement of Bulk Flowability Energy (BFE) and Specific Energy (SE): Flow Properties of AM powders under Compressive and Unconfined Stress States

Methodology

This test involves the motion of a precision blade, shown in Fig. 5.1 as impeller blade, through a cylindrically shaped powder container to measure the flow resistance of the powder. There are two distinct blade motions involved, one called downward testing (blade's downward helical motion) which causes the powder to flow under a confined compressive stress state and the other called upward testing (blade's upward helical motion) which causes the powder to flow under an unconfined stress state.

The first motion imposes a confined, compressive stress state using a constant blade tip speed of 100mm/s as the blade is forced downward into the powder bed. The average energy required to induce powder flow over seven tests, is reported as the Basic Flowability Energy (BFE). This provides a measure of how well the powder flows given a stress state similar to what it will experience under an AM spreading mechanism which entrains powder into the gap between itself and the existing powder bed. The second motion, in which the impeller blade moves upward through the powder bulk, imposes an unconfined stress state while the powder is allowed to flow freely over the blade. The average energy requirement over the sixth and seventh test, normalized by weight, is recorded as the Specific Energy (SE). This provides a measure of how the powder will flow in low stress environments

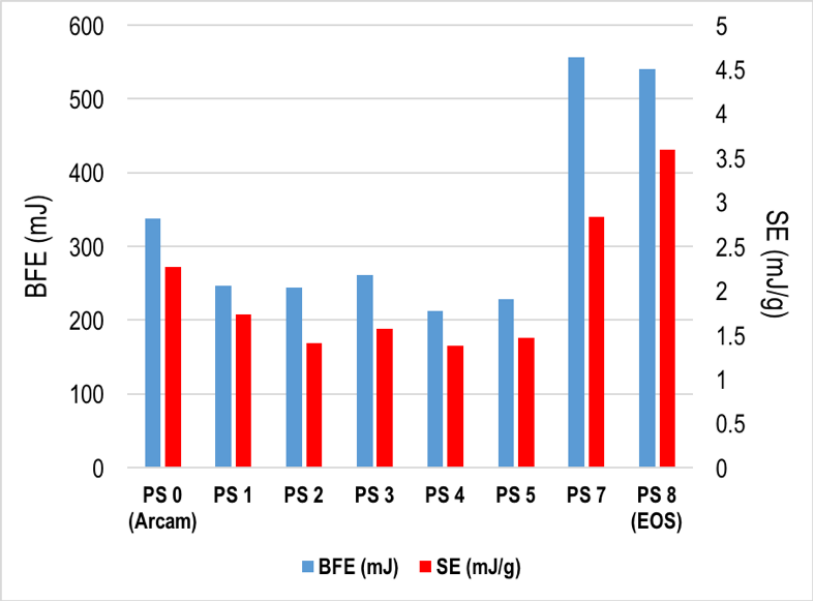

Figure 5.2: BFE and SE for different PSs

such as a hopper delivery system.

Results

Figure 5.2 displays the rheological behavior of all available AM PSs using a Freeman FT4 powder rheometer with two distinct blade motions. BFE values are shown with blue bars and SE values are shown in red bars. Shown in the Table 5.1 are particle sizes for the different PSs in μm. It can be seen that the rheological behavior of all PSs is different from one another. PS 0 is the Arcam standard and PS 8 is the EOS standard. PSs 0, 1 and 2 were to be used in Arcam machine while others were to be used in EOS machine.

Relevance to AM

From the results in Fig. 5.2, it can be seen that IN718 (PS 7) and EOS (PS 8) powders, for use in a direct laser sintering machine, exhibited BFE values 1.5-2 times greater than the other PSs. More specifically, PS 7 was the most reluctant to flow with a BFE of about 560mJ. It can be seen that the Arcam standard powder (PS 0) required significantly less energy to produce flow when compared to PS 7 and 8 but still more than PSs 1 and 2. PSs 1 and 2 had larger mean particles size than PS 0. The increased BFE for PS 7 can be attributed to the presence of lots of fines and irregular shaped particles (as seen in the SEM image for PS 7 or PREP, Fig. 47 in [2]). In addition, it should be noted that there is a distinct difference between the morphology of the EOS powder compared to the other powder systems. There were a larger number of fines (small particles), as well as a large number of satellites and irregular particles in the EOS powder, which increased friction and thereby the BFE. Because there was an increase in particle size, as well as sphericity, there was a much larger decrease in resistance to flow in both states in moving from the EOS and PS 7 to the other powder systems. This is an important feature of rheological characterization as it allows us to pre-screen powder from a new manufacturer for comparison to already printable and established powders. It should be noted that the transition from PS 1 to PS 2 featured a very large increase in average particle size. While this did not affect flowability under the spreader (similar BFE values), it was found to still have an effect on flowability in a hopper-like state displayed by the least SE value for PS 2. This was actually found to be crucial for builds as PS 2 proved to be so flowable in the hopper discharge that it required a redesign of the Arcam system hopper before successful builds could be undertaken.

However, it proved possible to maintain spreading parameters at similar levels as long as the average particle size was taken into account in setting the layer thickness. This is another example of the potential for pre-screening of new powders using an FT4. Given adequate characterization, powders that are too flowable could be pre-emptively designed for or avoided before use on a machine.

These types of detailed flow analyses are possible if a sophisticated rheometer is used. Hall flow meter which captures only the free flow of powders under gravity might not be able to capture these powder flow trends. More importantly, solely relying on the results from a Hall flow meter test can be misleading as seen in the Hall flow meter studies conducted at North Carolina State University and elaborated in "A Database Relating Powder Properties to Process Outcomes for Direct Metal AM" (America Makes report 4028.001).

5.3.2 Aeration testing: Flow energy of AM powders under compressive stress at varying air flow rates

Methodology

Because AM systems take place under a variety of environments, with differing levels of potential fluidization, it is important to study the effect of differing air flow rates on each powder. In this test, the powder flow energy is measured in a way similar to the BFE measurement described in the previous section, but with differing levels of air flow through the base of the powder bulk. The aeration base unit, which is a porous disc allowing for the air to flow through the powder bulk, replaces the white disc at the base of "cylindrical vessel with impeller blade" shown in Fig. 5.1. As the air flow increases, the air can act as a lubricant between particles,

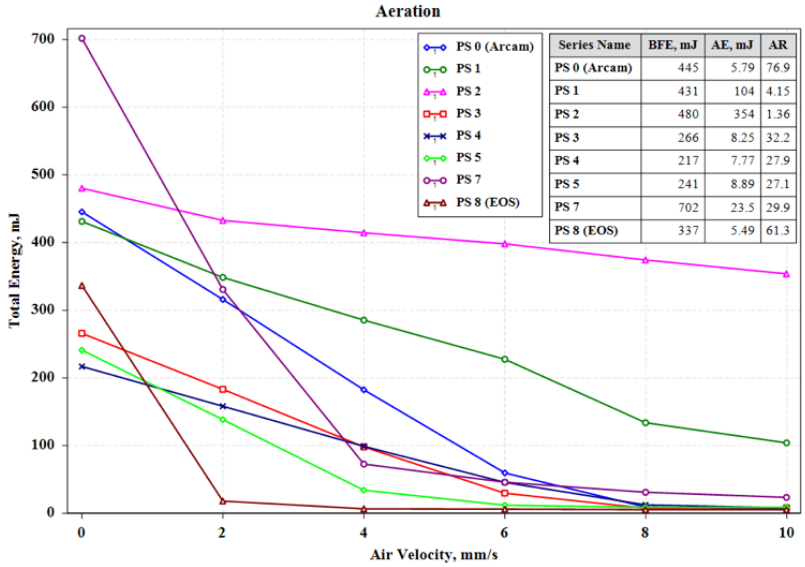

Figure 5.3: BFE under aerated conditions for different PSs

reducing cohesive forces throughout the bulk. At a certain point, the powder may become fully fluidized, such that cohesive forces are reduced to effectively zero.

Results

Figure 5.3 presents the flow energy results of all available PSs under varying air levels. Flow energy at zero air flow is BFE. Flow energy at maximum airflow of 10mm/s is referred to as the Aeration Energy (AE). The ratio of BFE to AE is called aeration ratio (AR). BFE, AE and AR values for different PSs are shown in the table inside the plot of Fig. 4. Also, to remind the reader of the particle sizes of these PSs, Table 5.1 shows the range of particle diameters in μm. The EOS standard PS (PS 8) shows drastic effect of air flow on the flow energy, in that the fluidization occurs at air flow of only 2mm/s. Among all the Ti-6Al-4V PSs, PS 8 is the one with least sized particles. As all the Ti-6Al-4V PSs have similar density, PS 8 has lightest

particles thereby the easy aeration. Other Ti-6Al-4V PSs seem to be relatively less fluidizable. PS 7 shows flow energy trends similar to PS 8. The reason can be attributed to the presence of lots of fines in this powder.

Relevance to AM

The importance of this testing methodology is for the usage of powders under different environmental conditions. This can exist in both AM machines which do not require vacuum, as well as those with delivery systems which are exposed to the air or which use air to enhance flow into the build area. For printers with ambient environments (i.e. infiltration or air), powders will flow far easier in situations with potential air flow such as at high spreading speeds, where air may be entrained into the bulk as well as in delivery systems utilizing air flow. This test also throws light on the minimum air speeds required to make these PSs behave like a fluid. PS 8 can easily enter the ambient room air if it is fluidized (which is easy as it can get fluidized at air speeds of just 2mm/s) and can thereby be a severe health hazard [20]. Necessary precautions must be taken at all the stages of printing parts with these PSs.

5.4 Shear properties

5.4.1 Shear and wall-friction testing

Methodology

It is important to understand the frictional behavior of AM PSs. There are two types of friction coefficient involved: particle-particle and particle-wall. Particle-particle

friction coefficient controls the inter-particle frictional behavior in a PS while the particle-wall friction coefficient controls the frictional behavior of PS along the hopper wall, spreader surfaces and previously 3D printed substrate. FT4 rheometer has a shear cell module to study the particle-particle frictional behavior and cohesion in a PS. This rheometer also has a customizable wall friction module to study the particle-wall frictional behavior. Both these modules involve exposing the powder bulk in a cylindrical vessel to normal and shear stresses. The shear stress required to cause the failure of the powder bed held at a predetermined normal stress is measured. This is repeated at varying normal stress values and a failure envelope is noted on a normal stress vs. shear stress plot. The blade used in the shear testing and the discs with varying roughness used for the wall-friction testing are shown in Fig. 5.1. The wall-friction discs can be fabricated of material and roughness similar to that of the hopper wall and the spreader surface. To mimic the previously 3D printed substrate over which the new powder is spread inside a real 3D printer, these discs can also be 3D printed.

Results

Figure 5.4 presents the failure envelops for all the available PSs obtained using the shear cell. The values of the cohesion, which is the intercept of the failure envelop curve (line) on the shear stress axis and the angle of internal friction (AIF), which is the angle formed by the failure envelop curve (line) with the normal stress axis are show in the table inside the plot of Fig. 5.4. PS 7 exhibits maximum cohesion and AIF. The tan(AIF) is the powder particle-particle coefficient of friction. Similar plots can be obtained from the wall-friction test.

Due to the non-availability of discs made of the material similar to and having

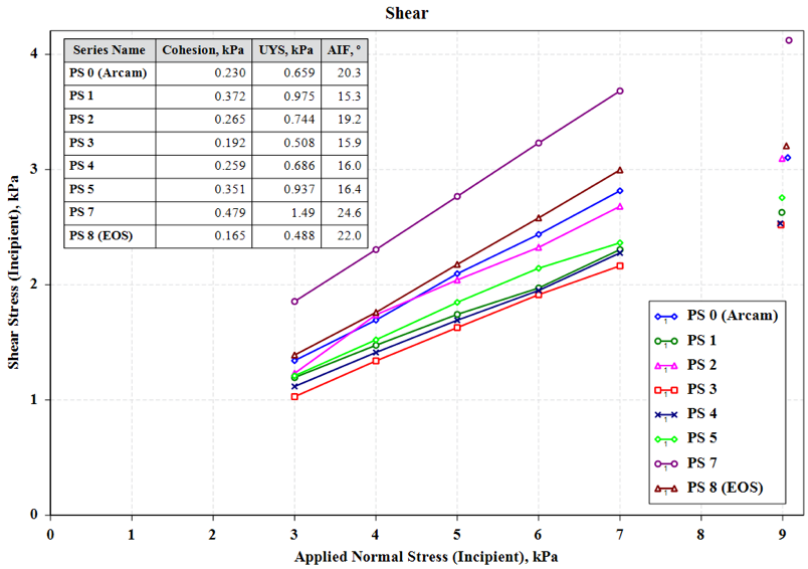

Figure 5.4: Shear testing on different PSs

roughness equal to the spreader of EOS or Arcam, wall friction results, which are quite similar to the aforementioned shear cell results, are not shown.

Relevance to AM

PSs which have larger cohesion and larger AIF values, will require more energy to spread under a spreader and will also be less flowable under gravity. The friction coefficient values obtained from these tests can be used in computational models like the Discrete Element Method (DEM) which are based on Lagrangian principles [21].

5.5 Bulk properties

5.5.1 Compressibility of AM powders

Methodology

Compressibility is defined as the percentage change in the volume of powder after compression. It is a measure of the change in density as a function of the applied normal stress. While compressibility might not be directly related to the flowability of powders, it can give insights about the particle size distribution, cohesion, particle shape and particle surface texture. The test involves compressing cylindrical powder bulk using a vented piston, shown in Fig. 5.1, to a normal stress of 15kPa and measuring the change in volume of the powder bulk. The vented piston, as seen in Fig. 5.1, has a compression face which is constructed from a woven stainless steel mesh and allows the entrained air in the powder to escape uniformly across the surface of the powder bed.

Results

Compressibility percentage (CP) and conditioned bulk density (CBD) for different PSs are shown as blue and red bars respectively in Fig. 5.5. PS 7 has the maximum compressibility indicating the presence of highly cohesive, irregularly shaped particles. On the other hand EOS standard powder (PS 8) exhibited least compressibility. This PS is followed by PS 3. A point to be noted here is that PS 8 used for this test comprised of the powder left over after multiple usage in 3D printed unlike the one for BFE and SE tests which was almost a virgin powder. The low compressibility indicates the presence of nice spherical particles, having a

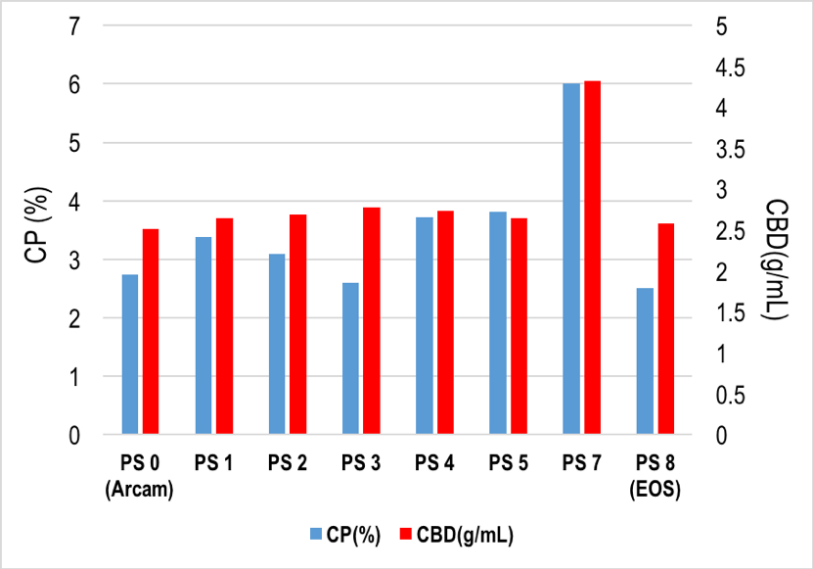

Figure 5.5: Compressibility percentage (CP) and conditioned bulk density (CBD) for different PSs

more uniform size distribution as opposed to virgin EOS powder which has lots of fines. The repeated usage of PS 8 in the 3D printer might have caused the frictional polishing of the powder and loss (used in the 3D printed part) of finer sized particles. Similar results about flowability of reused metal powders were obtained by [19] and the reason mentioned was loss of fines, emergence of a tighter particle size distribution and removal of moisture from the powder due to repeated exposure to high temperatures. CBD of all the Ti64 PSs (all but PS 7) is comparable.

Relevance to AM

Powders stored in a hopper are subject to compressive stresses under self-weight and knowledge of compressibility can help in the design of hoppers. A higher compressibility is an indication of cohesive powder with irregular shaped particles

with a larger spread in particle size distribution. On the other hand, a low compressibility is an indication of well-packed powder which can comprise of uniform sized, spherical particles.

5.6 Conclusions

To conclude, the present state of AM industry is marred by a very limited set of metal powders requiring very specific particle size distribution. The parts printed using these powders are rough from outside and porous from inside. One way to improve the present state of AM parts is to understand the rheology of existing powders and introduce newer, cheaper alternatives for the present AM powders. This involves studying the behavior of AM powders under different stress conditions. An extensive characterization of flow, shear and bulk properties was carried out on metal powders which are used in current state-of-the-art 3D printers (PS 0 and PS 8) along with newer powders which relax the restrictions of particle morphology and materials and might serve as alternatives for the existing PSs. FT4 powder rheometer was used to conduct experiments covering flow, shear and bulk properties of powders. Powders having same chemical composition (Ti-6Al-4V PSs) behave quite differently from one another, based on their morphology. Powders having different chemical composition (IN718 and Ti-6Al-4V) might behave similar based on their morphology and loading state. Powders having lots of fines and smaller particles sizes (PS 7 and PS 8) exhibited maximum resistance to stress states akin to hopper discharge and spreader due to more cohesive forces and agglomerations. These powders were also the most compressible ones. Powders with larger particle sizes and more spherical particles exhibited low flow energy in states akin to hopper

and spreader (PS 2). PS 3 exhibited the least compressibility mostly due to the absence of agglomerates and well packed state due to uniform particle sizes. Among all the Ti-6Al-4V PSs, the one with least sized particles (PS 8) and thereby lightest particles, is the one which can be easily fluidized and therefore easy to cause hazardous effects. Lastly PSs with larger AIF can be thought of being most resistive to spread due to higher friction values. The AIF and wall friction coefficient values can be used as input parameters in DEM models to develop computational tools to study the spreadability of these powders. All in all, a rheology based characterization can help to provide valuable insights about the behavior of metal powders inside hopper and spreader used in powder-bed AM machines.

Acknowledgements

Authors of this work would like to acknowledge the efforts of Ms. Natalie Kuang and Mr. Wentai Zhang from the research group of Prof. Higgs for assisting with the experiments in this study at Carnegie Mellon University (CMU).

The artist sees what others only catch a glimpse of.
-Leonardo da Vinci

Chapter 6

Modeling Powder Rheometry to determine Calibrated Powder Properties

A similar version of this chapter is prepared for the following journal publication: Desai, P. S., Mehta A., Dougherty P., and Higgs III, C. F., *A powder rheometry based DEM-calibration approach to study the spreadability of metal additive manufacturing (AM) powders.*

Abstract

The technology of metal powder-based Additive Manufacturing (AM) has been evolving rapidly over the last few years. Creating parts through additive manufacturing within acceptable tolerances for porosity, strength and roughness is contingent upon many process variables. One important factor is the ability to spread uniform layers of loose powder for a given thickness over a given coverage area. This is related to the "powder rheology" or the study of flow or shear motion of powders; it sometimes occurs under a given load. As in the case of spreading which is essentially a shear flow under a load, in this work, a benchtop powder rheometer with the capabilities to study bulk flow performance of AM powders is utilized to characterize metal powders. When used in tandem with powder dynamics modeling, the rheometer can provide the powder rheological parameters to quantify 'spreadability' or the ability of an AM powder to spread under a given load. Powder dynamics modeling can simulate powder spreading and capture powder layer quality descriptions such as segregation, porosity and surface roughness. This study is therefore directed towards modeling bulk powder performance and powder dynamics by using the Discrete Element Method (DEM). This work aims to experimentally validate the model against powder rheometer experiments and make the calibrated media, which is the "virtual avatar" of the real powder, available to study the 'spreadability' of AM powders. The model compares well with published results for a benchmark granular media (2mm glass beads) and in-house experiments on a well-known AM powder (100-250μm AM Ti-6Al-4V). CPU-based serial computing is used for modeling around 8000 2mm glass beads and subsequently, significantly faster GPU-based parallel computing is used to model 1.3 million 250μm Ti-6Al-4V powder.

Nomenclature

Symbol	Meaning
K	Stiffness of the spring in a spring-dashpot system
β	Damping of dashpot in a spring-dashpot system
n, t	Subscripts: normal and tangential directions respectively
ε	Coefficient of restitution
pp, pv, pi	Subscripts: Collisions occurring between a particle (p) and another particle (p), cylindrical vessel (v) or impeller blade (i) respectively
m	Particle mass
V	Particle speed
Δ	Overlap of a particle with another particle or geometry
ϕ	Diameter of a spherical particle
μ	Coefficient of sliding friction
$\underline{e_t}$	Unit vector along the tangential direction
F	Force magnitude
T	Torque magnitude
E	Energy consumed by impeller blade of rheometer
h	Height traveled by impeller blade of rheometer
α	Angle of helix generated by the motion of impeller blade of rheometer
η	Height of impeller blade of rheometer
R	Radius of impeller blade of rheometer
H	Fill height or the height up to which the cylindrical vessel of rheometer is filled with the granular or powder media

6.1 Introduction

The technology of metal powder-based Additive Manufacturing (AM), more commonly known as 3D printing, has been evolving rapidly over the last few years. Metal powder-based AM involves layer-by-layer spreading of a metallic powder and binding these layers to produce the required geometry [9]. Depending on the binding process, powder-based AM can be broadly divided into two categories: Energy Beam (laser or electron) or binder jetting [7, 9, 70]. A schematic of a metal powder-based AM process is shown in Fig. 4.1. At first, the powder is discharged from the hopper, then a spreader is used to spread it in a fine layer. This is followed by the fusion or binding process using the scanning arrangement (refer Fig. 4.1). The moving platform then descends by a distance equal to a single powder layer thickness and the process is repeated until the entire geometry is 3D printed. For example, Fig.4.1 shows a geometry of Eiffel Tower being 3D printed. Each step (i.e., spreading, binding, actuation, etc.) in the metal powder-based AM continues to be an on-going research sub-field. Various studies are being carried out to bridge the knowledge-gap between the process parameters and the final 3D printed product [71, 72].

One of the areas bottlenecking mass scale production using 3D printers is the uniform spreading of powder layer by layer. In order to control this parameter, it is essential to understand the powder delivery process which is carried out using a hopper and the powder spreading process which is carried out using a roller or a spreader (Fig. 4.1). Elucidating the flow or spread of powders is greatly aided by studying the *rheology* of powder. Powder rheology is the study of the flowing and

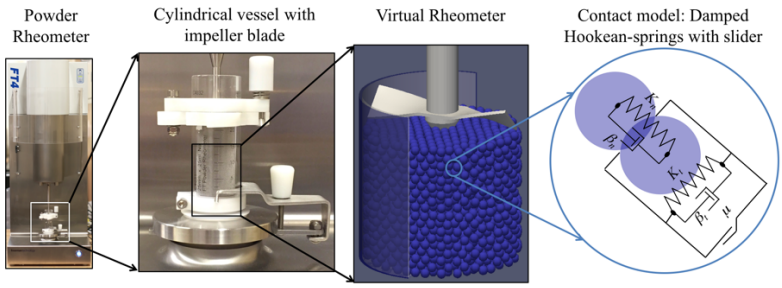

Figure 6.1: The Powder Rheometer Set-up: A Progression from the real, physical experiments to virtual experiments

spreading of powders under a giving loading. A benchtop powder rheometer (shown in Fig. 6.1) with the capabilities to study this dynamic flow of powder [9, 11] is used in this study.

The authors define powder flowability as the ease with which a powder will flow under a set of operating conditions. Normally flow of powders within internal geometries (e.g., hoppers, tubes, silos). Powder spreadability is the ease with which a powder will spread under a set of load conditions. Powders are normally spread within a sliding or rolling contact, such as underneath a roller or shearing foot.

Though powder rheology can be studied experimentally, it is difficult to experimentally study the actual powder spreading problem encountered in AM. Therefore, the authors of this paper have chosen a computational modeling approach based on experimental validation as a step towards understanding the problem of powder spreading. The discrete element method (DEM), pioneered by Cundall [21], which involves the Lagrangian principles as opposed to continuum modeling based on the Eulerian approach, best suits the problem at hand [18, 22, 23]. Only a few studies [18, 22–26] related to the DEM modeling of the powder rheometer have been reported in the literature. None of these has been in the area of AM where the

particle sizes are of the order of 10-300μm with around 1.3 million particles. This study, therefore aims to develop a fast, first-order DEM model (Section 6.2) along with a robust DEM calibration process (Section 6.3) to replicate the bulk behavior of a granular medium (2mm glass beads) and a finer commercial grade AM powder (250μm Ti-6Al-4V) in the powder rheometer. The granular medium [18] had mono-sized glass beads while the AM powder had particle sizes from 100-250μm. An SEM image of this powder can be seen in Fig. 48 in [2] (or reproduced in this thesis in Fig. 7.2c) named as 'Starmet'. This Starmet powder consists of nice, smooth, spherical particles and thus can be modeled as a collection of spherical particles using DEM. This experimentally-validated model (Section 6.4) can then be extended to solve the actual problem of powder spreading in AM.

6.2 Methodology

6.2.1 The Discrete Element Method (DEM)

The authors have developed an in-house multiphysics computational modeling platform known as the **Particle-Surface Tribology Analysis Code (P-STAC)**, which has a DEM module as its particle dynamics simulation tool. The DEM, originally developed by Cundall [21], and more recently described by Mpagazehe [4] is used in this study. A general algorithm for a DEM solver can be found elsewhere in the literature [18, 22, 73, 74]. In a nutshell, DEM treats the powder media to be made up of distinct particle elements and makes use of Newton's second law of motion to determine the changes within the media by considering the forces acting on each entity. These forces can be body forces such as gravity and surface forces such as element-element interaction together with element-geometry, here powder-impeller

blade and powder-cylindrical vessel, interaction.

A DEM solver is faced with two competing effects: accurate modeling of the bulk behavior of the discrete medium and computational efficiency. The choice of the interaction model, from now on referred to as the contact model, is a difficult one considering the absence of a constitutive law for DEM solvers [22]. There is no single holistic contact model capable of replicating the bulk behavior of the medium without applying some sort of calibration procedure [18, 22–27]. Therefore, a simple, first-order contact model is chosen for this study as followed by Mishra [75], Coetzee [76, 77] and many others [27]. Higher order contact models require more computational time with no guarantee of a seamless calibration match [18, 22–26]. This study assumes that the DEM entities, herein referred to as particles, are spherical in shape, cohesionless, undeformable (i.e., rigid) and have uniform size distribution.

6.2.2 Contact Model

The contact model used in this study is comprised of two damped Hookean-springs [22], one in normal (subscript n) and other in shear or tangential direction (subscript t), as shown in Fig. 6.1. The K and β stand for stiffness and damping respectively and the expressions for these are as given by equations 6.1, 6.2 [75]:

$$K_n = \frac{f^2 m_{eq} V_{max}^2}{\phi^2}; f = \frac{\phi}{\Delta_{max}} \tag{6.1}$$

$$\beta_n = -2\ln(\varepsilon)\left[\frac{K_n m_{eq}}{\pi^2 + \ln(\varepsilon)^2}\right]^{\frac{1}{2}} \tag{6.2}$$

Here m_{eq} stands for the equivalent mass of colliding particles, having diameter

ϕ and constant coefficient of restitution ε which is independent of impact velocity [18, 22]. This m_{eq} is one half of the harmonic mean of the individual masses. V_{max} and Δ_{max} are the estimated maximum speed and inter-particle penetration for the simulation at hand. These values are usually guessed (refer Section 6.3).

A slider is also present in the shear direction (refer Fig. 6.1). It limits the maximum frictional force in this direction, the value of which is equal to the product of sliding friction coefficient and normal reaction force $\underline{F_n}$ (given by Eq. 6.3). It is assumed that all the interactions cause particles to slide thereby nullifying the tangential damped Hookean spring. In other words, only the slider acts in the shear direction. Therefore, the forces along the normal ($\underline{F_n}$) and tangential ($\underline{F_t}$) directions experienced by a colliding particle with an overlap of Δ with other particles or geometries, relative approach speed of $\dot{\Delta}$ and unit vector $\underline{e_t}$ in shear direction as can be represented as:

$$\underline{F_n} = K_n \underline{\Delta_n} - \beta_n \underline{\dot{\Delta}_n} \tag{6.3}$$

$$\underline{F_t} = -\mu |\underline{F_n}| \underline{e_t} \tag{6.4}$$

Rolling and twisting motion of the particles has been ignored as done by Coetzee et al. [76, 77].

6.2.3 Neighborhood

In any DEM simulation, collision detection consumes a significant percentage of the entire computational time [73, 74]. One way to speed up a DEM simulation is to incorporate neighborhoods for particles. The neighborhood of a particular

particle refers to the group of particles surrounding it, which need to be checked for collisions. The neighborhood is updated every 100-200 iterations. In this study, for the CPU-based code which is used to model glass beads, neighborhoods based on the Delaunay Triangulation proposed by Ferrez [73, 74] have been employed. These neighborhoods require less memory and work with larger update intervals when compared to other neighborhoods like Verlet [73, 74].

6.2.4 GPU-based parallel computing using CUDA

The number of particles in Ti-6Al-4V rheometer simulations conducted in this study is around 435 thousand and 1.3 million. The high computational cost involved in these simulations necessitated the use of parallel programming. The massive parallelism in Graphical Processing Units (GPUs) can be utilized for parallel DEM computations. Therefore, the Ti-6Al-4V simulations were run by employing the Compute Unified Device Architecture (CUDA) [78] a GPU-based parallel computing platform and application programming interface (API) platform created by nVIDIA. Particle-particle collision detection is by far the most time-consuming step in the DEM process. Therefore, it was optimized using a spatial division technique [30] in concert with Verlet neighborhood. In this technique, the simulation space is subdivided in a uniform grid and the cells in the grid are indexed linearly. Every particle is then assigned to one grid cell based on its center. To detect all possible collisions for a particle, only the particles in neighboring (3 * 3 * 3 = 27) cells are needed to be checked. To find the particles in neighboring cells, a hash table is created for all the particles with a cell index as the hash value. Then the particles are sorted based on their hash values. This creates a list of particle IDs (identities) in cell order which can be used to find the particles in any cell using

binary search. The neighborhood for a single particle is created using particles within a user-defined spherical region and stored as a Verlet list which is updated every 50-100 iterations.

6.3 DEM calibration process

DEM models usually rely on a calibration process to get meaningful results due to the lack of a constitutive law [18, 22, 27]. This requires iteratively changing the micro-properties K, β and μ in such a way that the resulting virtual powder replicates the bulk behavior of the real powder. Wilkinson et al. [24] followed a machine learning based approach to identify the parameters for which the bulk behavior is most sensitive to, in other words the principal components of a multi-dimensional DEM assembly. This approach, though highly effective in finding the most sensitive parameters in a DEM contact model, requires one to carry out a lot of DEM runs to ensure that a wide range of DEM parameters has been covered. This approach becomes computationally expensive while dealing with hundreds of thousands of particles.

A flowchart for the calibration process used in the current study is shown in Fig. 6.2. Here stands for density, p for particle, v for vessel, i for impeller and the three subscripts pp, pv and pi stand for particle-particle, particle-vessel and particle-impeller interactions respectively. This process involves a two-step validation where the qualitative behavior of the virtual powder is validated by performing angle of repose tests (Virtual Experiments 1 and 2) and the quantitative behavior of the virtual powder is validated by performing a confined compressive flow energy test in a virtual rheometer. This approach is based on the one followed

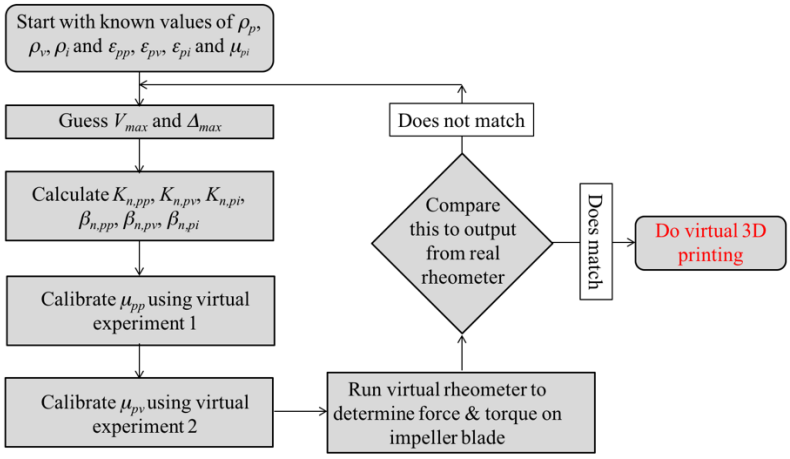

Figure 6.2: Flowchart showing DEM calibration process

by Ucgul [79] to study soil tillage and is similar to the one described by Coetzee [27] as a comprehensive approach towards bulk calibration involving some direct measurements. The calibration process tactfully isolates pp, pv and pi interactions for easy calibration of individual contact parameters.

Table 6.1: Material properties used in DEM rheometry simulations

Property	Impeller blade [18]	Rheometer vessel [18]	Glass beads [18]	Ti-6Al-4V
Density (kgm-3)	7800	2500	2600	4430
Young's Modulus (GPa)	189.8	62.4	62	114
Angle of repose	NA	NA	21.5° (VE 1) 21.5° (VE 2)	20.5° (VE 1) 18.5° (VE 2)

Note: VE = Virtual Experiment

6.3.1 Virtual Experiment 1: To calibrate μ_{pp}

This involves dropping of a cylindrical bed of approximately 8000 particles on a sheet of particles [80] from a height of four times particle diameter and tuning pp such that the angle of repose of the virtual pile matches the value in Table 6.1 within

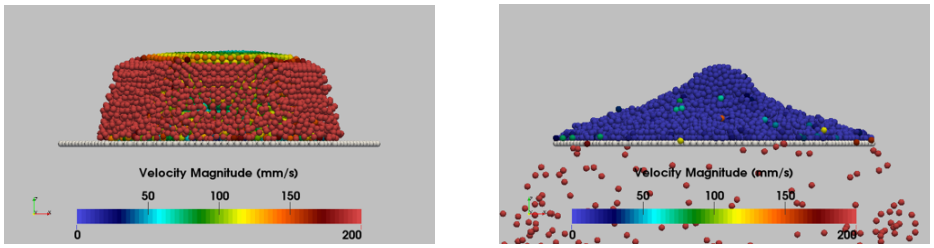

(a) time = 0.08s (b) time = 0.24s

Figure 6.3: Simulation snapshots for virtual experiment 1 with 2mm glass beads

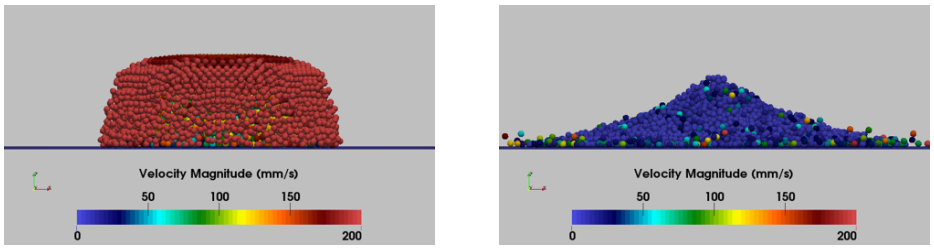

(a) time = 0.08s (b) time = 0.24s

Figure 6.4: Simulation snapshots for virtual experiment 2 with 2mm glass beads

the tolerance of 1° (refer Fig. 6.3). Before the drop, the particles are placed in a hexagonal close pack arrangement as opposed to face centered cubic arrangement which was used by Ucgul [79]. Also shown in Table 6.1 are other physical properties which are inputs to the contact model. Angle of internal friction for 250μm Ti-6Al-4V powder is measured using the rheometer's shear test apparatus [11] and is equal to the angle of repose for the assumed cohesionless Ti-6Al-4V powder [81].

6.3.2 Virtual Experiment 2: To calibrate μ_{pv}

This is similar to the first virtual experiment but now the particles are dropped on a flat plate made of the material of rheometer vessel, see Fig. 6.4, and pv is tuned to match the angle of repose of the virtual pile to the value in Table 6.1 within 1°.

6.3.3 Virtual rheometer: To examine the rheological behavior of virtual media

This involves confined-compressive loading of the particles in a virtual rheometer with 48mm impeller blade inside 50mm diameter vessel for 2mm glass beads and 23.5mm impeller blade inside 25mm diameter vessel for 250μm Ti-6Al-4V powder. The two blade geometries used in the simulations are modeled in close agreement with those seen in the real rheometers. The tip speed of impeller blade for the case of glass beads is 100mm/s [18, 22–26] and that for the case of Ti-6Al-4V powder is 100mm/s, 70mm/s and 40mm/s. The blade performs a penetrating action which comprises of a compressive downward rotational motion. Force and torque response, devoid of the presumed negligible impeller shaft effect, is calculated as done in studies [18, 22, 42]. The blade and vessel are assumed to be infinitely rigid.

Coefficient of friction between Ti-6Al-4V and impeller blade was found out experimentally by conducting a wall friction test using the rheometer [11]. In this test a 23.5 mm disc, having the material and surface roughness (of 0.25m) similar to the rheometer impeller blade, shears the powder at hand. This value was found out to be 0.12 (refer Table 6.2). Particle size does affect the behavior of a DEM model but the particle size distribution and coefficient of restitution have been shown to

Table 6.2: Contact interaction parameters used in DEM rheometry simulations

Property	Glass beads interacting with			Ti-6Al-4V powder interacting with		
	impeller [18]	vessel	glass beads	impeller	vessel	Ti-6Al-4V powder
ε	0.7	0.85 [18]	0.60 [18]	$0.8^{\#}$	$0.8^{\#}$	$0.8^{\#}$
μ	0.3	0.65*	0.30*	$0.12^{@}$	0.3*	0.185*

Note: * = value tuned via the DEM calibration process,
$^{@}$ = value measured using rheometer,
$_{\#}$ = assumed value

not affect the outcome of a DEM model applied to a powder rheometer [18, 25]. Therefore, in these simulations the particles sizes are kept as close to the real powder as possible and the size distribution is uniform. Coefficient of restitution is assumed to be 0.8 for all the collision pairs for case of Ti-6Al-4V powder (refer Table 6.2).

The force (F) and torque (T) response measured by the rheometer can be combined to calculate the energy required by the impeller blade to penetrate through the media. If h is the height traveled by the impeller blade, then the energy gradient is given as [23–26]:

$$\frac{dE}{dh} = \frac{T}{R\tan\alpha} + F \tag{6.5}$$

Here, R is the radius of the impeller blade of rheometer and is the angle of the helix formed by the motion of the blade. Validation for glass beads has been carried out on the F and T curves reported by Bharadwaj et al. [18]. Calibration for Ti-6Al-4V powder has been carried out for the cumulative flow energy, which is the integral of Eq. 6.5 over the height traveled by the impeller blade, as measured in-house by conducting 40 tests at impeller blades tip speed of 100mm/s. This calibrated virtual Ti-6Al-4V powder is then tested for virtual response at varying confined stress states enforced via varying impeller blades tip speeds. Blade tip speeds of 70mm/s and 40mm/s are chosen for testing the virtual Ti-6Al-4V powder and compared against 5 in-house experimental tests at each of these speeds.

In the problem of quantifying the ‘spreadability’ of AM powders, it is important to study the powder pileup in front of the spreader and the spread of powder under varying loads via varying spreader speeds. The calibration process to obtain the virtual powder bulk is designed such that it can robustly validate both of these

concerns. The virtual experiments 1 and 2 capture the former problem of powder pile-up in front of the spreader which is governed by the angle of repose while the virtual rheometry captures the latter problem of behavior of powder under known loading. The impeller blades tip speeds are chosen in the range of 40-100mm/s. These speeds are seen as spreader speeds in real 3D printing. Thus, the virtual bulk can comfortably serve as an input to the virtual spreading experiments and can be applied to study and optimize the powder spreading process in AM.

6.4 Results and Discussion

The tuned or calibrated values of pp and pv for 2mm glass beads and 250μm Ti-6Al-4V powder are shown in Table 6.2. These values are based on the guess values of Vmax as 20mm/s and Δ_{max} as 0.5% of particle diameter. Other values in Table 6.2 are from literature or measured experimentally by the authors or assumed close to real values.

6.4.1 Case 1: DEM modeling of 2mm glass beads

Simulation snapshots of 48 mm virtual rheometer simulation for 2mm glass beads with a fill height H of 25mm are shown in Fig. 6.5 for blade tip speed of 100mm/s. The rotational speed of blade is 4.15 rad/s and its downward translational speed is 8.72mm/s. The angle of the helix formed by the motion of the blade is -5° [18]. The particles are colored by the magnitude of their velocity. Simulation using Verlet neighborhood generation algorithm required a storage of 45 neighbors per particle and an update interval of 50 iterations. As opposed to this, a simulation using Delaunay Triangulation for neighborhood generation was much faster as it

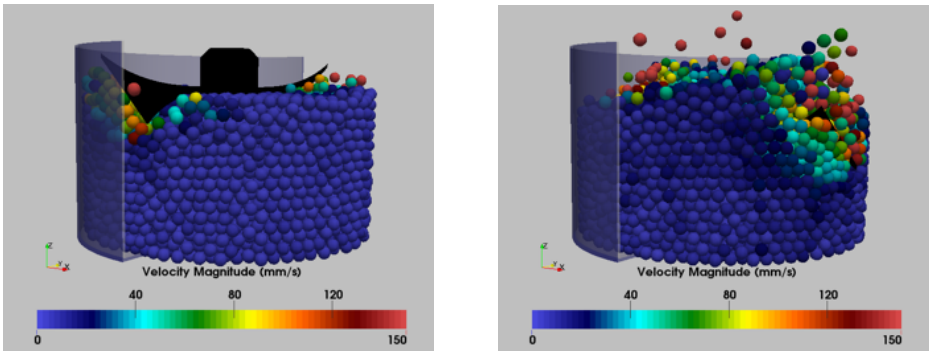

(a) time = 0.6s (b) time = 1.0s

Figure 6.5: **Case 1**- Simulation snapshots for confined-compressive loading inside 48mm virtual rheometer with 2mm glass beads. The particles are colored by the magnitude of their velocity.

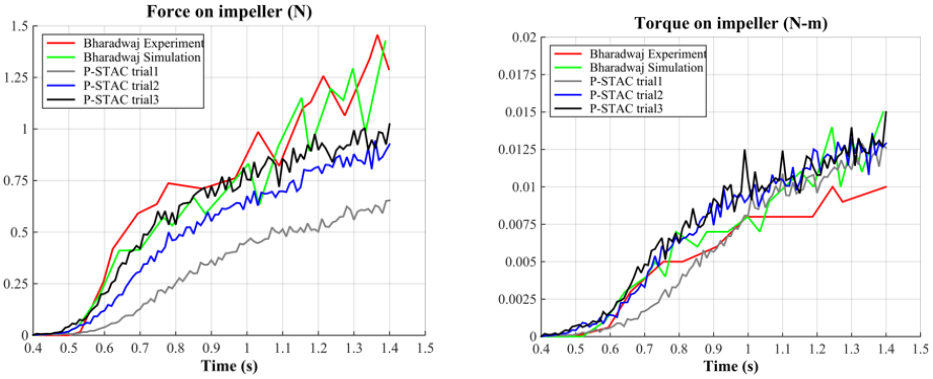

(a) (b)

Figure 6.6: **Case 1**- Force (a) and torque (b) response for 48mm virtual rheometer with 2mm glass beads

required a storage of 20 neighbors per particle, and update interval of 200 iterations. These results look similar to those obtained by Bharadwaj [6] using a higher order contact model. Few particles can be seen escaping the powder bulk, this though unreal for an actual experiment, does not affect the bulk material behavior as seen in Fig. 7 (P-STAC trial3) and can be attributed to a larger neighborhood update

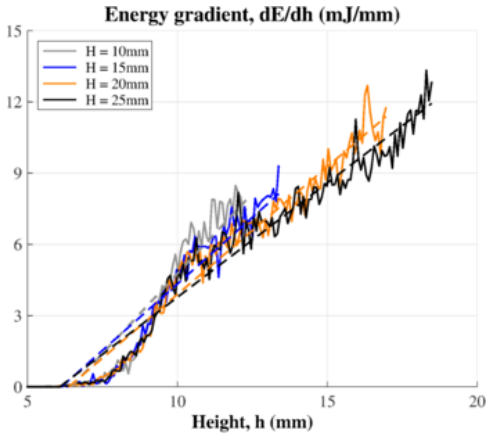

Figure 6.7: Fill height independence study for 48mm virtual rheometer with glass beads (η=10mm)

Table 6.3: Fill height independence study for 48mm virtual rheometer with glass beads (η=10mm)

Fill height (H)	Fitted line		% N-RMS error
	Slope	Intercept	
1.0η	1.3504	-8.7324	19.85
1.5η	1.1213	-6.8795	9.05
2.0η	1.0758	-6.8622	4.83
2.5η	0.9625	-5.8498	-

interval. The force and torque response predicted by CPU-based P-STAC trial3 in Fig. 6.6, DEM simulation parameters for which are shown in Table 6.2, matches well with that obtained by Bharadwaj [4]. Slight discrepancy can be attributed to the assumptions of negligible rolling resistance and slide-always frictional behavior for particle motion. The three trials corresponding to P-STAC curves in Fig. 7 make use of different Vmax values. The calibration algorithm iteratively changes Vmax such that the area under curves of force and torque experienced by the impeller blade is within acceptable tolerance when compared to the experimental results.

It is necessary to find out the minimum fill height H, to be tested in a virtual

rheometer, which can be matched to the experimental data with maximum confidence. This helps in reducing the computational time when the number of particles increases to hundreds of thousands, as in the case Ti-6Al-4V powder. With this in mind, virtual rheometer with glass beads was run for varying fill heights, refer Fig. 8. The energy gradient dE/dh given by Eq. 6.5 has been plotted for various runs. Also, shown in dashed-line in corresponding color is the straight line fitted to a dE/dh curve. Assuming the energy gradient response against the height traveled by impeller blade to be linear and response of virtual rheometer to the fill height of 25mm to be the true solution, normalized root mean square (N-RMS) errors are shown in Table 6.3. Also shown are the slope and intercept for each of the fitted lines. Clearly a fill height of twice the blade height is sufficient to predict the response with good accuracy. This study is referred here as *fill height independence study*.

These simulations in case 1 have been carried out using CPU-based P-STAC on a workstation with 32 GB memory running on a 3.7 GHz processor, using serial programming. The simulation time was around 30-45 minutes.

6.4.2 Case 2: DEM modeling of 250μm Ti-6Al-4V powder

A: Generating virtual avatar of real powder via confined, compressive loading at impeller blade tip speed of 100mm/s at small fill height

Around 14mm powder fill height was simulated in this case. This fill height is more than twice the blade height (Note: the impeller blade for this case is 23.5mm in diameter and about 5mm in height). Figure 6.8 shows simulation snapshots for the 23.5mm diameter virtual rheometer with 250μm Ti-6Al-4V powder for blade tip

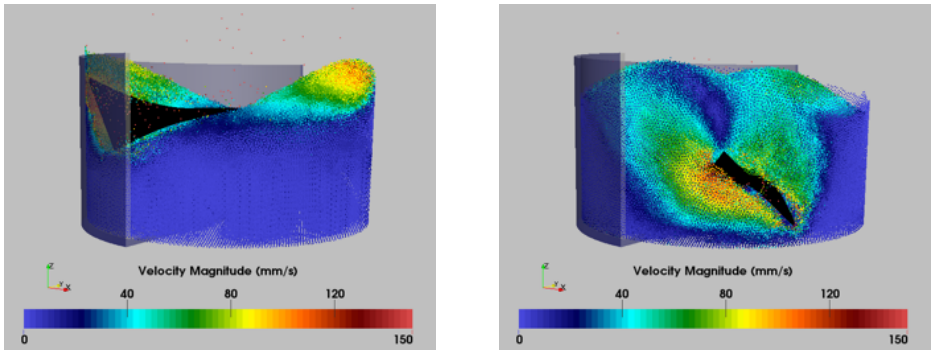

(a) time = 1.1s (b) time = 1.7s

Figure 6.8: **Case 2A**- Simulation snapshots for confined compressive loading inside 23.5mm virtual rheometer with 250μm Ti-6Al-4V powder. The particles are colored by their velocity magnitude.

speed of 100mm/s. This simulation has around 435,000 particles. The rotational speed of blade is 8.48 rad/s and its downward translational speed is 8.72mm/s. The angle of the helix formed by the motion of the blade is -5°. The particles are colored by the magnitude of their velocity. Powder heap formation in front of the impeller blade is in qualitative agreement with experimental findings (images for experimental findings are not shown). Similar to case 1, few particles can be seen escaping the powder bulk, this though unreal for an actual experiment, does not affect the bulk material behavior as seen in Fig. 6.9a (P-STAC trial3, DEM simulation parameters are shown in Table 6.2). Again, the calibration algorithm iteratively changes Vmax such that the area under cumulative energy curves is within acceptable tolerance when compared to the experimental values. The three corresponding trials are also shown in Fig. 6.9a. The energy response predicted by P-STAC trial3 matches well with the in-house experimental data. This calibrated DEM model of 250μm Ti-6Al-4V powder is referred to as the "virtual avatar" of the real 100-250μm Ti-6Al-4V powder. Slight discrepancy can be attributed to

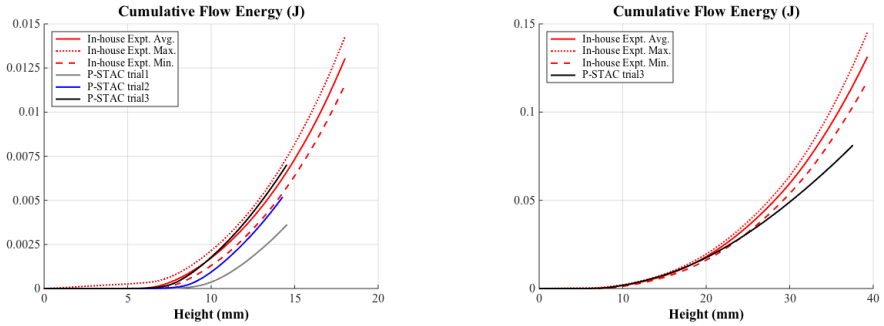

(a) **Case 2A**- Small fill height (b) **Case 2B**- Large fill height

Figure 6.9: Energy response for 23.5mm virtual rheometer with 250μm Ti-6Al-4V powder

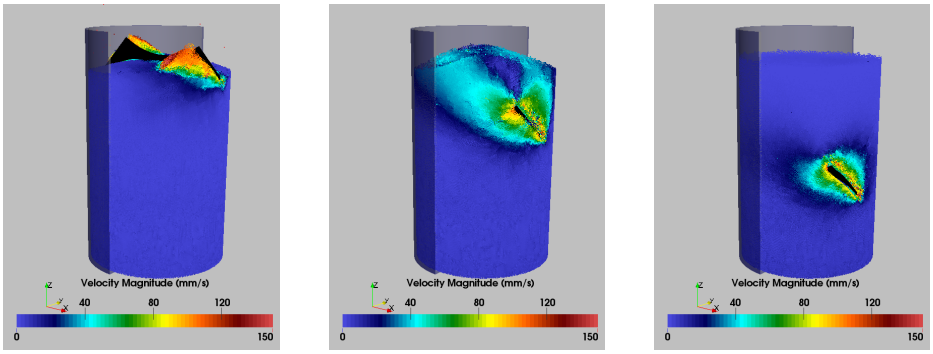

(a) time = 1.12s (b) time = 2.24s (c) time = 3.36s

Figure 6.10: **Case 2B**- Simulation snapshots for confined compressive loading inside 23.5mm virtual rheometer with 250μm Ti-6Al-4V powder. The particles are colored by their velocity magnitude.

the modeling of 250μm particles to represent a real powder in the range of 100-250μm and neglect of cohesive forces which can be present in the real powder. This simulation has been carried out using GPU-based P-STAC on an nVIDIA GeForce GTX 970 graphics card. The simulation time was around 2 hours.

B: Testing the virtual avatar of the real powder for confined, compressive loading at impeller blade tip speed of 100mm/s at larger fill height

In this case, the virtual powder obtained in case 2A and corresponding to DEM simulation parameters shown in Table 6.2, is used to simulate a larger fill height of 38mm. Figure 6.10 shows simulation snapshots for the 23.5mm diameter virtual rheometer with 250μm Ti-6Al-4V powder for blade tip speed of 100mm/s. This simulation has around 1.3 million particles. The rotational speed of blade is 8.48 rad/s and its downward translational speed is 8.72mm/s. The angle of the helix formed by the motion of the blade is -5°. The particles are colored by the magnitude of their velocity. The energy response predicted by P-STAC is shown in Fig. 6.9b and matches fairly well with experimental results. This simulation has been carried out using GPU-based P-STAC on an nVIDIA GeForce GTX 970 graphics card. The simulation time was around 43 hours and 45 minutes. This drastic increase in simulation time as compared to that in case 2A is due to the increase in the number of of particles and increase in the total height traversed by the blade.

C: Testing the virtual avatar of the real powder for confined, compressive loading at impeller blade tip speed of 70mm/s at large fill height

In this case, the virtual Ti-6Al-4V powder obtained in case 2A and corresponding to DEM simulation parameters shown in Table 6.2, is tested for its behavior in the virtual rheometer for a fill height of 38mm and blade tip speed of 70mm/s. Figure 6.11a shows energy response predicted by P-STAC. This simulation has around 1.3 million particles. The rotational speed of blade is 6.1rad/s and its downward translational speed is 5.9mm/s. The angle of the helix formed by the motion of the

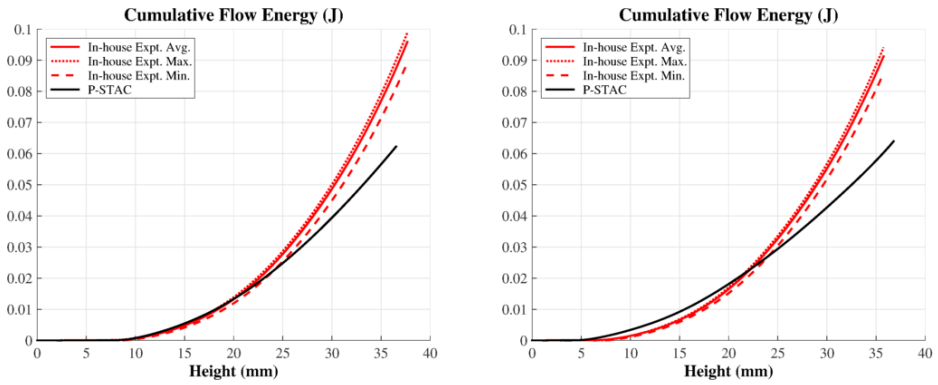

(a) **Case 2C**- Blade tip speed = 70mm/s (b) **Case 2D**- Blade tip speed = 40mm/s

Figure 6.11: Energy response for 23.5mm virtual rheometer with 250μm Ti-6Al-4V powder with large fill height.

blade is -5°. The particles are colored by the magnitude of their velocity. The flow energy response predicted by P-STAC matches fairly well with the experimental results. The discrepancies can be assigned to same factors listed in case 2A. This simulation has been carried out using GPU-based P-STAC on an nVIDIA GeForce GTX 970 graphics card. The simulation time was around 62 hours and 30 minutes. This time is higher than that in case 2B as the blade motion needs to be simulated for a longer time owing to the decrease in the downward translation speed.

D: Testing the virtual avatar of the real powder for confined, compressive loading at impeller blade tip speed of 40mm/s at large fill height

In this case, the virtual Ti-6Al-4V powder obtained in case 2A and corresponding to DEM simulation parameters shown in Table 6.2, is tested for its behavior in the virtual rheometer for a fill height of 38mm and blade tip speed of 40mm/s. Figure 6.11b shows energy response predicted by P-STAC. This simulation has around 1.3 million particles. The rotational speed of blade is 3.5rad/s and its downward

translational speed is 3.4mm/s. The angle of the helix formed by the motion of the blade is -5°. The particles are colored by the magnitude of their velocity. This simulation has been carried out using GPU-based P-STAC on an nVIDIA GeForce GTX 970 graphics card. The simulation time was around 109 hours and 20 minutes. This time is higher than that in case 2C as the blade motion needs to be simulated for a longer time owing to the decrease in the downward translation speed. The response predicted by P-STAC has a larger deviation from experimental results than in cases 2B and 2C. Still the virtual powder, making use of a simple damped Hookean spring and slider contact model, which has been calibrated only for case 2A is able to capture the energy response for impeller blade speeds in the range of 40-100mm/s within acceptable tolerances.

This virtual avatar of real Ti-6Al-4V can now serve as an input to a virtual spreading simulation with spreader speeds in the range of 40-100mm/s to obtain an application specific spreading recipe, in terms of spreader speed and geometry, to give the desired powder layer for each spread.

6.5 Conclusions

An experimentally-validated AM powder simulation framework has been presented in this study. It is shown that it is possible to use a damped Hookean spring and slider arrangement-based DEM model along with a robust DEM calibration process to simulate the powder dynamics encountered in a rheometer with reasonable accuracy. To achieve computational efficiency for CPU-based simulations, collision detection has been performed using Delaunay Triangulation, which is found to be much more efficient that the traditional Verlet technique. But the CPU-based, serial simulations

become increasingly time expensive for simulating 250μm Ti-6Al-4V, and thus GPU-based simulations were carried out for higher particle numbers. The DEM model has been successfully applied to study the rheology of macro-particles like 2mm glass beads and micro-particles like 100-250μm Ti-6Al-4V AM powder. The fill height independence study in concert with a robust calibration algorithm establishes a computationally efficient way to generate a virtual powder which behaves similar to the real powder and need not be calibrated for different loadings. The model compares well with experimental findings and prior result from another higher order DEM model. The restrictions of uniform particle size distributions and non-existent of cohesive forces can be relaxed in future efforts to increase prediction accuracy. A higher-order, non-linear contact model can be applied to powders like 250μm Ti-6Al-4V but that will come at excessive computational costs. The computational model developed herein can now be applied to study and optimize the powder spreading process in AM.

Innovation distinguishes between a leader and a follower.
-Steve Jobs

Chapter 7

Developing Spreading Process Maps via Physics-based Modeling and Machine Learning

A similar version of few sections of this chapter have appeared in SFF Conference Proceedings [82]: Zhang, W., Mehta A., Desai, P. S., and Higgs III, C. F., *Machine Learning enabled Powder Spreading Process Map for Metal Additive Manufacturing (AM)*

Abstract

The technology of powder-bed Additive Manufacturing (AM), more commonly known as “three-dimensional (3D) printing”, has been evolving rapidly over the last few years. The powder-bed AM process involves two main steps: spreading of powder in thin layer and then fusing or binding the spread layer. Creating parts through additive manufacturing within acceptable tolerances for surface roughness and porosity is contingent upon many process variables. Most of the AM research is focused on the second step of powder fusion. The first step of powder spreading is more rarely studied but is of significant importance with respect to the quality of the final part and total print or build time. The spreading step controls powder layer defects of roughness and porosity and can consume anywhere from 10% to 50% of the overall build time with the machine default spreader speeds. It is thus essential to understand how to modify the spread parameters like spreader speed to generate a layer having desired roughness and porosity in the most time efficient manner. Considering the difficulties involved in studying this problem experimentally, a physics-based computational modeling approach, making use of discrete element method (DEM), is applied to simulate the spreading process. DEM simulations in this study involve spreading of virtual Ti-6Al-4V powder, which is commonly used in 3D printing, on substrates having 3 different roughness values. A Particle Tessellated Surface Interaction Scheme to accurately capture the collisions between virtual AM powder and the spreader geometry and the previously 3D printed bottom surface in DEM is introduced. Since the DEM simulations are computationally expensive, only a few such simulations are run following a design of simulations approach. Subsequently, machine learning was employed to interpolate between the

highly non-linear results obtained by the DEM simulations. Based on the spreading process predictions, the most efficient spreading parameters can be found to achieve an acceptable surface finish. This eventually saves the total time for printing and reduces the cost of build.

Nomenclature

Symbol	Meaning
L_1, L_2, L_3	Barycentric coordinates of a point (x,y) with respect to a triangle having vertices (x1,y1), (x2,y2) and (x3,y3)
$\underline{P}$	Position vector of the projection point of center of a spherical particle on the plane of a triangle of a tessellated solid geometry
$\underline{v_1}, \underline{v_2}, \underline{v_3}$	Position vectors of vertices of a triangle of a tessellated solid geometry
$\underline{e_1}, \underline{e_2}, \underline{e_3}$	Edges of a triangle of a tessellated solid geometry
$\underline{n_T}$	Normal vector to the plane of a triangle of a tessellated solid geometry
$\underline{C}$	Position vector of center of a spherical particle
$\underline{U}$	Position vector of the point of contact of a spherical particle with the plane of a triangle of a tessellated solid geometry
Δ	Overlap of a particle with another particle or geometry
ϕ	Diameter of a spherical particle
K	Stiffness of spring in a spring-dashpot system
β	Damping of dashpot in a spring-dashpot system
n,t	Subscripts: normal and tangential directions respectively
ε	Coefficient of restitution
m	Particle mass
V	Particle speed
μ	Coefficient of sliding friction
$\underline{e_t}$	Unit vector along the tangential direction
U	Translation speed of the spreader
ω	Rotational speed of the spreader
Q_s	Volume of powder spread per unit time per unit width of spreader
R_q	Roughness of spread layer
S_q	Roughness of substrate
L	Loss function
N	Total number of training samples
Y,O	Actual and target output vectors respectively
α	Learning rate
λ	Regularization parameter
R	Correlation coefficient

7.1 Introduction

Powder-bed additive manufacturing (AM), colloquially known as three-dimensional (3D) printing, is one of the few types of technologies slated to disrupt the traditional manufacturing industry predominantly dependent on casting, molding and subtractive manufacturing. The state-of-the-art powder-bed 3D printers are optimized to work only with a handful of powders and the parts built using such printers have rough exterior and porous interior. The 3D printing process used involves repetitive spreading of powder and fusing or binding of the spread layer until the entire geometry is 3D printed [9], (see Chapter 6) refer Fig. 7.1. A commonly used metal powder made of Ti-6Al-4V and a cylinder printed using this powder are shown in Figs. 7.2a and 7.2b respectively. Optical scan of the top surface of printed cylinder can be seen to have noticeable striations, refer Fig. 7.2c, which make the part non-isotropic with unpredictable mechanical properties and rough exterior. Most of the existing AM research is clustered around fusing (e.g., laser sintering or melting) process optimization [71, 72]. The step of powder spreading is rarely studied and makes use of machine default spread settings; however uniform spreading of powder layer is mandatory to 3D print dense and isotropic parts with a smooth surface finish. Only a handful of studies [83–86] have attempted to answer the influence of spreading step in the entire 3D printing process.

Herbold et al. in 2015 [83] performed a computational study which used 40-particles square by 10-particles deep domain with particle sizes as seen in real AM metal powders but no justification was provided as to the choice of the domain size and no experimental validation was provided for the spreading simulations. Parteli and Pschel in 2016 [85] incorporated complex shapes of powder particles

and provided relationships between spreader speeds and layer roughness. Using only model simulation results, in this work they employed a small domain size with periodic boundary conditions. Haeri et al. in 2016 [84] and Mindt et al. in 2016 [86] followed a small domain simulation approach as done by Parteli and Pschel in 2016 [85]. Haeri et al. in 2016 [84] made use of rod-like particles and two spreader geometries, a blade and a roller, comprised of spherical particles, thereby adding an unreal roughness to the spreaders. The study conducted by Mindt et al. in 2016 [86] has accounted for true geometry of the previously printed layer along with particle size distribution. They have also simulated the fusion process. Similar to the aforementioned works, the domain simulated in their work was smaller than the real size of a build platform.

The authors of this paper aim to study the *spreadability* of AM powders, i.e., the ability to spread under a given compressive load, by following a synergistic approach involving interplay of experiments, physics-based modeling and machine learning as summarized in Section 7.2. Section 7.3 describes the in silico virtual spreading experiments performed in scenarios similar to those found in real 3D printers using physics-based GPU-optimized Discrete Element Method (DEM). DEM used to simulate the powder spreading process requires an accurate representation of the previously printed bottom surface and the spreader geometry. In order to simulate these interactions, a model to detect collisions between triangulated surfaces and spherical particles has been developed. Since the DEM simulations are computationally expensive, only a few such simulations are run following a design of simulations approach. Subsequently, in Section 7.4, machine learning has been employed to interpolate between the highly non-linear results obtained by the DEM simulations. Spreading process maps generated using such a synergistic approach

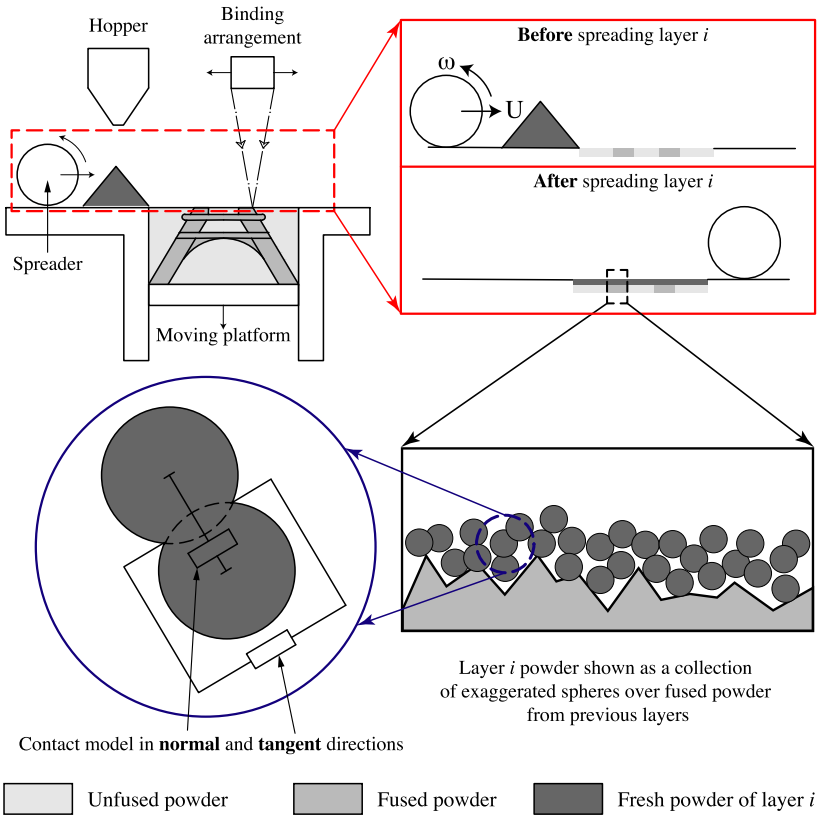

Figure 7.1: Schematic of powder-bed AM process (top left) with insets showing powder spreading (top right and bottom right) and contact model used in physics-based modeling (bottom left)

can be used to find the most efficient spreading parameters to achieve a desirable surface finish.

7.2 Methodology

The problem to study the spreadability of AM powders is twofold, firstly, it is difficult to study this problem experimentally inside a real 3D printer which often works in an inert atmosphere, due to the difficulty involved in characterizing the

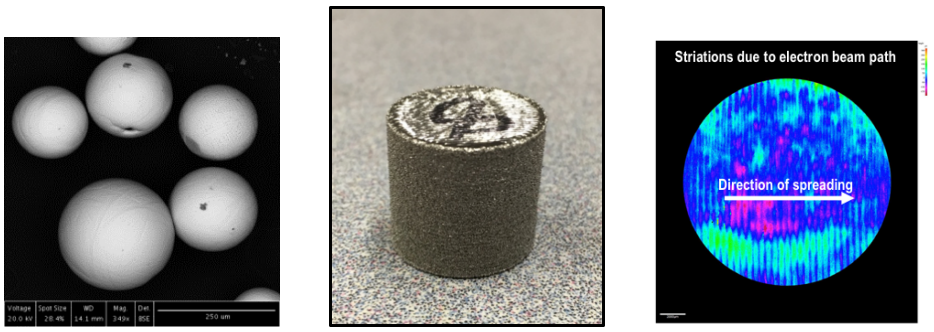

(a) (b) (c)

Figure 7.2: **(a)** SEM image of 250μm Ti-6Al-4V powder [2], **(b)** 3D printed cylinder from an AM machine using electron beams for binding the metal powder shown in (a), **(c)** Optical image of the top surface of (b)

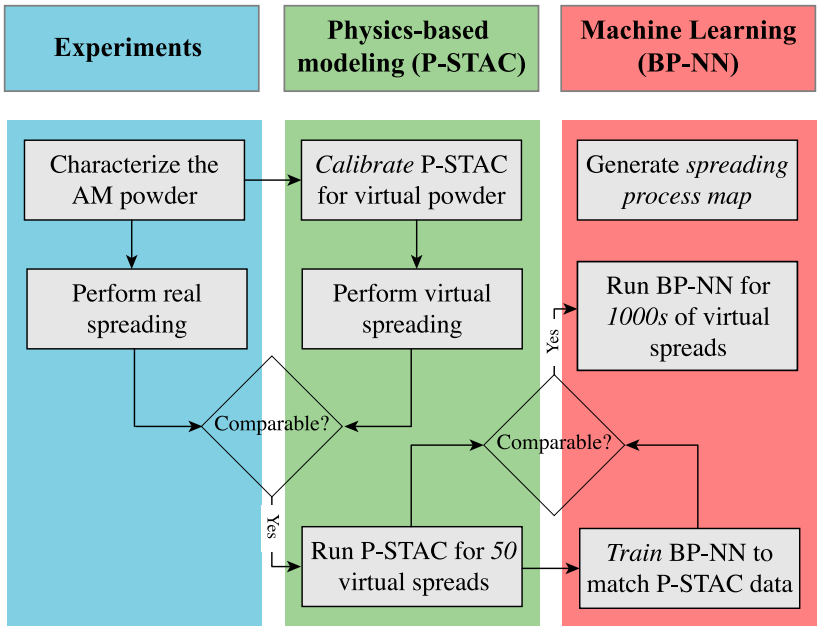

Figure 7.3: Synergy between experiments, physics-based DEM simulations and machine learning

spread layer properties without interfering with the inert conditions. The safety issues associated with the handling of AM powders like toxicity, flammability and

explosivity make a trial-and-error approach, common with experimental studies, unrealistic and unsafe [20]. This first problem makes the experimental study not only difficult but also expensive. Secondly, computational study of this problem is also not trivial as the DEM, most well suited among other computational techniques, is based on Lagrangian principles and has no simple constitutive laws for AM powders [18], refer Chapter 6 . Therefore, a synergistic, three-step approach as shown in Fig. 7.3 is used to predict spreadability of AM powders. The first step involves the characterization of the AM powder using a state-of-the-art powder rheometer and using the data for calibrating a virtual powder which behaves similar to the real AM powder as discussed in (refer Chapter 6). This rheometer also serves the purpose of validating the DEM model and exposes the powder to loadings similar to those seen in powder spreading. The second step involves the spreading simulation study of this rheometry-validated virtual powder and comparison to the real spreading, if possible but has not been done in this study. Finally, refer Fig. 7.3, the simulation data is used to train and test regression algorithms based on machine learning, like back propagation neural networks, to generate spreading process maps. These maps show the relations between 3D printer operator's input parameters like spreader speeds and spread layer properties. The following sections describe the second and third steps of this methodology and discuss the results obtained using these steps.

7.3 Physics-based DEM Modeling

Discrete Element Method (DEM) is used in this study to simulate the powder spreading process in AM. This problem requires an accurate representation of the

spreader geometry and the previously 3D printed bottom surface. DEM used in this study makes use of uniformly sized, 235,000 smooth spherical, cohesionless elements of 250μm diameter to represent the AM powder. Fig. 7.2a shows an SEM image of a Ti-6Al-4V powder, commonly used in AM, which has the maximum size of about 250μm. Also shown are a 3D-printed cylinder and its top-surface optical scan in Fig. 7.2b and Fig. 7.2c respectively. The striations seen in Fig. 7.2c are in the direction of spreading and can be attributed to uneven heating of the spread layer by the electron beams [87]. The roughness R_q of the top surface of this 3D printed cylinder was about 46.5μm. In order to simulate the interactions of AM powder with the spreader geometry and the previously 3D printed bottom surface, a model to detect collisions between triangulated surfaces and spherical particles is developed. The length scales involved in these simulations, which have particles with sizes of 10 to a few hundred micrometers and the spread layer of 10s of centimeters in size, drastically increase the number of computations as the particle count can easily reach millions. In order to simulate this problem in realistic times without compromising with the accuracy of the simulation, the DEM code is parallelized to run on a Graphics Processing Unit (GPU) using (refer Chapter 6). There are two different types of collisions involved in the simulation of powder spreading in AM, namely powder particles colliding with other powder particles and powder particles colliding with the solid surfaces of spreader and previously 3D printed bottom surface. Each type of collision has its own computational challenges. The former particle-particle collision requires an efficient neighborhood search [73] while the latter, particle-surface collision, requires an accurate representation of the surface geometry. The neighborhood search is the most time-consuming step in a DEM simulation. Hence, a verlet-based [4, 73, 78] efficient neighborhood search

algorithm is employed using a technique called “spatial binning” [30] to further improve the performance of the solver. The solution to incorporate accurate surface geometry is described in the following sub-section.

7.3.1 Particle Tessellated Surface Interaction Scheme

In DEM modeling of AM spreading process, particle and solid surface contact detection model is of significant importance to efficiently and accurately capture the interaction between the AM powder and solid surfaces. These solid geometries can be represented by several methods. One way to represent solid geometries is to cover the solid surfaces (spreader and previously 3D-printed bottom surface) with spheres and moving these based on the prescribed motion of the solid surfaces [4]. This simplifies the calculation of particle - solid surface contact as these contacts are now just particle-particle contact. But this treatment of solid surfaces is not able to capture the solid geometry accurately. A solid surface having sharp edges or fine topographical changes can not be represented realistically with such a treatment of solid geometry. In the AM spreading process, the distance between bottom surface and the spreader is very small, therefore the inaccuracies of this method have a significant effect on the final quality of the layer.

On the other hand, a tessellated representation of a solid surface, in the form of triangular mesh, is able to accurately capture any surface geometry. If the AM powder is represented as collection of spherical particles and AM substrate and spreader geometry are represented as tessellated surfaces with triangular elements, the algorithm to perform Particle Tessellated Surface Interactions can be given as:

For every spherical particle *i*,

1. Generate a neighborhood of nearest triangular faces of the tessellated surfaces of spreader and previously 3D-printed bottom surface as a collection of triangles lying within a particle diameter from the center of the particle *i*

2. For each triangular face in the neighborhood generated in Step 1

   (a) Sequentially check for intersection of particle *i* with inner area, edges and vertices of the triangular face

   (b) Omit the invalid or duplicate particle triangular face contacts

   (c) Apply contact forces to the particle *i* (due to its interaction with the triangular face) for valid contacts

Step 1 can be performed using Verlet algorithm [4]. Step 2-a can be performed by using Barycentric co-ordinates of a point (x,y) with respect to a triangle given by points 1,2 and 3, as shown in Fig. 7.4a taken from [32]. These Barycentric co-ordinates, denoted by L1, L2 and L3 can be obtained by solving the following set of equations:

$$\begin{aligned} x &= x_1L_1 + x_2L_2 + x_3L_3 \\ y &= y_1L_1 + y_2L_2 + y_3L_3 \\ 1 &= L_1 + L_2 + L_3 \end{aligned} \tag{7.1}$$

The signs of these Barycentric co-ordinates can now be used to determine the location of point (x,y) with respect to the triangle as shown in 7.4b. For example, if $L_1, L_2 > 0$ and $L_3 < 0$ then the point (x,y) lies in the voronoi region of edge1-2 and so on. In the case of determining the type of contact, if point (x,y) is the projetion

(a) (b)

Figure 7.4: Location of point (x,y) with respect to a triangle given by points 1, 2 and 3 [32]

of the center of particle sphere on the plane of triangular face, then the particle might undergo an edge collision. As calculating a matrix inverse is computationally expensive and the type of contact is only determined on the basis of the sign of the Barycentric co-ordinates and the magnitude is not of direct use, authors of this paper have used the following method, inspired by [31] to determine the location of the projection of particle center, denoted by $\underline{P}$, on the plane forming the triangular face with respect to the triangle formed by vertices $\underline{v_1}$, $\underline{v_2}$ and $\underline{v_3}$ as shown in Fig. 7.5. The edges are given by Eq. 7.2.

$$\begin{aligned} \underline{e_1} &= \underline{v_3} - \underline{v_2} \\ \underline{e_2} &= \underline{v_1} - \underline{v_3} \\ \underline{e_3} &= \underline{v_2} - \underline{v_1} \end{aligned} \tag{7.2}$$

If $\underline{n_T}$ is a vector normal to the plane of the triangle and $\widehat{\underline{n_T}}$ is a unit normal

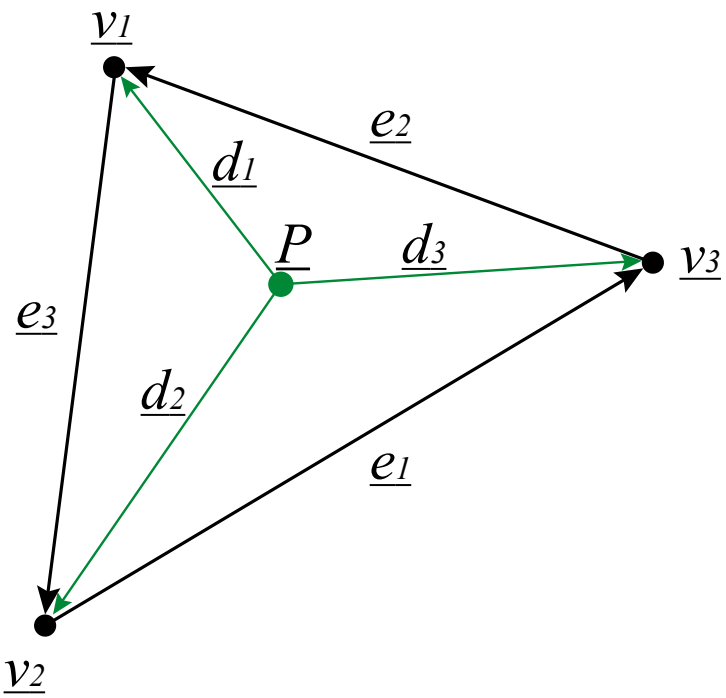

Figure 7.5: Case showing surface triangle formed by vectors v_1, v_2 and v_3 with point vector P lying in the interior of the surface triangle

vector normal to the plane of the triangle, then

$$\begin{aligned} \underline{n_T} &= \underline{e_1} \times \underline{e_2} \\ \widehat{\underline{n_T}} &= \frac{\underline{n_T}}{||\underline{n_T}||} \end{aligned} \tag{7.3}$$

If the center of the sphere is denoted by $\underline{C}$ then the projection of the center of the sphere, denoted by $\underline{P}$, on the plane of the triangle can be expressed as:

$$\underline{P} = \underline{C} + \left((\underline{v_1} - \underline{C}) \cdot \widehat{\underline{n_T}}\right)\widehat{\underline{n_T}} \tag{7.4}$$

Depending on the location of the projection point $\underline{P}$, the sphere can collide with

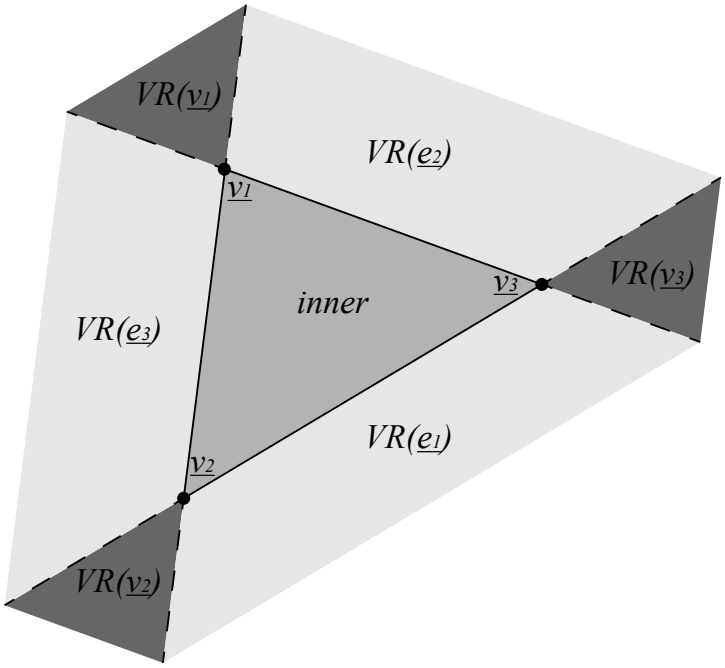

Figure 7.6: Voronoi regions (VR) of surface triangle formed by vectors v_1, v_2 and v_3.

either the face, one of the edges or one of the vertices. The voronoi regions which can decide the region in which $\underline{P}$ can lie are given in Table 8.2 and shown in Fig. 7.6. Also, given in Table 8.2 is the definition of point $\underline{Q}$ which is the point of contact between the sphere with diameter ϕ and the triangular face.

Where,

$$\underline{d_i} = \underline{v_i} - \underline{P} \tag{7.5}$$

$$\begin{aligned} \underline{n_1} &= \underline{d_2} \times \underline{d_3} \\ \underline{n_2} &= \underline{d_3} \times \underline{d_1} \\ \underline{n_3} &= \underline{d_1} \times \underline{d_2} \end{aligned} \tag{7.6}$$

$$\underline{h_i} = \underline{n_T} \cdot \underline{n_i} \tag{7.7}$$

$$\begin{aligned} g_1 &= \left(\underline{P} - \underline{v_2}\right) \cdot \underline{e_1} \\ g_1' &= \left(\underline{P} - \underline{v_3}\right) \cdot \underline{e_1} \\ g_2 &= \left(\underline{P} - \underline{v_3}\right) \cdot \underline{e_2} \\ g_2' &= \left(\underline{P} - \underline{v_1}\right) \cdot \underline{e_2} \\ g_3 &= \left(\underline{P} - \underline{v_1}\right) \cdot \underline{e_3} \\ g_3' &= \left(\underline{P} - \underline{v_2}\right) \cdot \underline{e_3} \end{aligned} \tag{7.8}$$

Since, the point $\underline{Q}$ is the contact point, the overlap of the sphere with the

Table 7.1: Voronoi regions (VR) for all possible contacts and the respective definition of point of contact Q vector

Contact Type	Region	Condition	Contact Point
Face	Inner	$h_i \geq 0, \forall\, i \in \{1,2,3\}$	$\underline{Q} = \underline{P}$
Edge	VR($\underline{e_1}$)	$h_1 < 0 \cap g_1 > 0 \cap g'_1 < 0$	$\underline{Q} = \underline{v_2} + \frac{g_1}{\|\underline{e_1}\|^2}\underline{e_1}$
	VR($\underline{e_2}$)	$h_2 < 0 \cap g_2 > 0 \cap g'_2 < 0$	$\underline{Q} = \underline{v_3} + \frac{g_2}{\|\underline{e_2}\|^2}\underline{e_2}$
	VR($\underline{e_3}$)	$h_3 < 0 \cap g_3 > 0 \cap g'_3 < 0$	$\underline{Q} = \underline{v_1} + \frac{g_3}{\|\underline{e_3}\|^2}\underline{e_3}$
Vertex	VR($\underline{v_1}$)	$g_3 < 0 \cap g'_2 > 0$	$\underline{Q} = \underline{v_1}$
	VR($\underline{v_2}$)	$g_1 < 0 \cap g'_3 > 0$	$\underline{Q} = \underline{v_2}$
	VR($\underline{v_3}$)	$g_2 < 0 \cap g'_1 > 0$	$\underline{Q} = \underline{v_3}$

triangular element, denoted by Δ,can be calculated as given in Eq. (7.9)

$$\Delta = \frac{\phi}{2} - ||\underline{Q} - \underline{C}|| \tag{7.9}$$

All triangles are checked for possible contacts with every particle. This may result in multiple contacts or invalid contacts which need to be eliminated in Step 2-b. Methodology to eliminate these multiple and invalid contacts is discussed in details by Hu et al. in 2013 article [31]. The Δ thus obtained can now be used in the DEM contact model to calculate the force experienced by the particle, Step 2-c.

7.3.2 Contact Model

Please refer Section 6.2.2 in Chapter 6 to understand the contact model used in the current study.

7.3.3 Design of Simulations (DoS) for virtual spreading

Spreading simulations require a set of contact force parameters which can make the virtual powder bulk comprising of uniformly sized, 235,000 smooth spherical, cohesionless elements of 250μm diameter behave in ways similar to a real AM powder. The density of these spherical particles is 4430kg/m^3 and is equal to the real AM Ti-6Al-4V powder shown in Fig. 7.2a. This virtual bulk is developed by

Table 7.2: Contact interaction parameters used in DEM spreading simulations

Property	Ti-6Al-4V powder interacting with		
	spreader	3D printed substrate	Ti-6Al-4V powder
ε	$0.8^{\#}$	$0.8^{\#}$	$0.8^{\#}$
μ	$0.12^{@}$	$0.25^{\#}$	0.185*

Note: * = value tuned via the DEM calibration process,
$^{@}$ = value measured using rheometer,
$_{\#}$ = assumed value

Table 7.3: Design of Simulations (DoS) for virtual spreading

Parameter	Range of values
Spreader diameter (mm)	10
Spreader length (mm)	70
Spreader translation speed, U (mm/s)	40, 55, 70, 85, 100
Spreader rotation speed, ω (rad/s)	0, 5, 10, 15, 20, -5, -10, -15, -20
Substrate roughness S_q (μm)	0, 46, 99

using the calibration process mentioned in The DEM parameters used in this study are summarized in Table 7.2. GPU parallelized P-STAC, though much faster than a CPU serial code, requires significant computational time to simulate a spread of about 235,000 AM powder particles. So only 45 simulations for each of the three different substrates have been conducted using an n-factorial design of simulations approach on the lines of design of experiments approach carried out by Asadi et al. in 2016 ([33]). The different parameters for spreading simulations, involving a roller as a spreader, are summarized in Table 7.3. The substrate is assumed to have a normal distribution of heights with a standard deviation of 0, 46μm and 99μm. This range nicely covers the roughness value seen on a real 3D printed part shown in Fig. 7.2b. The skewness and kurtosis of the distribution of surface heights of the real 3D printed part are 0.15 and 3.34 respectively and are acceptable to assume a normal distribution. The substrates used in the spreading simulations have comparable striations per unit length as that seen in Fig. 7.2c. Sample simulation snapshots for three spreading cases are shown in Fig. 7.7, Fig. 7.8 and Fig. 7.9.

Figure 7.7 shows spreading of virtual 250μm Ti-6Al-4V powder over a flat substrate at spreader translation speed of 100mm/s and no rotation. While Fig. 7.8 and Fig. 7.9 show spreading of virtual 250μm Ti-6Al-4V powder over substrate with S_q of 46μm and 99μm at spreader translation speed of 100mm/s and rotation speed of 5rad/s and -5rad/s respectively. A black slit is shown on the spreader to

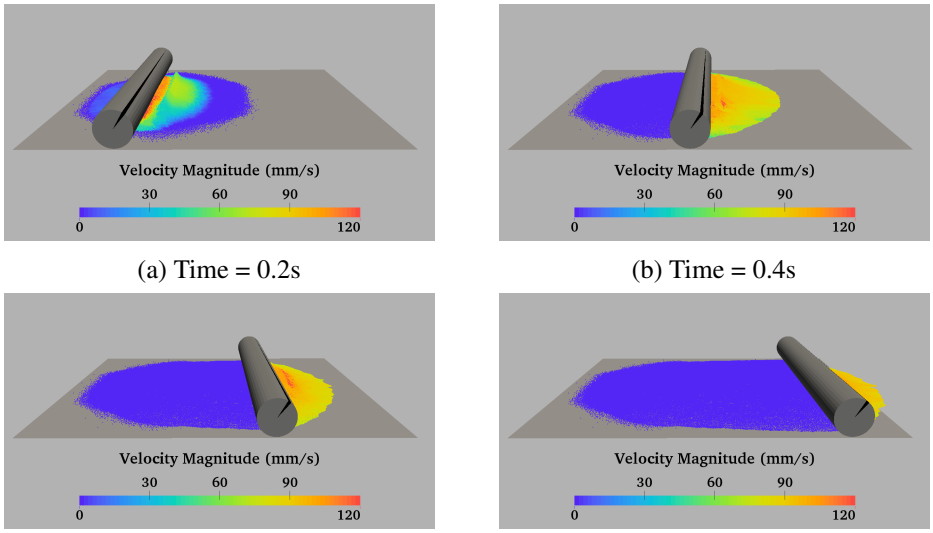

(a) Time = 0.2s (b) Time = 0.4s

(c) Time = 0.6s (d) Time = 0.8s

Figure 7.7: Simulation snapshots for virtual spreading with roller having U = 100mm/s and ω = 0 on a flat substrate. Particles are colored by values of their velocity magnitude.

better visualize the rotational motion of the spreader. The powder pileup in front of the spreader is largest in the case of the flat substrate and least in the case of clockwise rotating spreader as in this case 2 to 3 powder layers are deposited in one pass as opposed to the cases with no or anticlockwise spreader rotation. More powder gets used up in the cases of rougher substrates than the case of flat substrate. After the spreading simulation, the spread layer is critiqued for layer properties as described below. On an average, each spreading simulation took 45 minutes to run on an nVIDIA GTX 1070 GPU.

7.3.4 Spread Layer Characterization

A sampling region of Lx by Ly (here, 50mm by 50mm) centrally located above the substrate, after the spreading simulation has ended, can be sampled for many

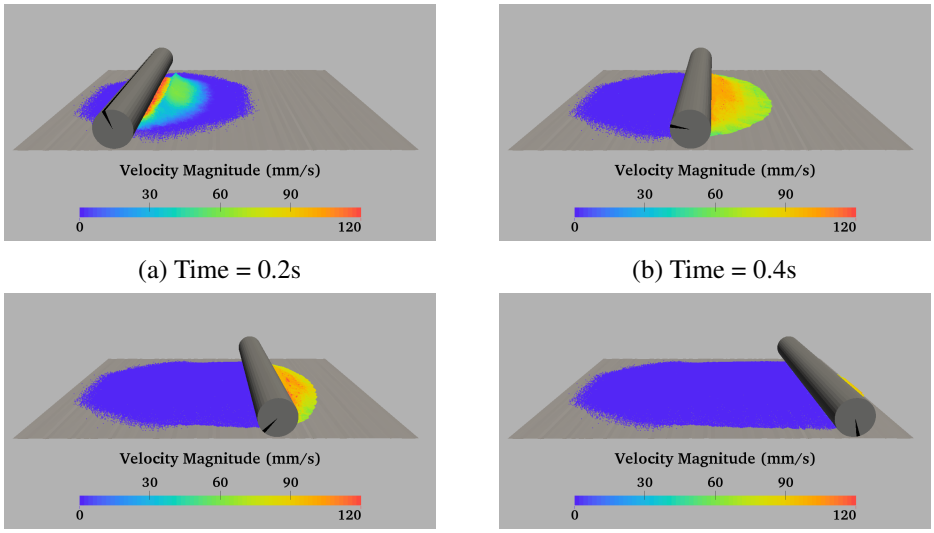

(a) Time = 0.2s (b) Time = 0.4s

(c) Time = 0.6s (d) Time = 0.8s

Figure 7.8: Simulation snapshots for virtual spreading with roller having U = 100mm/s and ω = 5rad/s on a substrate with $S_q = 46\mu$m. Particles are colored by values of their velocity magnitude.

important layer properties answering the following questions:

1. How *much* powder was spread in this sampling region?

2. How *fast* was this powder spread or the throughput of the spread?

3. How *rough* was the spread layer?

4. How *porous* was the spread layer?

The first question can be answered by measuring the mass of powder particles in the sampling region (M_S). The second by measuring the volume of powder spread per unit time per unit width of spreader or the throughput of the spread (Q_s). The third by measuring the roughness of the spread layer (R_q). While the fourth by measuring the porosity (Φ) of the spread layer. A prototyping application might

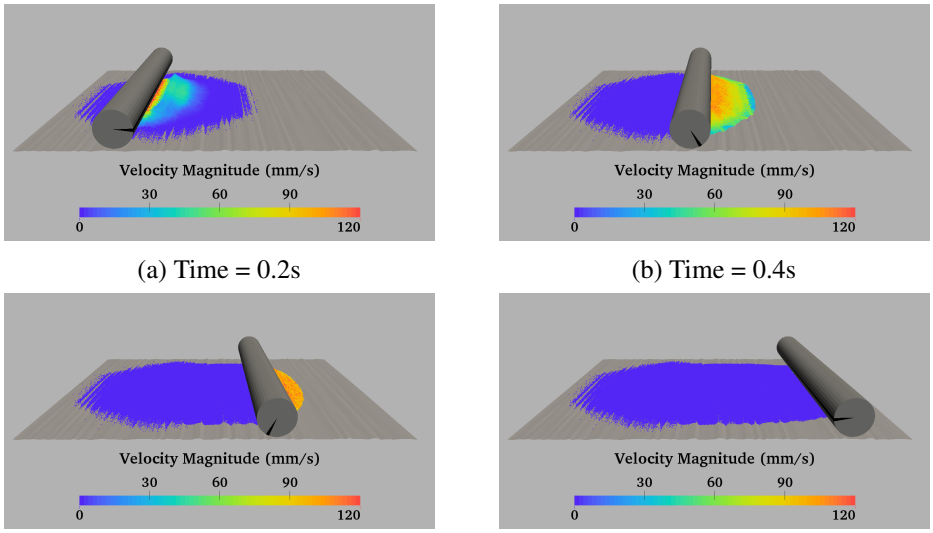

(a) Time = 0.2s (b) Time = 0.4s

(c) Time = 0.6s (d) Time = 0.8s

Figure 7.9: Simulation snapshots for virtual spreading with roller having U = 100mm/s and ω = -5rad/s on a substrate with S_q = 99μm. Particles are colored by values of their velocity magnitude.

require minimum porosity while an artistic application can discount porosity but might need least roughness. But all the applications desire maximum spreading throughput so as to 3D-print the object of interest in the least amount of time.

Figure 7.10 shows a generalized schematic of the side-view of a spread layer *i*. The heights of the previously 3D-printed layer layer *(i-1)* are denoted by *b's* while the heights of the post spread surface (consisting of fresh powder particles) are denoted by *h's*. In other words, *b's* are the heights registered by a virtual profilometer before the fresh powder was spread and *b's* are the heights measured by a virtual profilometer after the powder was spread. Notice the point of layer *(i-1)* denoted by b_3 where no powder was spread due to a steep peak. This point will be also registered as an *h* point for layer *i* while calculating its roughness.

The average height of layer *(i-1)*, denoted by b_{avg} and that of layer *i* denoted by

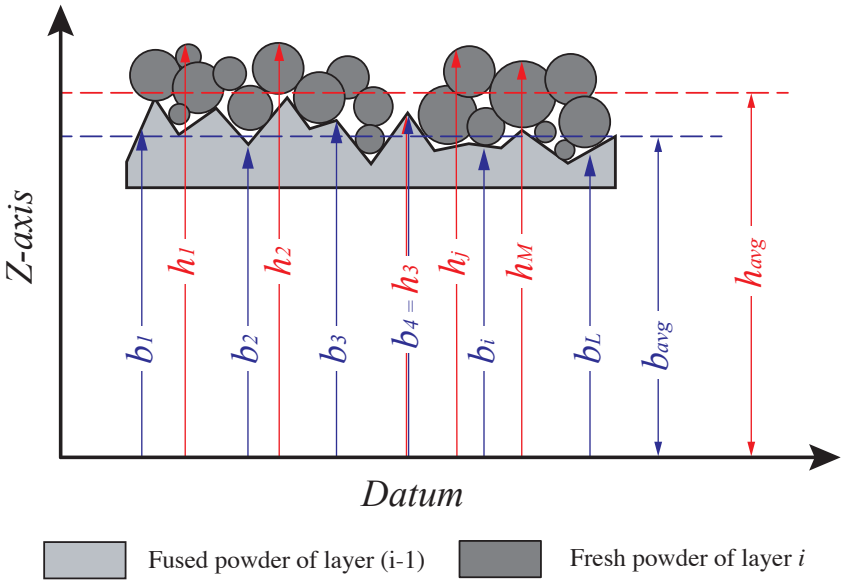

Figure 7.10: Schematic to understand computations of spread layer properties

h_{avg}, can be given by:

$$b_{avg} = \frac{\sum_{i=1}^{L} b_i}{L} \tag{7.10}$$

$$h_{avg} = \frac{\sum_{j=1}^{M} h_j}{M} \tag{7.11}$$

The average spread layer thickness can then be given by:

$$thk_{avg} = h_{avg} - b_{avg} \tag{7.12}$$

The quantities which answer the above four questions can be mathematically

obtained as follows:

$$M_s = \frac{4\pi\rho}{3}\sum_{k=1}^{N} {r_k}^3 \tag{7.13}$$

Here N is the number of powder particles in the sampling region of L_x by L_y. While ϕ_k is the diameter of the k^{th} particle and ρ is the material density of powder particles.

$$Q_s = U \cdot thk_{avg} \tag{7.14}$$

Where, thk_{avg} is given by 7.12 and U is the translation speed of the spreader.

$$R_q = \left[\frac{\sum_{j=1}^{M}(h_j - h_{avg})^2}{M}\right]^{\frac{1}{2}} \tag{7.15}$$

And finally,

$$\Phi = \left[1 - \frac{M_s}{\rho L_x L_y thk_{avg}}\right] \cdot 100\% \tag{7.16}$$

A 50mm by 50mm (L_x by L_y) region centrally located above the substrate, after the spreading simulation gets over, has been sampled for the throughput of the spread Q_s and the roughness of the spread layer R_q. The remaining layer properties are investigated in the next Chapter

The sampling regions for the cases shown in Figures 7.7, 7.8, 7.9 are shown in Fig. 7.11. The spread layer over a flat substrate, Fig. 7.11a, can be seen to have voids. These voids will result in porosity in the 3D printed part and can eventually cause failure of the part during loading. The spread layer over rough substrates can be seen to fill up the striations of the substrate. The case in which the substrate has

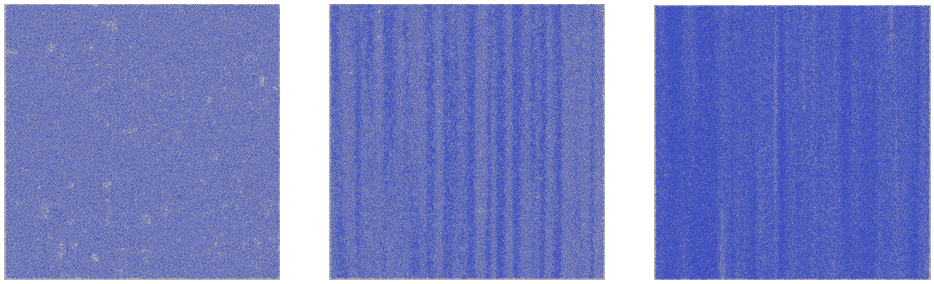

(a) (b) (c)

Figure 7.11: Sampling region of the spread layer used for measuring the layer properties Q_s and R_q: (a) U = 100mm/s and ω = 0rad/s on a flat substrate, (b) U = 100mm/s and ω = 5rad/s on a substrate with S_q = 46μm, (c) U = 100mm/s and ω = -5rad/s on a substrate with R_q = 99μm

maximum roughness, refer Fig. 7.11c, seems to have the densest layer. The values for Q_s and R_q for all the cases covered by the design of spreading simulations can be seen in Figs. 7.13, 7.14 (blue and black points).

7.4 Machine Learning based Spreading Predictions

The physics-based simulation results, as seen in Figs. 7.13, 7.14 (blue and black points), are highly non-linear and the simulation time, per spreading simulation, is quite high to perform a parametric study covering the entire range of spreader translation and rotation speeds, thereby resulting in a better understanding of the effect of these speeds on the spread layer properties Q_s and R_q. This problem is well suited to be solved using machine learning techniques to regress between the data obtained via design of spreading simulations from the previous section. Authors of this paper have chosen neural network to perform the regression over the datasets as neural networks [88] can generate an unbiased fit over a dataset than other regression techniques which have some assumptions about the function of the surface to be

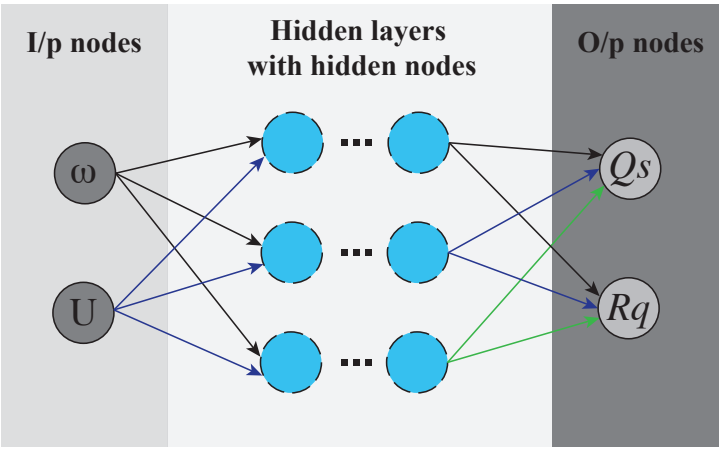

Figure 7.12: Schematic of a general neural network (NN) with multiple hidden layers with each hidden layer having multiple hidden nodes

regressed over the dataset [33–36].

7.4.1 Back Propagation Neural Network (BP-NN) [69]

A neural network is a mathematical model of a biological neuron. In real-living neurons, the dendrite receives electrical signals from the axons of other neurons, in the artificial neural network these electrical signals are represented as numerical values [88]. Generally, there are three kinds of layers in a neural network, namely input layer, hidden layer(s) and output layer, refer Fig. 7.12. The input layer is a vector of values which are given as conditions in the problem. Similarly, the output layer is also a vector of values which are the target solution for the problem. In the case of studying the effect of spreader speeds on the spread layer, the input layer vector is spreader translation speed U and spreader rotation speed ω and the output layer vector is made of spread layer properties Q_s and R_q, as defined in the previous section. There may be a single hidden layer or multiple hidden layers in the network

based on how the constructor defines the network. For this study, the NN comprises of a single hidden layer. Within each hidden layer, a vector of value is calculated using the data from the previous layer and these values are generated by the network to represent some feature of the data. Each layer is connected with the next layer using weights. These weights form a matrix of linear factors. The product of the vector from a certain layer and the weights matrix is the vector of the next layer. This means that each node in the next layer is a linear combination of nodes from the previous layer. However, this network has only linear functions. Many real problems often have complex nonlinear relationships between input and output. So, a nonlinear activation function is commonly used to make the network nonlinear and be able to learn some pretty complicated problems.

In the present study, sigmoid function, such $f(x) = \frac{1}{1+e^{-x}}$ or $f(x) = tan^{-1}(x)$, is used as an activation function. As the structure of the neural network has been defined, a useful way to train the network is back propagation (BP). In this training method, the target is the loss function which is commonly written as:

$$L = \frac{1}{N}\sum_{i=1}^{N} ||Y_i - O_i||^2 \tag{7.17}$$

where N is the total number of training data. Y_i is the actual output vector for the i^{th} training data. O_i is the target output vector for the i^{th} training data. The loss function is implemented to find the difference between the real output and the target output. Therefore the training process is actually finding the minimum of the loss function. Here, the gradient descent is implemented to minimize the loss function. The loss function can be regarded as a complex nonlinear function. A random initial point can be defined and the direction where the function has the fastest decreasing

speed can be found by calculating the derivative on that point. Then a step along the function is taken with a fixed step size and the new point is acquired. Using similar way for many iterations, the point will get closer and closer to the minimum point.

As we train the neural network, first, the weights are just randomly generated. Then outputs are calculated from the inputs and the random weights. Finally, the loss function value can be obtained and used as the updates for the weight:

$$W^{(n+1)} = W^{(n)} - \alpha \Delta W \tag{7.18}$$

where

$$\Delta W = \frac{\partial L}{\partial W} \tag{7.19}$$

In the above equations, α is the learning rate which will control the step size of gradient descent in each iteration. If α is too small, it may take a large number of iterations for the loss function to come to convergence. However, if α is too large the learning process may crash when the network is training. Oscillations will occur on the loss function value for each iteration.

Another main challenge of training the network is overfitting where the training error is decreasing but testing error is increasing. Usually the reason is that the complexity of the network becomes much higher than the data itself and the weights have large magnitude. Hence L-2 regularization is implemented in the loss function to avoid overfitting:

$$L = \frac{1}{N} \sum_{i=1}^{N} ||Y_i - O_i||^2 + \lambda ||W||^2 \tag{7.20}$$

In the new loss function, the norm of all the weight is put into the loss function and λ is the parameter to control the level of regularization. In this way, as the loss

function decreases, the magnitude of all the weights is secured to be small.

The parameters used for BP-NNs used to regress between the spreader speeds and spread layer properties are listed in Table 7.4. Number of hidden nodes was decided by conducting a parametric study involving BP-NNs with increasing number of hidden nodes and 200 was chosen as a trade-off between accuracy and computational efficiency. The learning rate and L2-regularization parameter were also decided by conducting numerical experiments but for the brevity of the paper these analyses are not presented. Regression results from the final BP-NN with parameters listed in Table 7.4 are shown in Fig. 7.13 and Fig. 7.14 for spreading simulations over a flat substrate. The surfaces predicted by this BP-NN, refer Fig.

Table 7.4: BP-NN parameters for spreading simulations over a particular substrate

Parameter	Value	Parameter	Value
Number of training samples	35	Activation function for hidden layer	Sigmoid
Number of test samples	10	Activation function for output layer	Linear
Number of hidden layers	1	Learning rate α	0.0001
Number of hidden nodes	200	L2-regularization parameter λ	0.1

Table 7.5: BP-NN performance matrix

Q_s				
Substrate Sq (μm)	Normalized RMS error (%)		Correlation coefficient	
	For training samples	For test samples	For training samples	For test samples
0	1.74	2.21	0.9938	0.98463
46	1.97	2.94	0.99537	0.98768
99	5.46	2.69	0.9954	0.99622
R_q				
Substrate Sq (μm)	Normalized RMS error (%)		Correlation coefficient	
	For training samples	For test samples	For training samples	For test samples
0	1.99	2.27	0.98264	0.98175
46	0.83	0.93	0.97348	0.95751
99	1.1	0.92	0.98201	0.97227

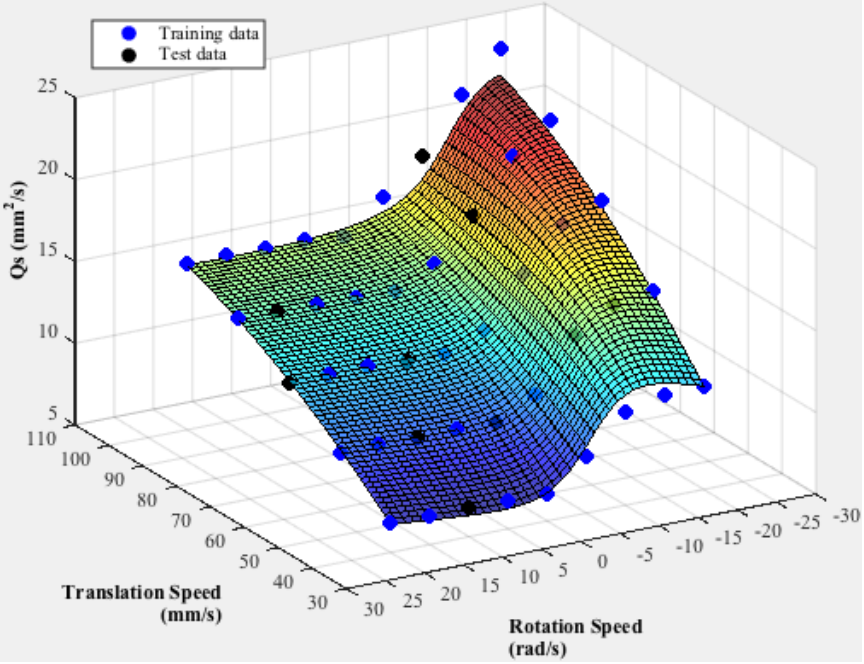

(a)

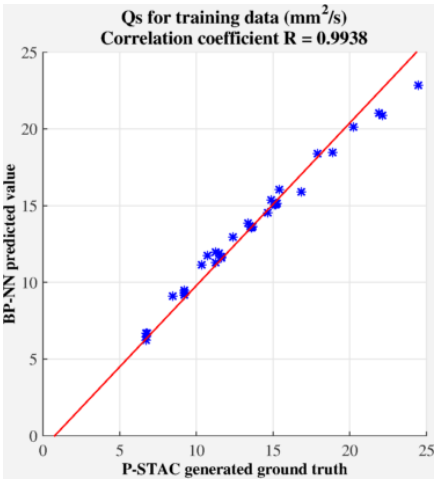

(b)

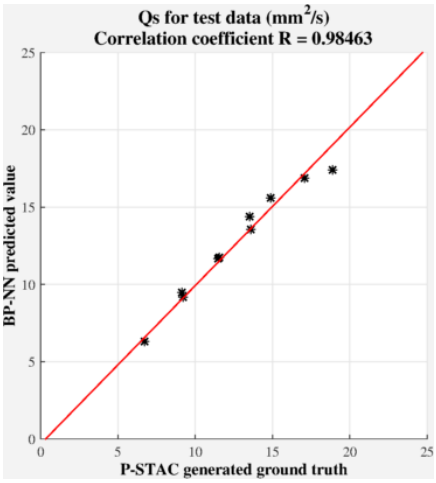

(c)

Figure 7.13: BP-NN regressed surface for Q_s for the case of spreading of flat substrate

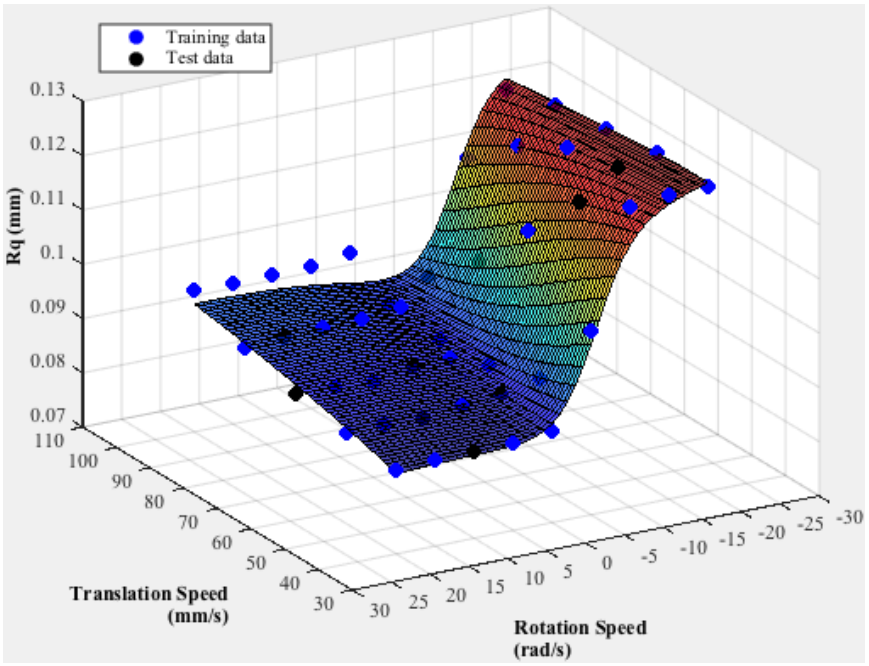

(a)

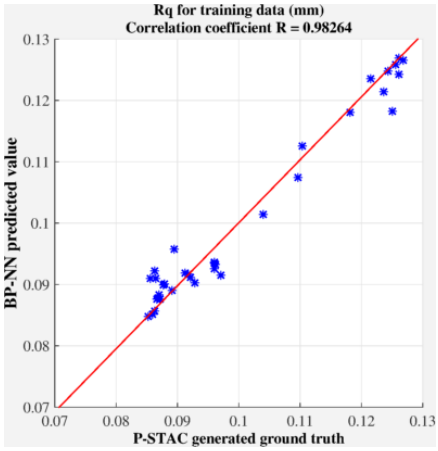

(b)

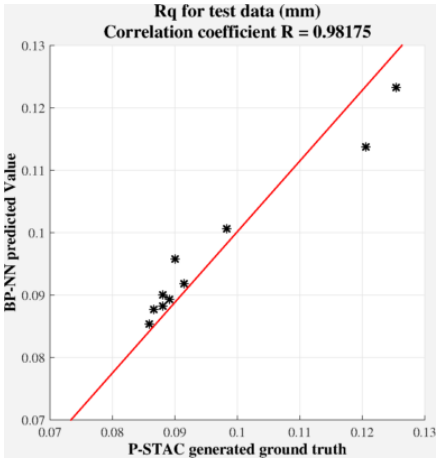

(c)

Figure 7.14: BP-NN regressed surface for R_q for the case of spreading of flat substrate

7.13a and Fig. 7.14a, nicely blanket the simulation data points, both training and test data points, generated via design of simulations. Also shown is the correlation coefficient R between simulation results and predicted results in Figs. 7.13a, 7.13b and Figs. 7.14a, 7.14b. The near unity value of R for both training and test data points for each of the layer properties Q_s and R_q, suggests a near perfect regression. The error values and R values for the three substrates are listed in Table 7.5. Three separate BP-NNs trained for three cases of varying substrate roughness are able to predict results with at least 95% accuracy. The normalized RMS error reported in the Table 7.5 refers to the root mean square of the error in predicted spread layer properties by BP-NN with respect to the ground truth generated using P-STAC and normalized by the range of the corresponding value.

7.4.2 Spreading Process Maps

Spreading process maps, similar to binding process maps as shown in works of [33, 71, 72], are shown in Figs. 7.15, 7.16 and 7.17 for three different substrate roughness values. These process maps relate the 3D printer spreader parameters of translation U and rotational speeds ω to the spread layer properties of Q_s and R_q. From flat to the roughest substrate, efficiency of spreading which is indicated by a larger Q_s, increases for the same U-ω pairs. The variation in roughness values is much more for a smooth substrate than rough substrates as the spread powder is used up to level off a rough substrate. In all the three substrates (Figs. 7.15, 7.16 and 7.17), the R_q of the spread layer increases as the rotation of spreader changes from anticlockwise (+) to clockwise (-) direction. This is due to the clockwise spreader rotation forcing spread of multiple layers as opposed to only one to two layers in the cases of no and anticlockwise rotational motion. For a constant rotational speed ω,

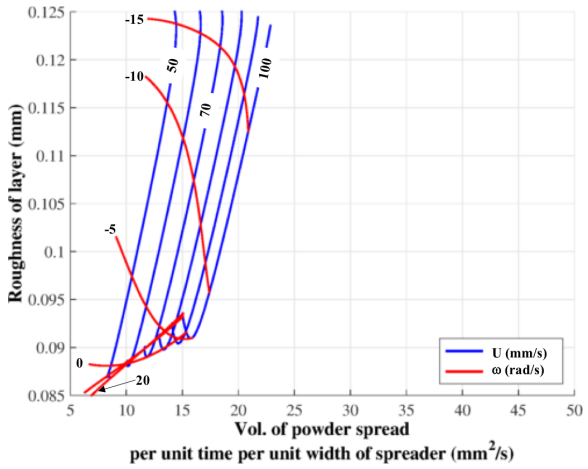

Figure 7.15: Spreading process maps relating the Q_s and R_q of the spread layer to the translation speed U and rotation speed ω of the spreader for flat substrate

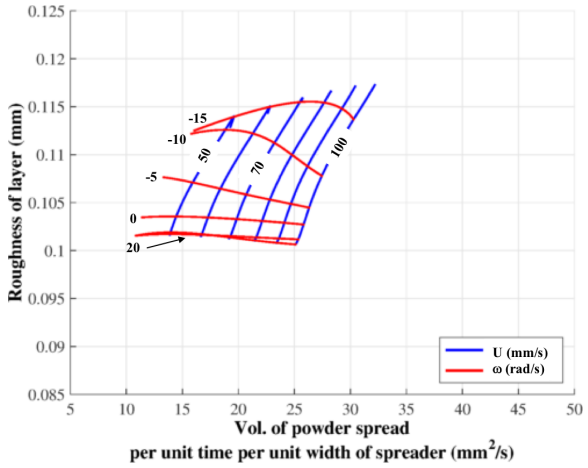

Figure 7.16: Spreading process maps relating the Q_s and R_q of the spread layer to the translation speed U and rotation speed ω of the spreader for substrate with S_q = 46μm

the efficiency of spread increases at the translational speed increases. Conversely, the most efficient way to spread a layer, which is indicated by a larger Q_s, of known roughness is to obtain the rightmost U-ω pair on the process map.

For a constant ω, the variation in R_q with increasing U inverts from concave up

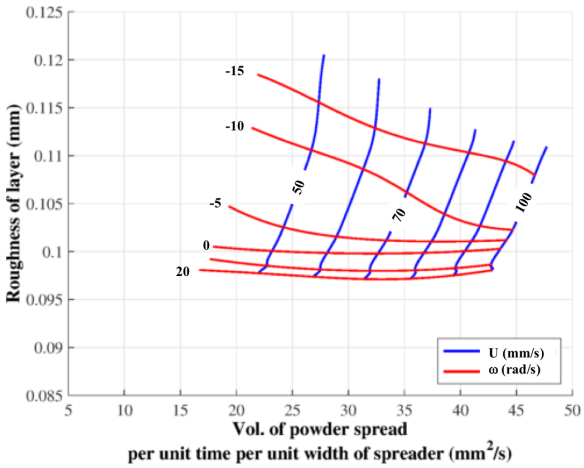

Figure 7.17: Spreading process maps relating the Q_s and R_q of the spread layer to the translation speed U and rotation speed ω of the spreader for substrate with S_q = 99μm

to concave down as the sign of rotation changes from positive (anti-clockwise) to negative (clockwise).

7.5 Conclusions

To conclude, a synergistic framework based on DEM modeling and machine learning has been presented in this study to provide spreading predictions in powder-bed AM techniques. An accurate particle tessellated surface interaction scheme is introduced to be used along with DEM and is successfully applied to simulate spreading of virtual Ti-6Al-4V powder, which is modeled as 235,000 smooth spherical, cohesionless particles, on substrates having three different roughness values. Back propagation neural network is used to regress between the highly non-linear spread layer properties as a function of spreader speeds. The spreading process maps thus developed can be made available to a 3D printer operator to efficiently

print parts at desired roughness values within the intervals of contours on spreading process maps. These maps can also serve the function of forcefully introducing roughness in the spread layer to offset the uneven temperature distribution which is often encountered in the electron beam or laser based binding processes and thereby result in a smooth and uniform build or 3D printed layer.

Acknowledgements

Authors of this work would like to acknowledge SEM imaging of Ti-6Al-4V powder from Ross Cunningham and Anthony Rollett. We also thank Luke Schime and Jack Beuth for the 3D printed cylinder. Finally, we thank Recep Onler and Burak Ozdonglar for the roughness image of the 3D printed cylinder.

Nothing is more intolerable than to have to admit to yourself your own errors
-Ludwig van Beethoven

Chapter 8

Considering Polydispersity in Spreading: Modeling and Experimental Validation

Nomenclature

Symbol or Acronym	Meaning
ε	Coefficient of restitution
μ	Coefficient of sliding friction
U	Translation speed of the spreader
ω	Rotational speed of the spreader
AM	Additive Manufacturing
PSD	Particle Size Distribution
Q_s	Volume of the powder spread per unit time per unit width of spreader
R_q	Roughness of the spread layer
M_s	Mass of the spread powder in the sampling region
Φ	Porosity of the spread layer
S_q	Roughness of the substrate
R	Correlation coefficient

8.1 Introduction

Metal AM powders rarely have a uniform particle size distribution (PSD), as was assumed in the previous chapters. Particle size distribution brings in new phenomena of segregation and particle agglomeration which cannot be modeled by a virtual particulate media having a uniform particle size distribution. However, the number of particles to be simulated increases drastically and the time step of the simulation goes down. This increases the total simulation time.

This Chapter tries to develop a virtual avatar of Ti-6Al-4V powder by considering a normal PSD (Section 8.2), based on the calibration process introduced in Chapter 7. A retrofit for the ExOne Innovent 3D printer for performing single layer spreading is developed and single layer spreading experiments have been carried out with an industry grade AM powder (Subsection 8.3.1). Behavior of virtual avatars, with and without PSD, of the aforementioned AM powder is tested in single layer spreading simulations modeled close to the single layer spreading experiments (Subsection 8.3.4) and finally machine learning predictions are provided for spreading with virtual avatar having PSD (Section 8.4)

8.2 Virtual avatar of Ti-6Al-4V with polydispersity

The Ti-6Al-4V powder used in this study had particle sizes in the range of 100 and 250 μm, as specified by the manufacturer. This is the same Ti-6Al-4V powder considered in Chapter 6. A normal or Gaussian PSD with a mean of 175 μm as shown in Fig. 8.1. is considered in this chapter to account for the polydispersity in the real Ti-6Al-4V powder. Calibration process as described in Section 6.3, is used to generate a virtual avatar of the Ti-6Al-4V powder which behaves qualitatively

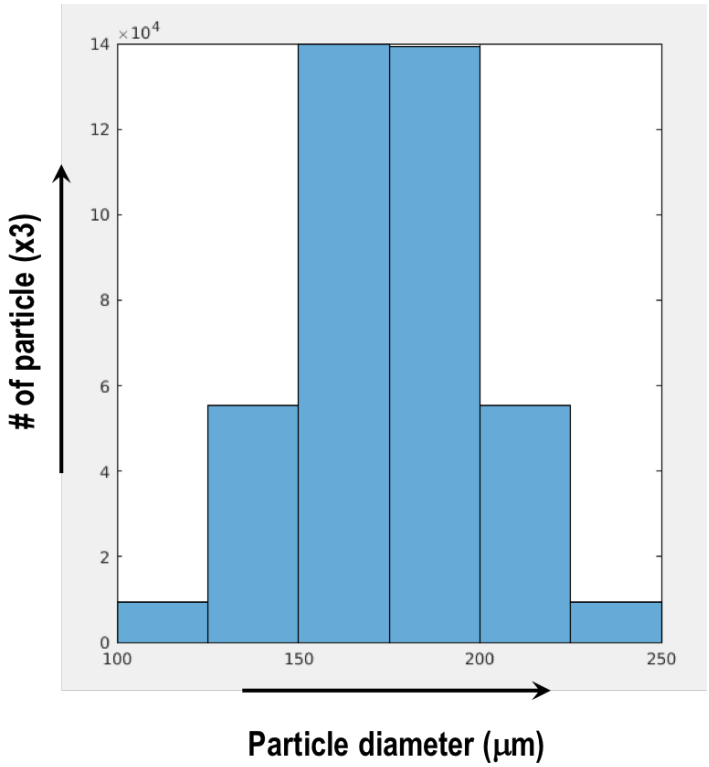

Figure 8.1: PSD used in the DEM simulations of Ti-6Al-4V powder

(angle of repose testing) and quantitatively (powder rheometry testing for small fill height at impeller blade tip speed of 100mm/s) to the real Ti-6Al-4V powder.

Figure 8.2 shows simulation snapshots for the 23.5mm diameter virtual rheometer with polydispersed Ti-6Al-4V powder for blade tip speed of 100mm/s. This simulation has around 1.2 million particles. Inclusion of PSD increases the particle count from 435,000 uniform sized (250microns) particles (Chapter 6) to 1.2 million particles. The time step of this simulation is governed by the smallest sized particle and the stiffest spring. The rotational speed of blade is 8.48 rad/s and its downward translational speed is 8.72mm/s. The angle of the helix formed by the motion of the

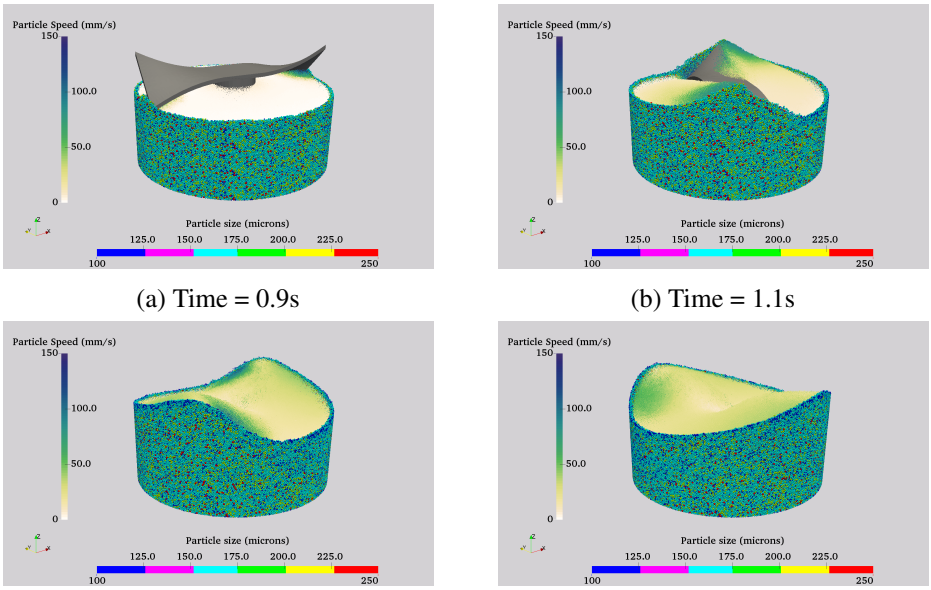

(a) Time = 0.9s (b) Time = 1.1s

(c) Time = 1.5s (d) Time = 1.7s

Figure 8.2: Simulation snapshots for confined compressive loading inside 23.5mm virtual rheometer with 100-250μm Ti-6Al-4V powder

blade is -5°. In Fig. 8.2, the particles near the wall of the cylindrical vessel have been displayed as spheres which are scaled and colored by their particle sizes while the remaining particles are displayed as points and are colored by their speed. As the blade penetrates the virtual powder, the smallest sized particles can be seen to form a ring at the top, occupying the space between the impeller blade's edge and the inner wall of the cylindrical vessel. This can be attributed to the segregation tendency in a polydispersed particulate media. Note, only small fill height of 14mm, based on the fill height independence study described in Section 6.4, was used to calibrate for the micro-properties. The final tuned micro-properties are presented in Table 8.1. These values are based on the guess values of Vmax as 80mm/s and Δ_{max} as 0.5% of particle diameter. Again, the calibration algorithm iteratively changes Vmax such

Table 8.1: Contact interaction parameters used in DEM ploydispersed rheometry and spreading simulations

Property	Ti-6Al-4V powder interacting with			
	Ti-6Al-4V powder	rheometer vessel	spreader	3D printed substrate
ε	$0.8^{\#}$	$0.8^{\#}$	$0.8^{\#}$	$0.8^{\#}$
μ	0.22*	0.2*	$0.12^{@}$	$0.25^{\#}$

Note: * = value tuned via the DEM calibration process,
$^{@}$ = value measured using rheometer,
$_{\#}$ = assumed value

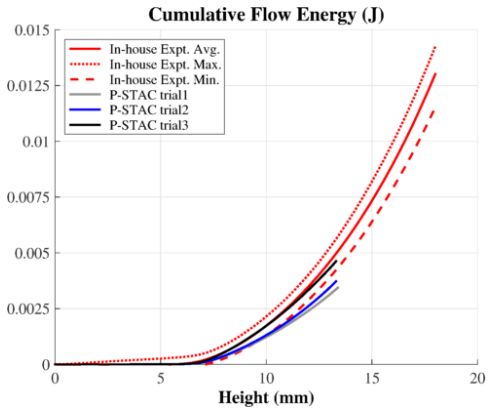

Figure 8.3: Energy response for 23.5mm virtual rheometer with 100-250μm Ti-6Al-4V powder denoted by P-STAC trials

that the area under cumulative energy curves is within acceptable tolerance when compared to the experimental values. The three corresponding trials are also shown in Fig. 8.3. The energy response predicted by P-STAC trial3 matches well with the in-house experimental data. This calibrated DEM model of polydispersed Ti-6Al-4V powder is referred to as the virtual avatar of the real 100-250μm Ti-6Al-4V powder. Refer Chapter 6 for the virtual avatar of the real 100-250μm Ti-6Al-4V powder modeled as monodispersed media with 250μm particles.

8.3 Single layer spreading

8.3.1 Experiments

It is difficult to isolate spreading of a single layer in the current state-of-the-art 3D printers and characterize the layer for spread properties which were introduced in Chapter 7. Also, it is necessary to perform spreading on a platform which has been 3D printed with the same powder. With this in mind, an easy to handle, multi-purpose retrofit, as shown in Fig. 8.4, has been designed for an ExOne Innovent 3D printer to experimentally study single layer spreading. While performing spreading experiments, following precautions must be observed:

1. Spillage and dust cloud formation of AM powders must be avoided as these powders are metallic in nature and can cause breathing problems, if inhaled. Proper respirator, an apron, a pair of goggles and a pair of gloves must be

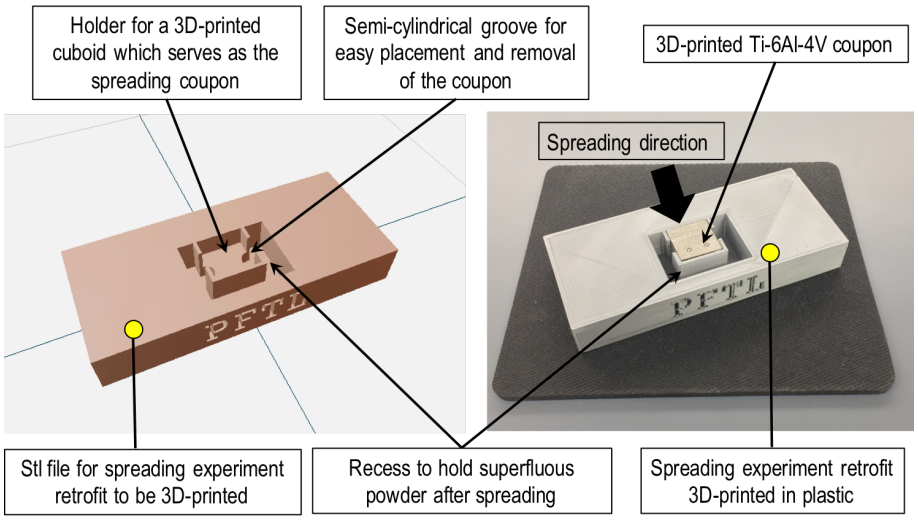

Figure 8.4: Retrofit to study single layer spreading on a 3D printed coupon for ExOne Innovent 3D printer

used at all times [89].

2. Also, the dust cloud of explosive powders like Ti-6Al-4V should not come in contact with any object which can carry an electrostatic charge [89].

The retrofit shown in Fig. 8.4 has been designed to avoid any spillage of superfluous powder. The Ti-6Al-4V powder used in this study has considerably larger particle sizes as compared to the powders used in EOS or Arcam 3D printers. Hence the probability of the dust cloud formation is minimum. The retrofit itself has been 3D printed in plastic. The coupon which is a 3D printed cuboid of Ti-6Al-4V, represents the spread and fused layer *(i-1)* on top of which layer *i* will be spread at varying spreader speeds. The coupon itself can be 3D printed at varying process parameters and materials, hence the multi-purpose nature of this retrofit.

Figure 8.5 shows how to use this retrofit to study single layer spreading in ExOne Innovent 3D printer. Following steps must be carried out:

1. Place the 3D printed coupon, here 3D printed Ti-6Al-4V cuboid, in the coupon holder of the retrofit and place the retrofit on top of the print platform of the ExOne Innovent.

2. Lower the print platform such that the top surface of the retrofit is flushed with the outer edge of the build box.

3. Deliver a fixed volume of powder, here this is done using a black plate with a cuboid hole, in front of the coupon. This volume must be sufficiently large so that the powder can cover (after spreading) the entire top surface of the coupon.

4. Perform single pass of spreader, here a roller as seen in Fig. 8.6, at a particular translation and rotation speeds and observe the spread layer. In the present case of Ti-6Al-4V powder, no changes in spread layer (for different spreader speeds) could be seen by naked eye. The distance of the lower most point of the spreader from the top surface of the coupon was around 300μm. In other words, the layer height was about 300μm.

5. Carefully move the print platform up and remove the retrofit. The retrofit along with the coupon and the spread layer can now be carried to layer characterization rig(s). In the present study, only the mass of the powder M_s which remained on the top surface of the coupon has been measured and compared to the simulation results in Subsection 8.3.4. Other layer properties

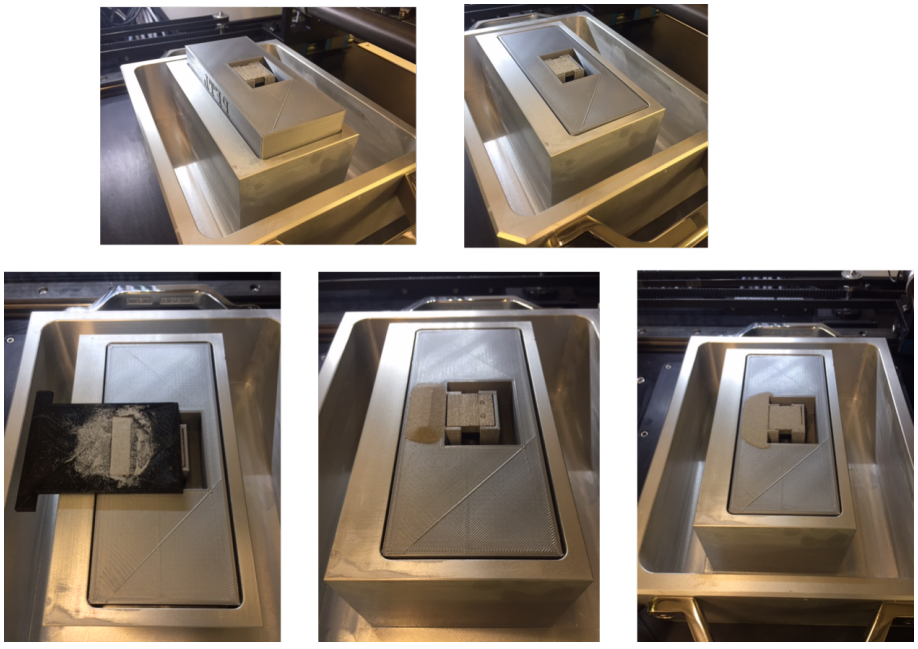

Figure 8.5: Snapshots of steps involved in studying single layer spreading on a 3D printed coupon (top-left to bottom-right)

(a) Time1 (b) Time2

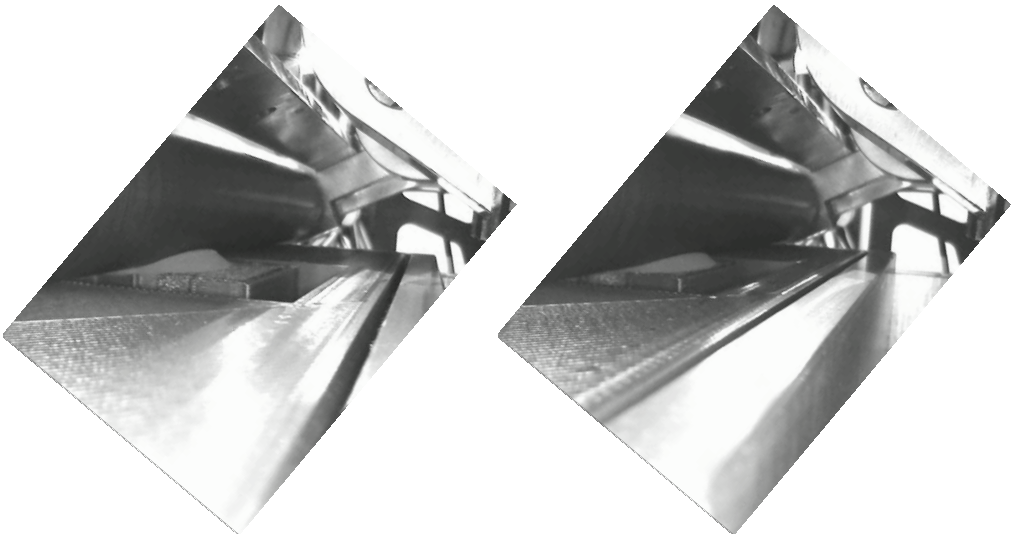

(c) Time3 (d) Time1

Figure 8.6: Experimental snapshots for real spreading inside ExOne Innovent with the spreading retrofit for 100-250μm Ti-6Al-4V powder

like layer roughness and porosity are difficult to measure experimentally.

The experimental snapshots shown in Fig. 8.6 were obtained by attaching an

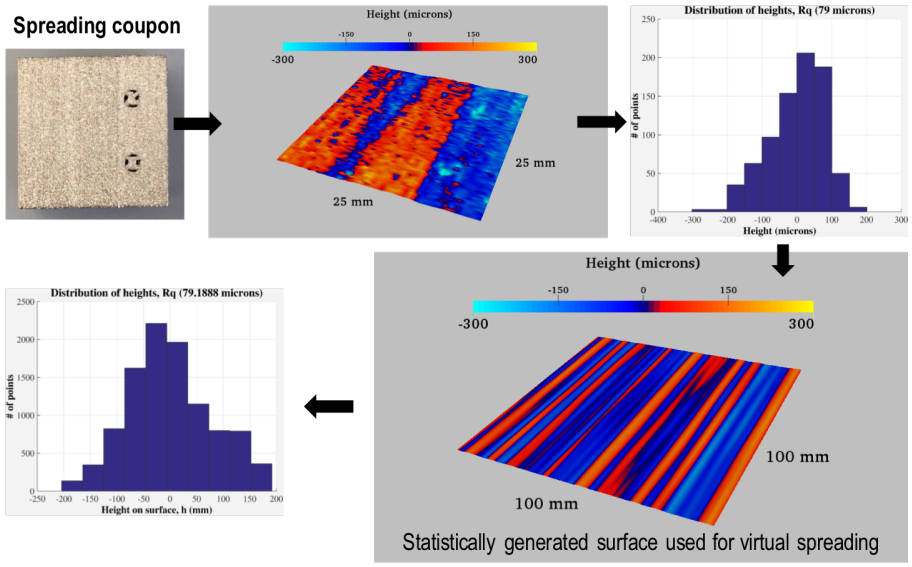

Figure 8.7: Steps showing the progress from the real spreading coupon (top left) surface roughness measurements to generating virtual surface to be used for virtual spreading

endoscope in front of the spreader.

8.3.2 Modeling

Single layer spreading simulations on a substrate having roughness similar to the top surface of the spreading coupon (on which experimental spreading was conducted in the previous sub-section) have been carried out by following the approach described in Section 7.3.

Figure 8.7 shows the spreading coupon along with its surface topography. The roughness of the top surface of the spreading coupon is 79μm. Fig. 8.7 also shows the statistically generated surface which has the roughness similar to the real substrate and has striations per unit length comparable to the real one. Note that the virtual spreading is carried out on a larger substrate (100mm by 100mm) and a

region of 25mm by 25mm, referred to as the sampling region (which is equal in size when compared to the top surface of the real spreading coupon), is used to study the layer characteristics to be described in the next subsection. Fig. 8.8 shows spreading of virtual 100-250μm powder over substrate with S_q of 79μm at spreader translation speed of 100mm/s and rotation speed of 5rad/s. A black slit is shown on the spreader to better visualize the rotational motion of the spreader. The simulation consisted of 435,000 DEM particles. The heap of particles is considerably smaller than the heaps seen in virtual spreading simulations with uniform particle sizes (Fig. 7.7, Fig. 7.8 and Fig. 7.9). After the spreading simulation, the spread layer is critiqued for layer properties as described below. On an average, each spreading simulation with PSD took 2 hours to run while the ones without PSD took 45 minutes to run on an nVIDIA GTX 1070 GPU.

A better visualization of the tribosystem which involves Ti-6Al-4V particulate media trapped between sliding-and-rolling spreader and the 3D printed substrate is shown in Fig. 8.9 by zooming near the center half of the spread layer. Powder particles fill up the valleys formed by the surface topography of the substrate while the peak-like features of the substrate are not fully covered by the powder particles at the end of the spreading. This, partial coverage can result in porosity in the 3D printed object. Also, the spread layer formed is highly sensitive to the substrate features and it does not look repeatable along the axis of the spreader. Hence, it is important to carry out a 3D simulation covering bigger domain as has been done in the present study; other studies in the literature have not accounted for this effect [83–86].

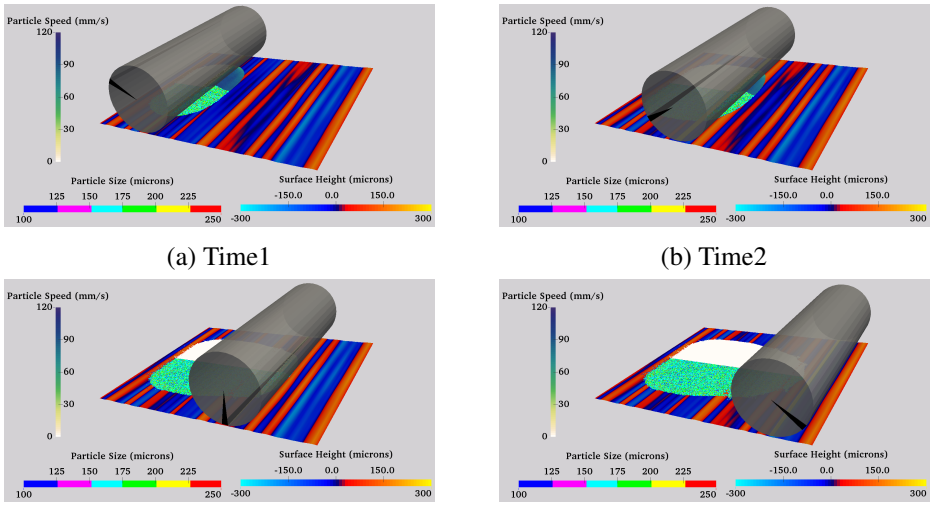

(a) Time1

(b) Time2

(c) Time3

(d) Time4

Figure 8.8: Simulation snapshots for virtual spreading with roller having U = 100mm/s and ω = 5rad/s on a substrate with S_q = 79μm. Particles on the front half are colored by values of their sizes and those on the back half are colored by their speeds. The substrate is colored by surface heights.

8.3.3 Spread layer characterization

A 25mm x 25mm region centrally located above the substrate, after the spreading simulation has completed, is sampled for four important properties (as described in Section 7.3): the mass of the powder in the sampling region, M_s, the volume of powder spread per unit time per unit width of the spreader, Q_s, the roughness of the spread layer, R_q and the porosity of the spread layer,Φ. Out of these, only M_s can be measured easily for real spreading experiments and this is the property against which the computational model will be validated in the next sub-section. Q_s is indicative of the efficiency of the spreading while R_q is indicative of the qualitative aspect of the layer. The optimum values for Q_s, R_q and Φ depend on the AM application. The sampling regions for virtual spreading with and without

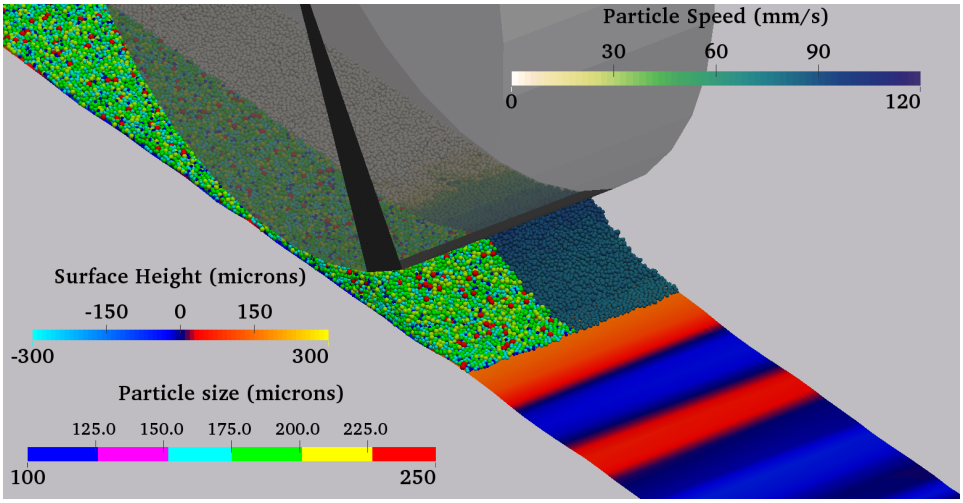

(a) Time = 0.36s

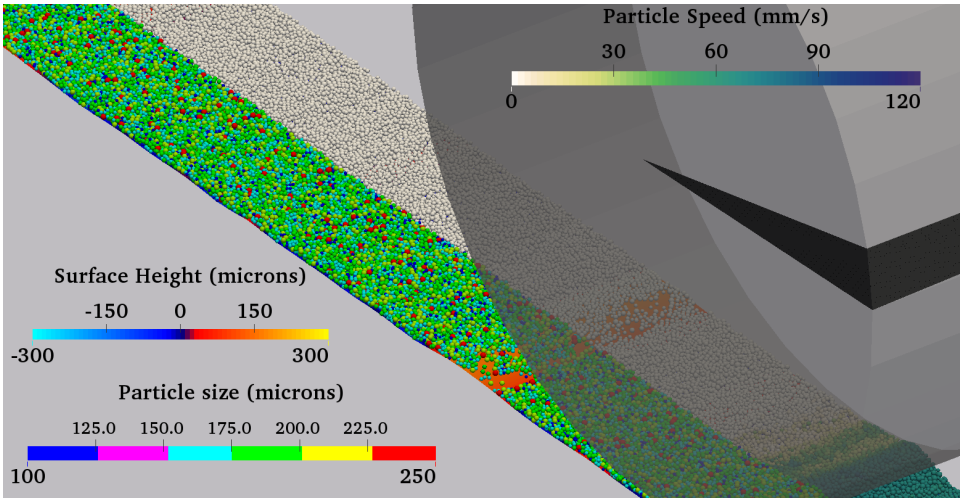

(b) Time = 0.60s

Figure 8.9: **Zoomed-in** simulation snapshots for virtual spreading with roller having U = 100mm/s and ω = 5rad/s on a substrate with S_q = 79μm. Particles are scaled by their sizes; those on the front half are colored by values of their sizes and those on the back half are colored by their speeds. The substrate is colored by surface heights.

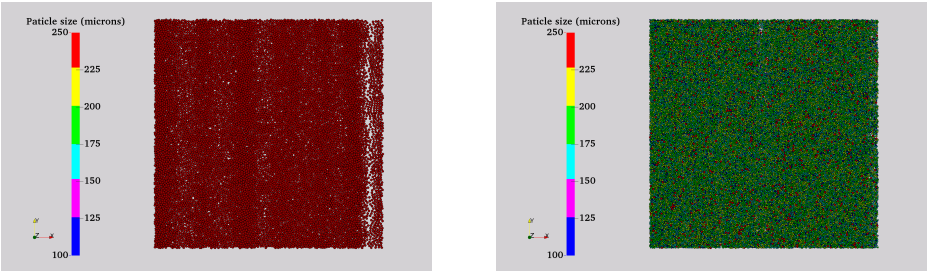

(a) Without PSD (b) With PSD

Figure 8.10: Top view of sampling region (of the spread layer) used for measuring the layer properties after virtual spreading with roller having U = 100mm/s and ω = 5rad/s on a substrate with $S_q = 79\mu$m.

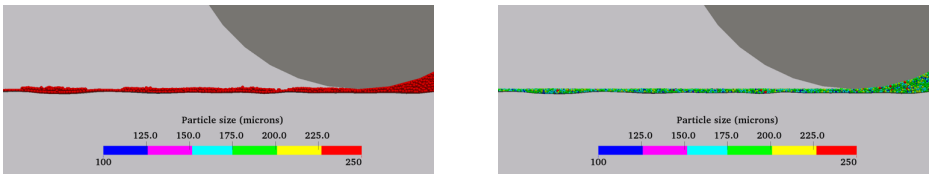

(a) Without PSD (b) With PSD

Figure 8.11: Side view of the spread layer used used for measuring the layer properties after virtual spreading with roller having U = 100mm/s and ω = 5rad/s on a substrate with $S_q = 79\mu$m.

PSD are shown in top view in Fig. 8.10 and in side view in Fig 8.11. The higher Φ and R_q for the spreading simulation with uniform particle sizes when compared to spreading simulation with PSD is evident from these figures. In the case with PSD, finer particles are able to fill in the gaps created by the larger particles and thereby create a better packing (Fig. 8.10b) and smoother layer (Fig. 8.11b).

8.3.4 Experimental validation

Of the various spread layer properties introduced in Chapter 7, the only spread layer property which can be easily measured after performing spreading experiments

is the mass of the powder left on the spreading coupon, M_s. Fig. 8.12 shows M_s for the experimental spreading along with the simulation results. All the spreads were carried out at a translation speed of 100mm/s and varying rotational speeds. As the rotational speed (in the direction of translation) increases, the impact with which the roller surface interacts with the powder increases and thereby more energy is imparted to the powder. This causes powder particles to disperse easily when compared to lower impacts which occur at lower rotational speeds. Therefore a decline in M_s (single spread expt. line) can be seen with increase in rotational speeds. The P-STAC simulations which did not account for PSD in the virtual powder were not able to predict this declining trend in M_s. Since there were no fine particles to fill up the voids generated by the larger particles, there was no appreciable change in the mass in the sampling region for P-STAC simulations which did not account for the PSD. However, the declining trend in the M_s has been captured when PSD was considered in the virtual spreading.

Figure 8.13 shows the R_q predicted by P-STAC simulations with and without PSD. The simulation results for the cases without PSD over predict the roughness of the spread layer. This is foreseeable as the particles making up the layer are much larger in case of simulation without the PSD than in the case of simulation with the PSD. This higher roughness can also be seen in the side view images shown in Fig. 8.11. PSD does seem to be an important attribute of the physics of particles dynamics which must be included while trying to study this AM tribosurface. But this higher fidelity comes at an added computational cost. Fig. 8.13 shows the drastic increase in the number of particles found in sampling region for the simulation cases with PSD when compared to the ones which had uniformly sized particles.

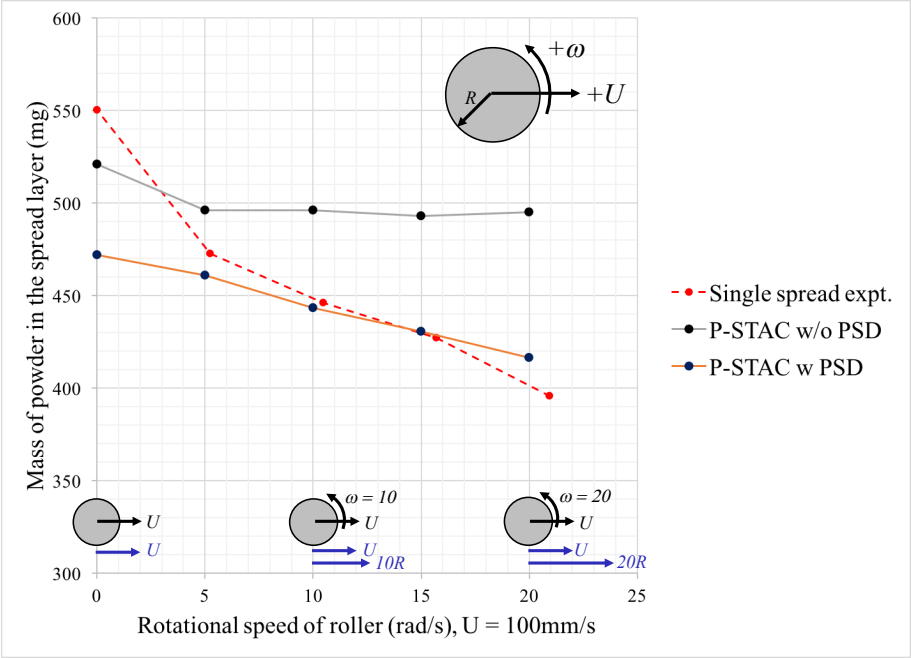

Figure 8.12: Variation of spread layer property M_s with changing spreader rotational speeds: Experiments and Modeling

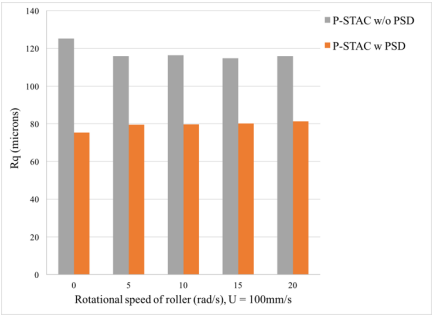

(a) R_q of the spread layer

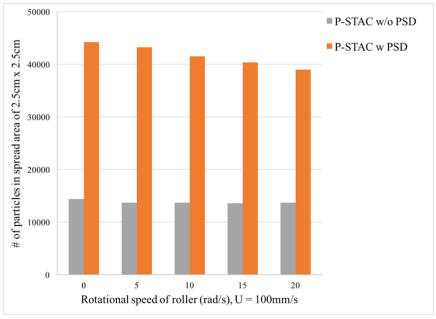

(b) Number of particles in the sampling region

Figure 8.13: Single layer spreading simulations with and without PSD

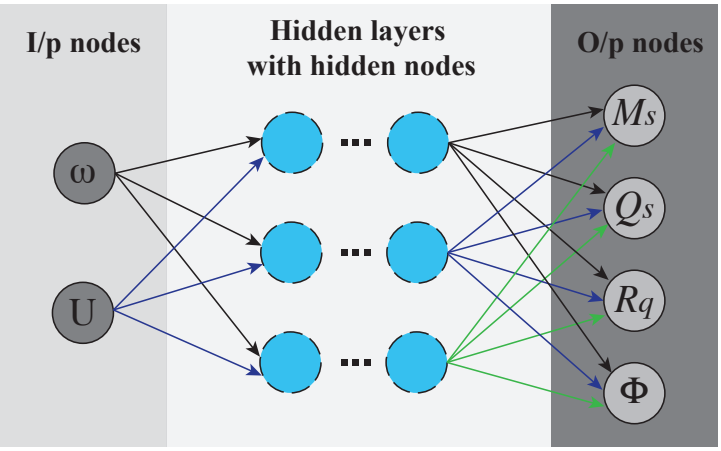

Figure 8.14: Schematic of a general neural network (NN) having 2 input nodes and 4 output nodes, with multiple hidden layers with each hidden layer having multiple hidden nodes

Table 8.2: Design of Simulations (DoS) for virtual spreading with PSD

Parameter	Range of values
Spreader diameter (mm)	10
Spreader length (mm)	70
Spreader translation speed, U (mm/s)	40, 55, 70, 85, 100
Spreader rotation speed, ω (rad/s)	0, 5, 10, 15, 20, -5, -10, -15, -20
Substrate roughness S_q (μm)	79

8.4 Design of Simulations for virtual spreading and Machine Learning predictions

GPU P-STAC with PSD can be used to provide predictions about the spread layer characteristics by varying the translation and rotational speeds of the spreader. Similar to the Design of Simulations (DoS) described in Section 7.3, DoS can be carried out to understand the behavior of virtual particulate media with PSD under different spreading conditions. The different parameters for spreading simulations

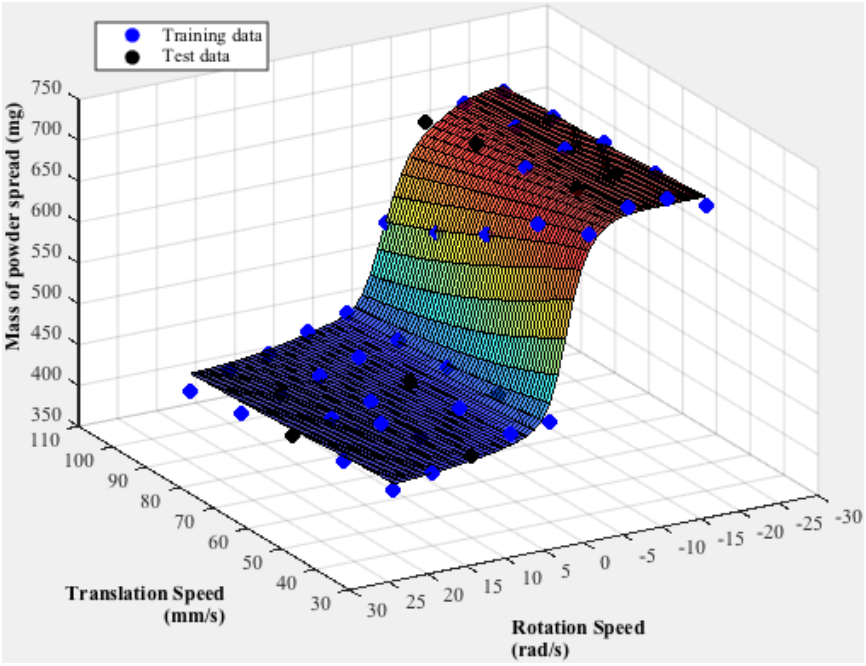

(a)

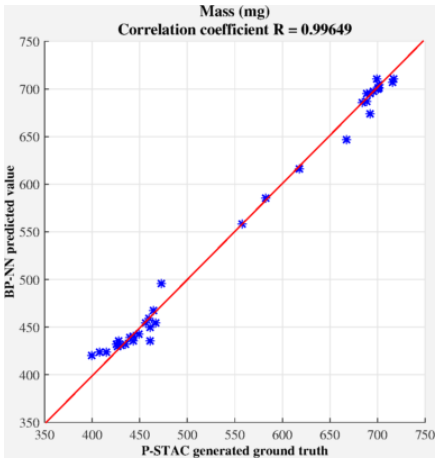

(b)

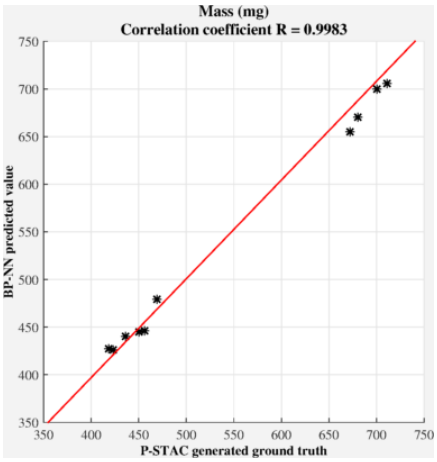

(c)

Figure 8.15: BP-NN regressed surface for M_s for the case of spreading on substrate with $S_q = 79\mu$m

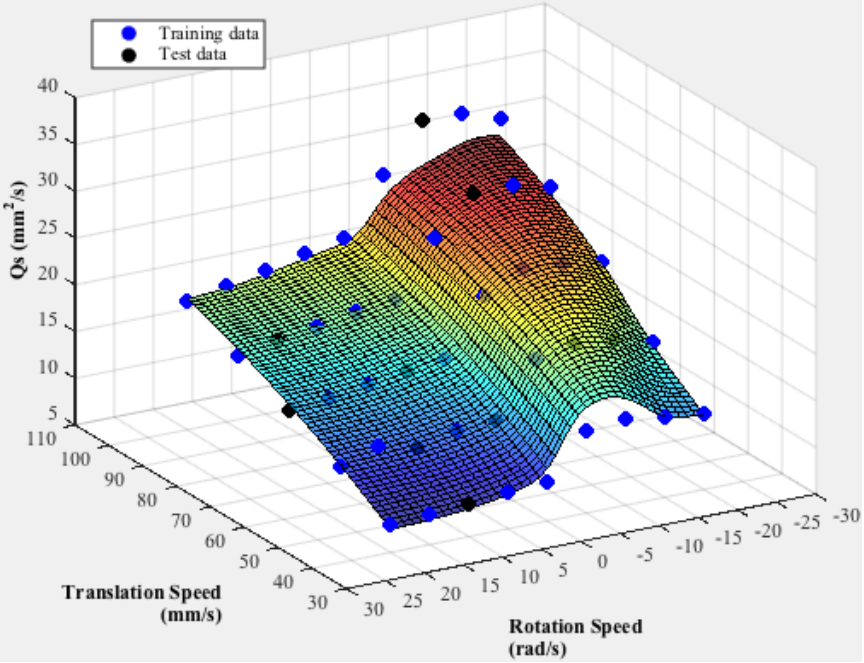

(a)

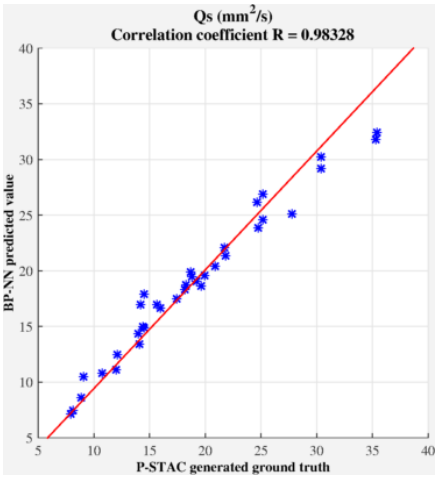

(b)

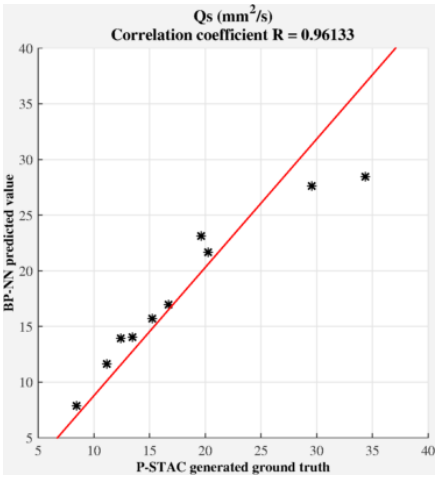

(c)

Figure 8.16: BP-NN regressed surface for Q_s for the case of spreading on substrate with $S_q = 79\mu$m

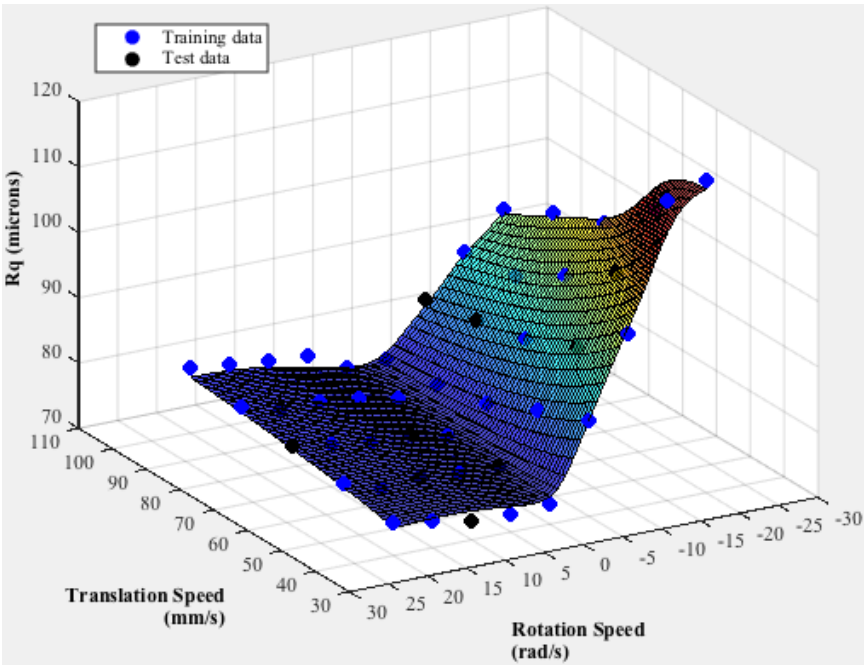

(a)

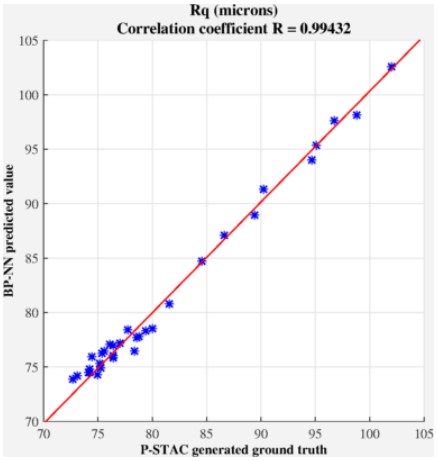

(b)

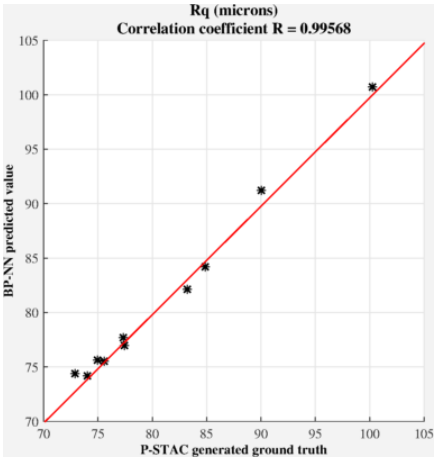

(c)

Figure 8.17: BP-NN regressed surface for R_q for the case of spreading on substrate with $S_q = 79\mu$m

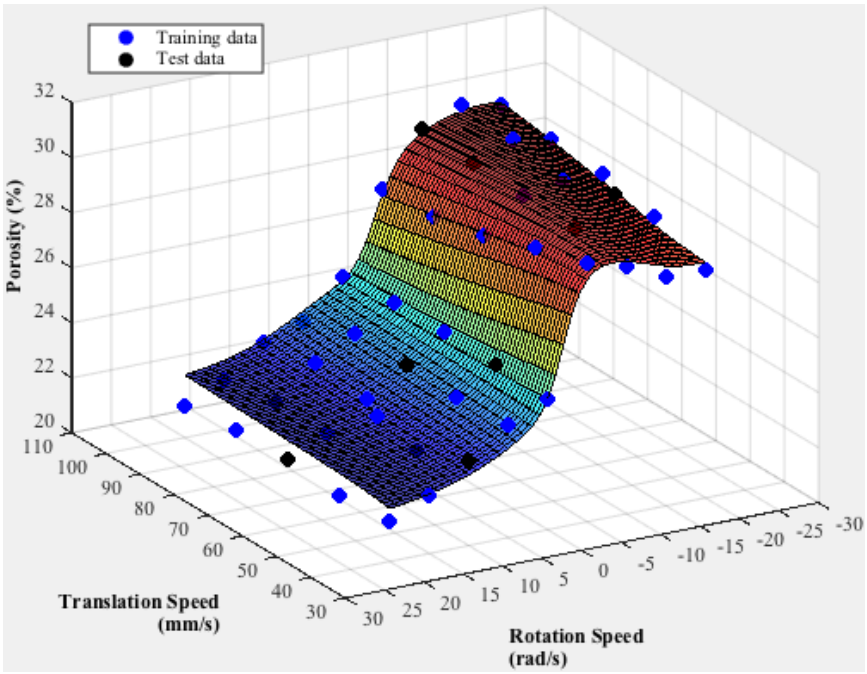

(a)

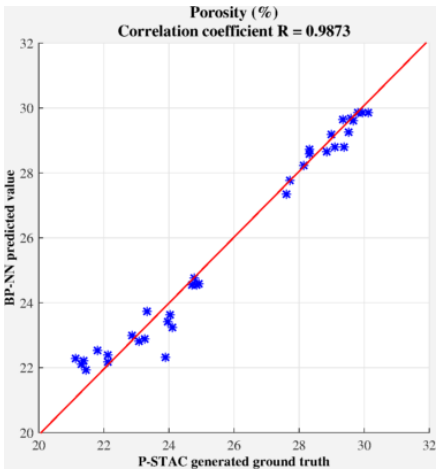

(b)

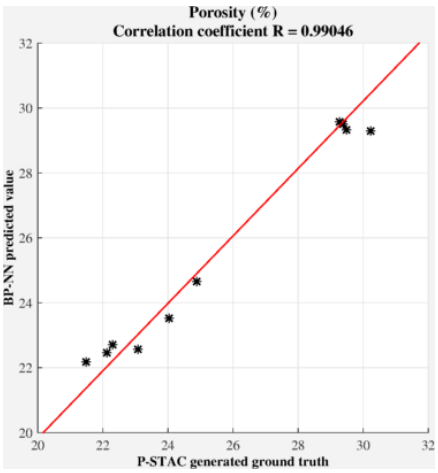

(c)

Figure 8.18: BP-NN regressed surface for Φ for the case of spreading on substrate with $S_q = 79\mu$m

are summarized in Table 8.2. Again, like in the case of spreading with no PSD (refer Chapter 7), spreading cases with no roller rotation and roller rotating in clockwise direction (i.e., opposite to the rotational motion shown in Figs. 8.8 and 8.9), resulted in deposition of 2-3 powder layers over a single pass of spreader as opposed to a single layer of particles with single pass of anticlockwise rotating roller. The physics-based simulation results, as seen in Figs. 8.15, 8.16, 8.17 and 8.18 (blue and black points), are highly non-linear and the simulation time, per spreading simulation, is quite high to perform a parametric study covering the entire range of spreader translation and rotation speeds, thereby resulting in a better understanding of the effect of these speeds on the spread layer properties M_s, Q_s, R_q and Φ. Similar to Section 7.4, Machine Learning enabled surrogate modeling can be employed to regress between these highly non-linear data points. A schematic of a Back Propagation Neural Network (BP-NN) with 2 inputs and 4 outputs, is shown in Fig. 8.14. Only single hidden layer was used in this study. The topology of BP-NN is the same as that described in Table 7.4. Regression results from the final BP-NN with parameters listed in Table 7.4 are shown in Figs. 8.15, 8.16, 8.17 and 8.18 for spreading simulations over a rough substrate ($S_q = 79\mu$m). The surfaces predicted by this BP-NN, refer sub-figure (a) of Figs. 8.15 through 8.18, nicely blanket the simulation data points, both training and test data points, generated via DoS. Also shown is the correlation coefficient R between P-STAC simulation results and BP-NN predicted results (b) and (c) sub-figures of Figs. 8.15 through 8.18. The near unity value of R for both training and test data points for each of the layer properties M_s, Q_s, R_q and Φ, suggests a near perfect regression. BP-NN trained for spreading of Ti-6Al-4V powder on 79μm substrate is able to predict results with at least 96% accuracy. Blanket plot for Q_s with PSD is similar to the one without PSD

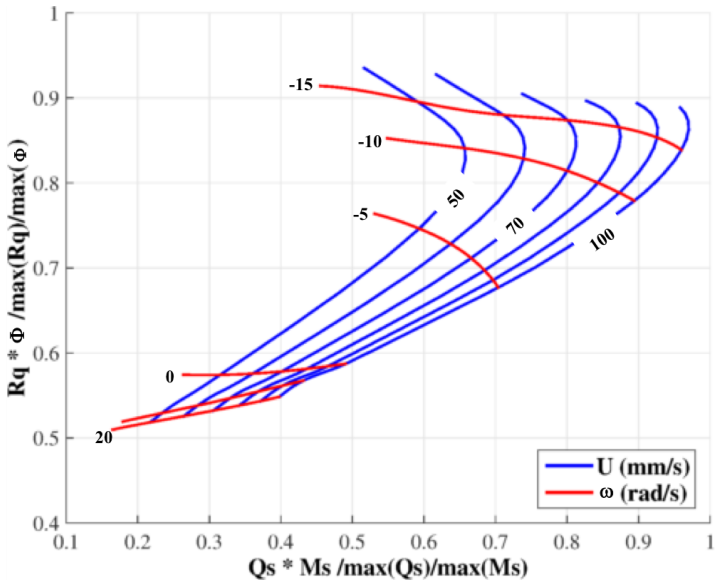

Figure 8.19: Spreading process map relating hybrid spread layer properties to the translation speed U and rotational speed ω of the spreader for polydispersed Ti-6Al-4V particulate media

(refer Fig. 7.13). However the trend of R_q blanket with PSD is much different when compared to the one without PSD (refer Fig. 7.14). Thus it is necessary to consider PSD when providing predictions related to AM powder spreading.

It is difficult to present the information shown in blankets plots of Figs. 8.15 through 8.18 on a single process map (as was done in Chapter 7) due to the higher dimensionality of this data. However a close examination of these blanket plots in Figs. 8.15 through 8.18, shows that clockwise roller rotations (negative ω values) result in a rougher and porous layer but provide a higher throughput. Smoother spread layer is obtained by having no rotational motion. Depending on the application of the part being 3D printed, it might be desirable to have least porosity or least roughness but always maximum spread throughput. Once a 3D printer operator knows the desired minimum porosity (or roughness) he/she can use these blanket

plots to determine the U-ω pair which has the maximum throughput.

But it is possible to present the information from the four layer properties on a single plot by creating hybrid properties like ((R_q normalized by the maximum (R_q)) * ((Φ normalized by maximum (Φ)) and ((Q_s normalized by the maximum (Q_s)) * ((M_s normalized by maximum (M_s)). Most of the applications will need minimum of the first hybrid property and maximum of the second hybrid property. A process map with these hybrid properties is shown in Fig. 8.19. For a given R_q, Φ pair, the rightmost point on the process map corresponds to the maximum throughput or print speed. A 3D printer operator can perform a spread at a U-ω pair and examine the roughness (R_q) and the porosity (Φ) of the layer and also find the corresponding U-ω point on the spreading process map. Now, if a lower porosity and roughness is desired then he/she can slide down along the blue contour corresponding to the U value. But by doing so, the throughput decreases. The operator can sustain the spread throughput by following a vertical line through the U-ω pair and move downwards. Thus he can determine the next U-ω pair at which he can conduct the spreading which will result in a smoother and denser layer while sustaining the throughput.

8.5 Conclusions

To conclude, a synergistic framework based on experiments and modeling, which comprised of physics-based modeling using DEM and ML enabled surrogate modeling using BP-NN, has been presented in this study to provide spreading predictions in powder-bed AM techniques. A novel, simple to use, multi-purpose retrofit to a commercial 3D printer, to experimentally study single layer spreading, is designed

and additively manufactured using plastic. This spreading retrofit is successfully used to study spreadability of an industrial grade Ti-6Al-4V powder having particle sizes in the range of 100μm and 250μm over additively manufactured spreading test coupon. The DEM modeling technique introduced in Chapters 6 and 7, is expanded to account for polydispersity and is successfully applied to generate a rheometry validated virtual avatar of the particulate media (viz. Ti-6Al-4V powder). This virtual avatar is further used to simulate the spreading of virtual Ti-6Al-4V powder, which is modeled as a collection of 235,000 smooth spherical and cohesionless particles. The spreading simulations with PSD compare better than the ones without PSD, to the experimental findings. This added modeling fidelity of polydispersity in the particulate media comes at the expense of higher computational costs. The spreading model is further used to extract other spread layer properties, which are difficult to be measured experimentally, like layer porosity, roughness and spread throughput. Back propagation neural network is used to regress between the highly non-linear spread layer properties as a function of spreader speeds.

Acknowledgements

Authors of this work would like to acknowledge the following contributions:

1. Dr. Sneha Narra from the research group of Prof. Beuth for the 3D printed Ti-6Al-4V coupon

2. Mr. Nicholas Wolf from the research group of Prof. Higgs for the 3D printed coupon holder in plastic

Part III

Application #2:

Sustainability of cutters used in energy resource rock drilling

Art is the lie that enables us to realize the truth.
-Pablo Picasso

Chapter 9

Introduction to rock drilling

In today's world where renewable energy sources are being tapped into for energy needs, much more than any of the preceding decades, fossil fuels still continue to contribute towards satisfying majority of the energy needs of the world [37]. Prices of oil have historically shown a mischievous trend [90] going as high as $156/barrel in 2008 and as low as $20/barrel in 1998 or the recent exponential drop to $30/barrel in 2016 (not adjusted for inflation). The factors for these price fluctuations can vary from supply-demand to OPEC behavior [91] and result in major changes in the world GDP [92].

As mentioned in Chapter 1, over the last many years, petroleum companies have been trying to find ways to efficiently drill through the rocks to reach the fossil fuel rich geologic formations. In the present day, with the steep fall in oil prices, it becomes all the more relevant to optimize this rock drilling process. The energy rich geologic formations are usually located deep inside the earth's crust (refer the schematic of a typical off-shore drill rig shown in Fig. 9.1) and drilling a hole to reach these formations consumes significant portion, as high as 50%, of the entire

crude oil extraction time [37]. The cost to rent the drilling rigs, a practice which is prevalent in the petroleum industry, is exorbitantly high (as high as $250,000 per day). Drilling action involves high impact between the drill bit and the rock formation and can result in the fracture of individual cutters which makeup the bit. If a significant number of cutters break mid-way to the drilling process, to reach the energy rich geologic formation, then the drill bit can no longer penetrate through the rock formation. This results in stalling of the drilling action and considerable time and money is lost in replacing the drill bit [37]. Thus, there is a need to optimize the drill bit's penetrating action which is controlled by the material composition of the bit, weight on the bit and revolutions per minute (rpms) of the bit, to drill to the energy rich geologic formation consuming the least amount of time. This optimization process is highly dependent on the rock formation which is being drilled into. These rock formations vary a lot based on geographical position of the oil well and even vary significantly with the depth at any given well location, as is indicated by rock core sampling data [38]. In other words, there is no single, 'strongest' drill bit that can work best anywhere on the earth. There is a need to understand the wear mechanism of both, rocks and cutters, and predict the lifetime of a cutter, in other words the sustainability of cutter.

The present drill bit research is focused around drilling muds, vertical turret lathe testing of cutters and bit-on-rock tribometry [4, 39–41]. While this is easy to perform, it is far from the real conditions seen by a drill bit which has a rotary action as opposed to the translation loading in a vertical turret lathe, very high weight on bit as opposed to bit-on-rock tribometry and occurs in a high temperature and high pressure subsurface environment.

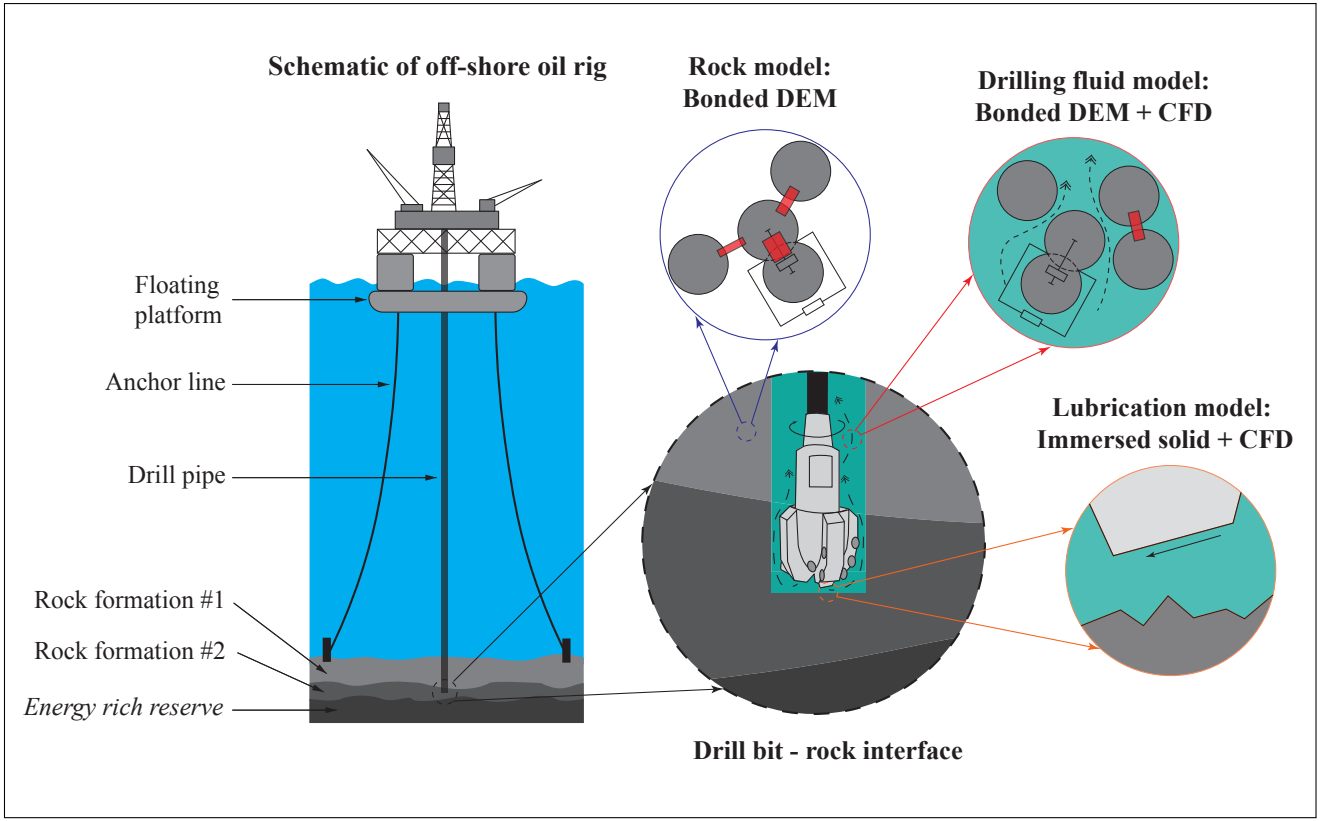

Figure 9.1: Multi-physics involved in the energy resource rock drilling

The wear of a bit caused directly by the rotary action should be considered in concert with the impacts of the drilled rock pieces as these are being carried out by the drilling fluids. This problem has a cutter-on-rock interface filled with drilling fluids and rock cuttings. This is a particle-fluid-structure interaction problem. This problem is rich in multi-physics covering tribological phenomena like three body wear and hydrodynamic lubrication, fracture mechanics of rocks and fluid mechanics and cooling efficiency of the drilling mud. This research tries to study the sustainability or the wear-based lifetime predictions of cutters used in drill bits using the triadic formulation introduced in the first chapter.

Referring to the terminology introduced in Section 1.3, Fig. 9.1 shows an exploded view of all the attributes of all the phenomena or physics of contact mechanics, particle mechanics and fluid mechanics which can be encountered while trying to understand the rock drilling capability of cutters.

A theory or model which accounts for all the attributes shown in the Fig. 9.1 does not exist in literature. The multiphysics of this tribosystem is analogous to the different tiles which made up the baby elephant of Fig. 1.3 and the inclusion or approximation of the attributes, shown in circles or bubbles in Fig. 9.1, is analogous to the clarity of the tiles making up the aforementioned baby elephant. The aim is to answer questions about the rate of penetration of the drill bit in a particular rock formation (question about guessing the animal name in Section 1.2.1) the lifetime of this drill bit (question about predicting the animal age in Section 1.2.1) in the least amount of time.

To this effect, a closed-loop, synergistic solution combining experiments and modeling is proposed in this thesis to understand the rate of penetration of a drill bit as a function of weight on bit and revolutions per minute (rpm) of the drill bit, in dry

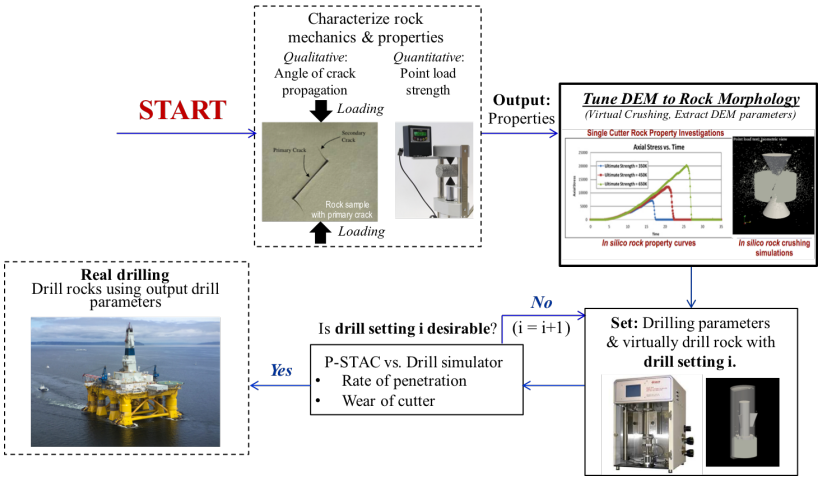

Figure 9.2: Process flow to study the *sustainability* of cutters used in rock drilling for energy purposes

and aqueous conditions. Figure 9.2 shows the process flow to study the *sustainability* of cutters used in rock drilling for energy purposes. A rock strength characterization test called point load strength test is described in Chapter 10. Also described in Chapter 10, is the way to model a cement-concrete like rock using bonded particle discrete element method and the approach based on finite differencing to model the fluid dynamics encountered in the aqueous drilling conditions. Finally, in Chapter 11, this framework is applied to study dry and aqueous drilling of sandstone. Here the model predictions are compared to the experimental findings from a benchtop drilling simulator for two types of sandstones: Castlegate sandstone from the energy rich state of Texas and Crab Orchard sandstone from Tennessee.

The heart of a man is very much like the sea, it has its storms, its tides and its depths; it has its pearls too.
-Vincent van Gogh

Chapter 10

Modeling rock mechanics and fluid mechanics

10.1 Introduction

Rock drilling for oil and gas has existed for ages but still continues to be a major research and development project. The primary goal of a drilling job, which accounts for almost half the cost of the entire oil extraction project [37], is to drill to the energy rich rock formation situated hundreds of miles inside the earth, as fast as possible.

Nomenclature

Symbol	Meaning
K	Stiffness of the spring in a spring-dashpot system
K_{bond}	Stiffness of the mathematical bond between particles
γ	Bond stiffness factor
β	Damping of dashpot in a spring-dashpot system
n, t	Subscripts: normal and tangential directions respectively
ε	Coefficient of restitution
pp, pv, pd	Subscripts: Collisions occurring between a particle (p) and another particle (p), cylindrical vessel (v) or drill bit (d) respectively
m	Particle mass
V	Particle speed
Δ	Overlap of a particle with another particle or geometry
ϕ	Diameter of a spherical particle
μ	Coefficient of sliding friction
σ_{bond}	Bond strength in newtons
$\underline{C}$	Position vector of the center of a spherical particle
$\underline{e_t}$	Unit vector along the tangential direction
λ	Bond strength factor
F	Force magnitude
I_s	Point load strength index
ρ	Fluid density
μ_f	Dynamics viscosity of fluid

It is difficult to predict the nature and manner of rock failure owing to the heterogeneous nature of rock. This in turn, causes difficulty in predicting exact geometry of the rock-cutter interface while the dill bit penetrates through the rock. A typical PDC drill bit (refer Fig. 9.1) is made up of a number of immovable cutters made of PDC (Polycrystalline Diamond Compact) having many variables like cutter orientation, rake angle, cutting edge material and cutting edge bevel [2, 40]. Studies trying to understand the wear of PDC cutters can be broadly divide into two schools of thought: vertical turret lathe (VTL) like testing or bit-on-rock tribometry testing [39–42]. VTL like testing involves translation loading of the cutter which is much different form the rotational motion of a real drill bit. Bit-on-rock tribometry

occurs at loadings and temperatures much smaller than the ones encountered in the real drilling. The wear of a bit caused directly by the rotary action should be considered in concert with the impacts of the drilled rock pieces as these are being carried out by the drilling fluids. With this regard, the present chapter presents a multi-physics framework which can be used to simulate a benchtop drilling simulator which performs drilling into real rock cores at realistic drilling conditions, and provide engineering predictions about drilling into rocks. The tribosystem of interest involves mechanics of interacting and contacting solids (drill bit and parent rock), mechanics of the particulate media (rock cuttings) and mechanics of the drilling fluid. Wear of rock is as much important to understand as is the wear of the cutters. This chapter presents a framework to generate virtual concrete-like rocks made up of 265,000 bonded DEM particles (500μm in size) to mimic sandstones in Section 10.2. Then Section 10.3 presents and validates a fluid rigid (i.e., non-deformable) structure interaction model using a CFD approach based on finite differencing, immersed boundary method (IBM) and Newtonian fluids, subsequently to be used to simulate aqueous drilling fluids.

10.2 Computational Rock Mechanics

10.2.1 Bonded Particle DEM model for concrete-like rocks

Bonded particle model making use of parallel bonds has been proposed by Cundall and Potyondy [53] and used by many researchers [4]. This model captures the heterogeneity of rocks by forming mathematical bonds, parallel or point, between overlapping particles. This model, though shown to have given good results in predicting rock mechanics, does not allow boding between particles or rock grains which do not overlap but are in the vicinity of each other. Such types of bonds which are more intuitive and realistic (like cement paste biding aggregates in concrete) in naturally occurring sandstones have been employed in the current study.

Cement paste like mathematical bonds are formed between uniform sized spherical, uncrushable particles. These bonds have a stiffness, referred to as K_{bond}, which is chosen to be a fraction of K_n (Eq. 1). Here is γ is referred to as bond stiffness factor.

$$K_{bond} = \gamma K_n \tag{10.1}$$

where,

$$K_n = \frac{f^2 m_{eq} V_{max}^2}{\phi^2}; f = \frac{\phi}{\Delta_{max}} \tag{10.2}$$

Here m_{eq} stands for the equivalent mass of colliding particles, having diameter ϕ and constant coefficient of restitution ε which is independent of impact velocity [18, 22]. This m_{eq} is one half of the harmonic mean of the individual masses. V_{max}

and Δ_{max} are the estimated maximum speed and inter-particle penetration for the simulation at hand. These values are usually guessed.

The bonds have strengths $\sigma_{bond,ij}$ which decay as the distance between particles increases:

$$\sigma_{bond,ij} = \frac{\phi}{||\underline{C_i} - \underline{C_j}||}\sigma_{bond,max} \tag{10.3}$$

Where $\underline{C_i}$ and $\underline{C_j}$ are the position vectors of the centers of particles i and j respectively and $\sigma_{bond,max}$ is the absolute maximum bond strength. This absolute maximum bond strength is defined as the maximum force which the bond can resist before breaking:

$$\sigma_{bond,max} = \lambda K_{bond}\Delta_{max} \tag{10.4}$$

Here λ is referred to as the bond strength factor. A slider is also present in the shear direction. It limits the maximum frictional force in this direction, the value of which is equal to the product of sliding friction coefficient and normal reaction force $\underline{F_n}$ (given by Eq. 10.7). It is assumed that all the interactions cause particles to slide thereby nullifying the tangential damped Hookean spring. In other words, only the slider acts in the shear direction. Therefore, the forces along the normal ($\underline{F_n}$) and tangential ($\underline{F_t}$) directions experienced by a colliding particle with an overlap of Δ with other particles or geometries, relative approach speed of $\dot{\Delta}$ and unit vector $\underline{e_t}$ in shear direction as can be represented as:

$$\underline{F_n} = \begin{cases} K_n\underline{\Delta_n} - \beta_n\underline{\dot{\Delta}_n} + K_{bond}\underline{\Delta_{bond,n}}, & \text{if } K_{bond}|\underline{\Delta_{bond}}| < \sigma_{bond} \text{ (intact bond).} \\ K_n\underline{\Delta_n} - \beta_n\underline{\dot{\Delta}_n}, & \text{for (broken bond).} \end{cases} \tag{10.5}$$

$$\underline{F_t} = \begin{cases} -\mu|\underline{F_n}|\underline{e_t} + K_{bond}\underline{\Delta_{bond,t}}, & \text{if } K_{bond}|\underline{\Delta_{bond}}| < \sigma_{bond} \text{ (intact bond).} \\ -\mu|\underline{F_n}|\underline{e_t}, & \text{for (broken bond).} \end{cases} \tag{10.6}$$

The damping coefficient for the DEM particles is given by (similar to Part II):

$$\beta_n = -2\ln(\varepsilon)\Big[\frac{K_n m_{eq}}{\pi^2 + \ln(\varepsilon)^2}\Big]^{\frac{1}{2}} \tag{10.7}$$

Rolling and twisting motion of the particles has been ignored

Around 265,000 particles initialized at an hcp lattice are allowed to settle under gravity in a cylindrical vessel using the DEM approach described in Part II. Then these are bonded as follows:

1. Form a neighborhood for every particle i (refer Part II for details)

2. Particle i will be bonded with every particle j in its neighborhood with a mathematical bond whose strength (in terms of force) is given by $\sigma_{bond,ij}$

A calibration process can be designed to iteratively change V_{max}, γ and λ to find the correct point load strength for the rock of interest. Concrete-like bonded DEM makes use of the Particle Tessellated Surface Interaction Scheme introduced in Part II to account for particle-structure interactions. This capability is added to the computational particle dynamics (CPD) module of the in-house multi-purpose, multiphysics software Particle-Surface Tribology Analysis Code (P-STAC) developed by the author and prior PhD and MS students of Prof. C. Fred Higgs III.

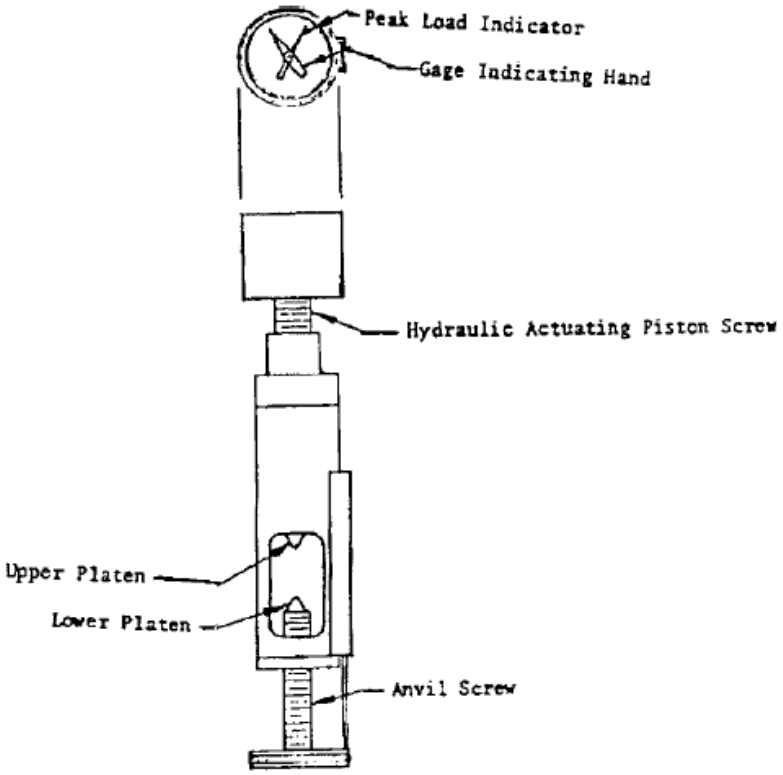

Figure 10.1: Point load strength test apparatus, reproduced from ASTM standard D 5731 - 16 [93]

10.2.2 Point load strength test

One of the simplest and most versatile test to characterize rock strength is the point load strength test pioneered by Broch (1972) [45] and described in ASTM D 5731-16 [93]. This test is referred to as an index test as the compressive strength of the rock specimen (which can have any shape) is not directly measured from this test but what is measured is an index to which the compressive strength is proportional

to. This index, denoted by I_s is given by:

$$I_s = \frac{P}{D^2} \tag{10.8}$$

where P is the load at which the rock sample, held in-between conical platens shown in Fig. 10.1, fails or ruptures and D is the distance between the platens. The compressive strength of rock (σ_c) is then given by:

$$\sigma_c = kI_s \tag{10.9}$$

here k is a factor in between 17.5 and 24.5 which depends on the size of the rock sample, the manner of loading (diametral or axial) and the shape of the rock sample (cylindrical core or spherical lump). This test is an experimental equivalent of the domain size independence study conducted in this thesis in Chapter 6 to obtain the smallest feasible rock sample size which can provide dependable and reproducible strength values. Thus, this test also is best suited for calibrating a virtual avatar of the real rock, as the virtual rock can have computationally manageable DEM entities.

10.2.3 Virtual point load strength test: Axial loading

The two cones, having geometries as defined in the ASTM standard [93], are used to apply point axial loads on the top and bottom faces of the cylindrical rock core using displacement control (0.2mm/s). The diameter of the virtual rock core is 36mm and the height is 23mm. Based on the ASTM standard, a sandstone like Castlegate having an unconfined compressive strength of 12 MPa should fail at a point load P of about 250N (assuming k to be 25). Note: This standard applies to

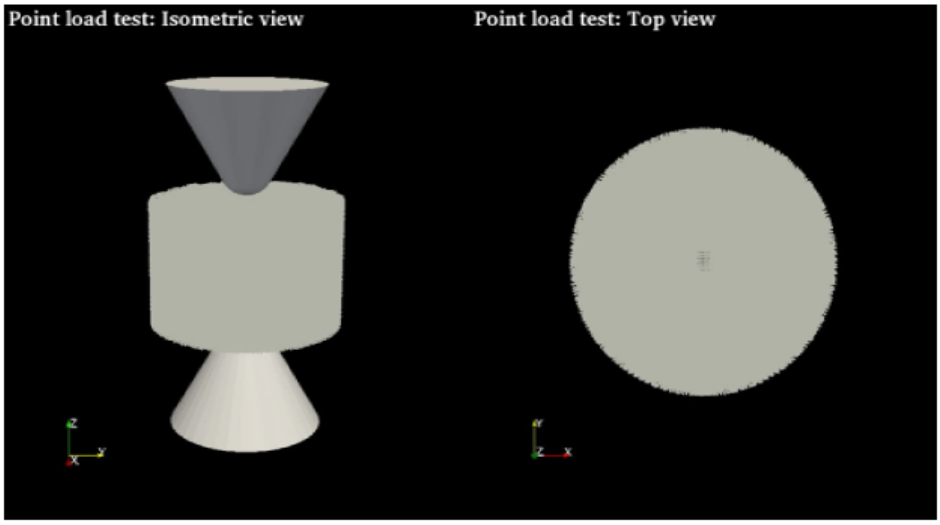

(a) Start time

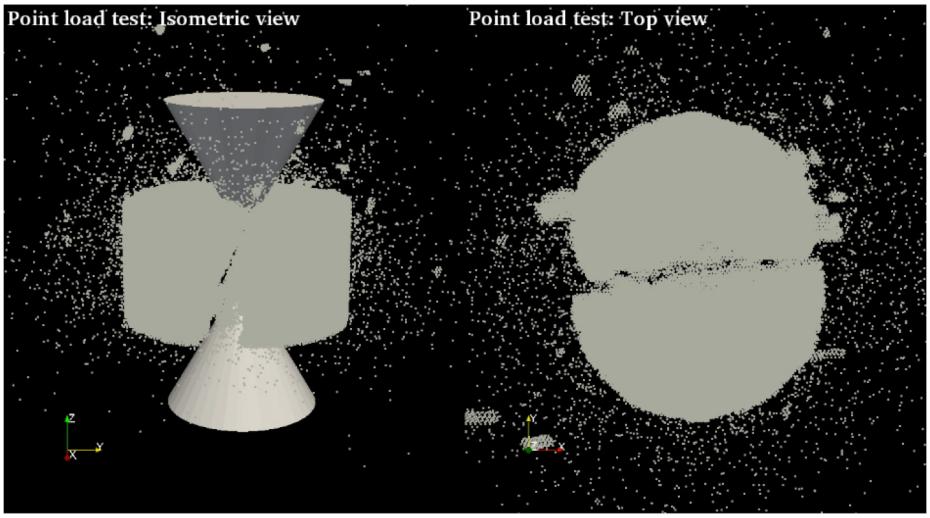

(b) End time

Figure 10.2: Simulation snapshots for point load strength test with concrete-like rock comprised of 265,000 spherical grains with a grain size of 500μm

rocks having compressive strength 15MPa or more but the authors feel that point load test is the only strength characterization test best suited for weaker rocks.

(a) Valid failure (b) Invalid failure

Figure 10.3: Rock sample failures in a point load test [93]

Table 10.1: Contact interaction parameters used in DEM rock drilling simulations

Parameter	Value
Density of grains (kgm-3)	2650
Grain diameter (μm)	500
μ_{pp}	0.3
μ_{pv}	0.9
μ_{pd}	0.3
ε	0.8
λ	20
γ	0.8

Typical simulation start and end snapshots are shown in Fig. 10.2. The concrete-like rock can be seen to be failing by developing a fault plane which intersects both the top and bottom faces of the rock. This is type of failure desired and described as a valid failure in ASTM standard D 5731 - 16 for this test (refer Fig. 10.3). The rock failure occurred at a much lesser load of about 2N (i.e. a compressive strength of 95kPa) for the DEM parameters given in Table 10.1

Trying to increase the failure load means trying to increase the values of V_{max} and λ, this results in a smaller time step and longer simulation time. This virtual avatar, though not a naturally occurring rock, can still be thought of a very weak concrete-like rock, which qualitatively fails like real rocks and can be made available to study drilling in rocks.

10.3 Computational Fluid Mechanics

In this thesis, fluid mechanics is numerically modeled using Eulerian principles which assume the fluid to be a continuum. Following momentum 10.10 conservation and mass conservation 10.11 equations are solved using finite differencing technique:

$$\rho\left(\frac{\partial V_x}{\partial t}+V_x\frac{\partial V_x}{\partial x}+V_y\frac{\partial V_x}{\partial y}+V_z\frac{\partial V_x}{\partial z}\right)=-\frac{\partial p}{\partial x}+\mu_f\left(\frac{\partial^2 V_x}{\partial x^2}+\frac{\partial^2 V_x}{\partial y^2}+\frac{\partial^2 V_x}{\partial z^2}\right)+\rho f_x \tag{10.10a}$$

$$\rho\left(\frac{\partial V_y}{\partial t}+V_x\frac{\partial V_y}{\partial x}+V_y\frac{\partial V_y}{\partial y}+V_z\frac{\partial V_y}{\partial z}\right)=-\frac{\partial p}{\partial y}+\mu_f\left(\frac{\partial^2 V_y}{\partial x^2}+\frac{\partial^2 V_y}{\partial y^2}+\frac{\partial^2 V_y}{\partial z^2}\right)+\rho f_y \tag{10.10b}$$

$$\rho\left(\frac{\partial V_z}{\partial t}+V_x\frac{\partial V_z}{\partial x}+V_y\frac{\partial V_z}{\partial y}+V_z\frac{\partial V_z}{\partial z}\right)=-\frac{\partial p}{\partial z}+\mu_f\left(\frac{\partial^2 V_z}{\partial x^2}+\frac{\partial^2 V_z}{\partial y^2}+\frac{\partial^2 V_z}{\partial z^2}\right)+\rho f_z \tag{10.10c}$$

$$\frac{\partial V_x}{\partial x}+\frac{\partial V_y}{\partial y}+\frac{\partial V_z}{\partial z}=0 \tag{10.11}$$

Numerical solution to the above 3D, time-dependent, Navier-Stokes equations based on Chorin's projection method and staggered grid, is obtained using the techniques elaborated by Griebel [60]. Fluid entrapment in a tribosurface with sliding surfaces and converging gap results in pressure increase [94]. While trying to solve the fluid mechanics at the length scale of a tribosurface, the size of mesh can be

in microns and the length scale of the entire problem can be in cm's. This necessitates a local mesh refinement to save on computational costs by not having to simulate the entire CFD domain with highly refined mesh elements. An implementation of a non-uniform mesh or a locally refined mesh, referred to from hereon as a graded mesh, mandates the changes in the discretization schemes elaborated by Griebel for uniform mesh. In the current study, discretization schemes chalked out by Rojas [95], are used to account for a graded mesh like the ones shown in Figs. 10.4c and 10.7b. Immersed Boundary Method (IBM), introduced by Peskin [96] and described by Mpagazehe [4], is used to account for fluid-solid interaction. In this method, the presence of solid inside the fluid is accounted by applying pseudo body force in the implementation of the Navier-Stokes equation. The advantages of IBM include the use of structured mesh which need not be body-fitted to the surface of the solid. Two numerical studies have been carried out:

1. Air flow past stationary circular cylinder at low Reynolds numbers
2. Hydrodynamic lubrication in fluid film bearing

The aim of the first study is to shown the accuracy and computational efficiency of a CFD solver based on finite difference method of discretization, having structured-and-graded mesh, and employing IBM to account for immersed solids when compared to a CFD solver based on finite volume method of discretization and body-fitted mesh. While the aim of the second study is to show the need to solve the entire 3D Navier-Stokes equations even for the problems involving lubrication (as in the case of drill bit interacting with rocks in the presence of drilling fluid) instead of the lubrication approximation to the Navier-Stokes equation (also known as the Reynolds equation).

This CFD solver based on finite difference discretization, IBM and graded mesh forms the CFD module of the in-house multi-purpose, multiphysics software Particle-Surface Tribology Analysis Code (P-STAC) developed by the author and prior PhD and MS students of Prof. C. Fred Higgs III.

10.3.1 Air flow past stationary circular cylinder

Flow past a stationary circular cylinder has been studied for many decades. Even today the simplicity of the problem setup, both experimentally and computationally, makes it a natural choice for a touchstone problem to validate and verify in-house software like P-STAC. Even though the setup is simple, the physics represented by this problem is quite complex and still remains a major research topic. The graded mesh, which is refined in an exponential manner near the boundary of the circular cylinder, and the OpenFOAM mesh are shown in Fig. 10.4. The boundary conditions used in this study are shown in Fig. 10.4a. The immersed cylinder is accounted for by IBM in P-STAC and by a body-fitted mesh in OpenFOAM.

Unlike a flow past an obstacle having sharp corners, flow past a circular cylinder does not have pre-determined flow separation points. Also, the Reynolds number (Re, which is the ratio of fluid inertial to viscous forces) dependent dynamics of Karman vortex street (as seen in Fig. 10.5) adds to the complexity of this problem. If an in-house code (like P-STAC) can correctly predict the quantitative results for this problem then it increases the confidence in the fidelity of that software or code.

Time period of vortex shedding is plotted in Fig. 10.6a. Vortices are shed faster as the Re increases. P-STAC results are in good agreement with OpenFOAM and other published numerical and experimental findings [97–100]. Separation bubble length is defined as the distance from the base of cylinder (diametrically opposite

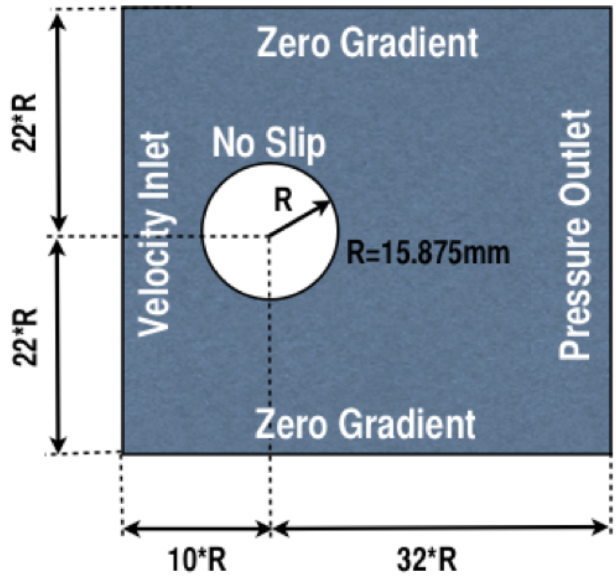

(a) BCs

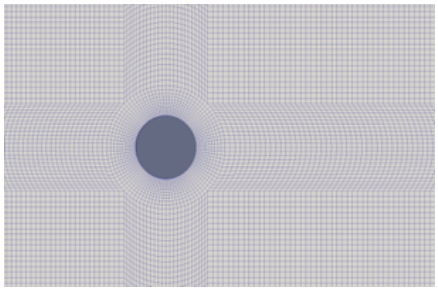

(b) OpenFOAM body-fitted mesh with 70,000 FV elements

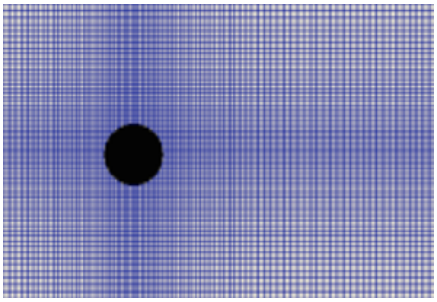

(c) P-STAC mesh with only 23,000 FD elements

Figure 10.4: CFD study of air flow past a stationary circular cylinder

to the flow stagnation point) to the point where the time-averaged (beyond the initiation of vortex shedding) velocity magnitude is zero (refer the schematic in the inset of Fig. 10.6b). The time averaging is carried out after the initiation of vortex shedding. The results are plotted in Fig. 10.6b. The results predicted by P-STAC are in good agreement with those predicted by OpenFOAM, the computational results

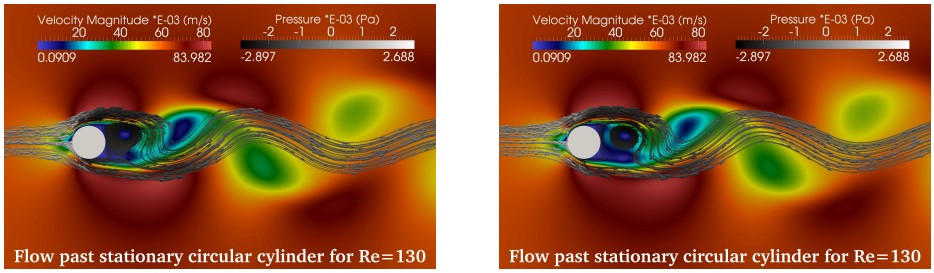

(a) Time1 (b) Time2

Figure 10.5: P-STAC simulation snapshots showing the Karman vortex street formed behind the cylinder

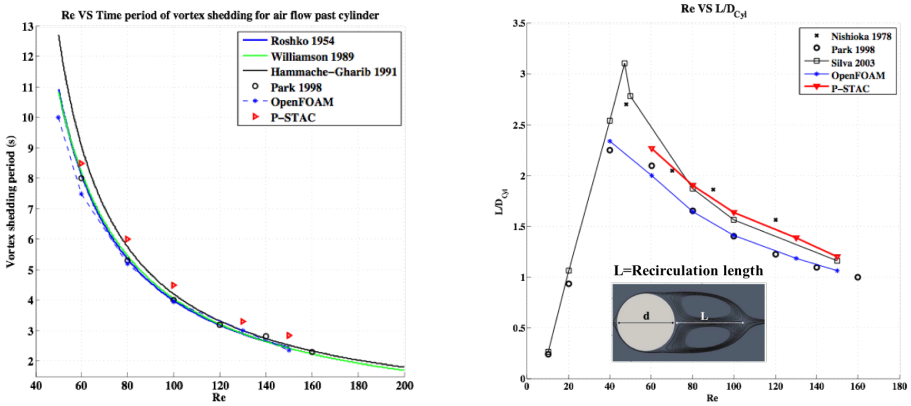

(a) Time period of vortex shedding (b) Length of separation bubble

Figure 10.6: CFD study of air flow past a stationary circular cylinder

by Park (1998) [100] and Silva (2003) [101] and experimental findings by Nishioka (1978) [102].

10.3.2 Hydrodynamic lubrication with SAE 0W-40 oil

Traditionally, Reynolds lubrication equation has been used to study the fluid mechanics in tribosurfaces. Reynolds equation is an approximation of the Navier-Stokes equations where inertial forces are assumed to be negligible (for low Re cases)

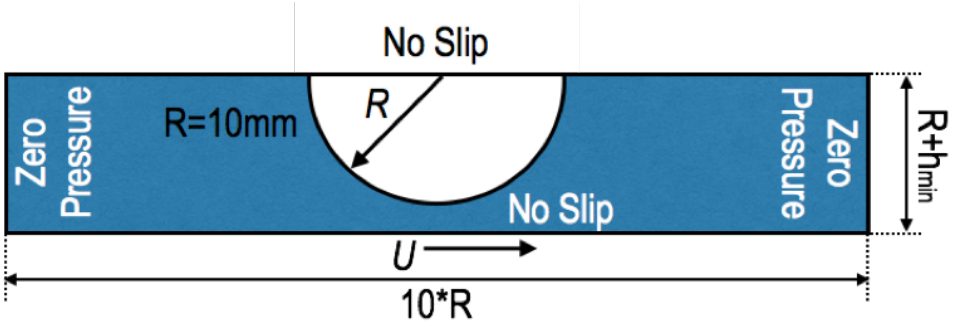

(a) BCs

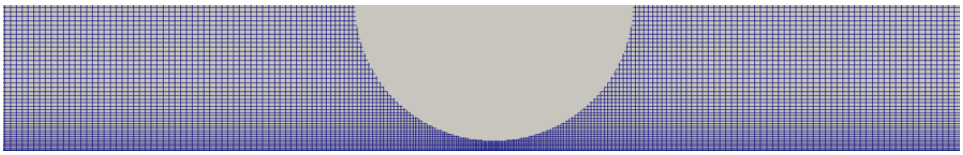

(b) Graded mesh

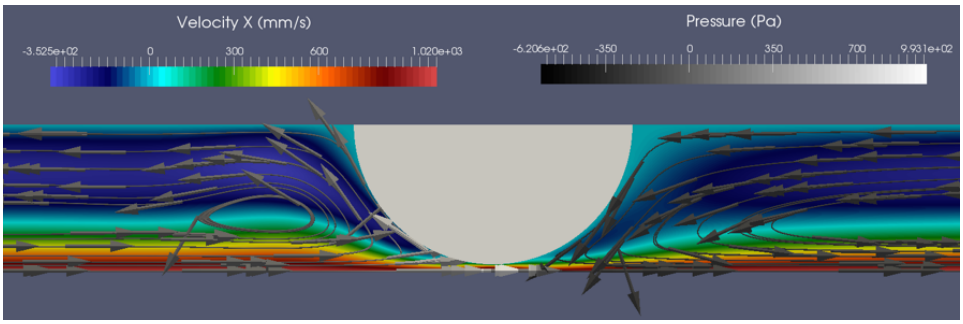

(c) P-STAC simulation snapshot

Figure 10.7: CFD study of hydrodynamic lubrication in a fluid film bearing

and is useful as it is computationally must faster than a full CFD analysis. However, for the problem of drilling into rocks, the Re is high and the inertial terms of the Navier-Stokes equations must be considered. To show the dependence of the pressure generated in sliding contact with a converging gap, on increasing sliding speeds, a typical fluid film bearing is modeled as a flat surface with a semicircular bump (top surface in Fig. 10.7a) [4]. The boundary conditions (BCs) are shown in Fig. 10.7a and the graded mesh is shown in Fig. 10.7b. A simulation snapshot

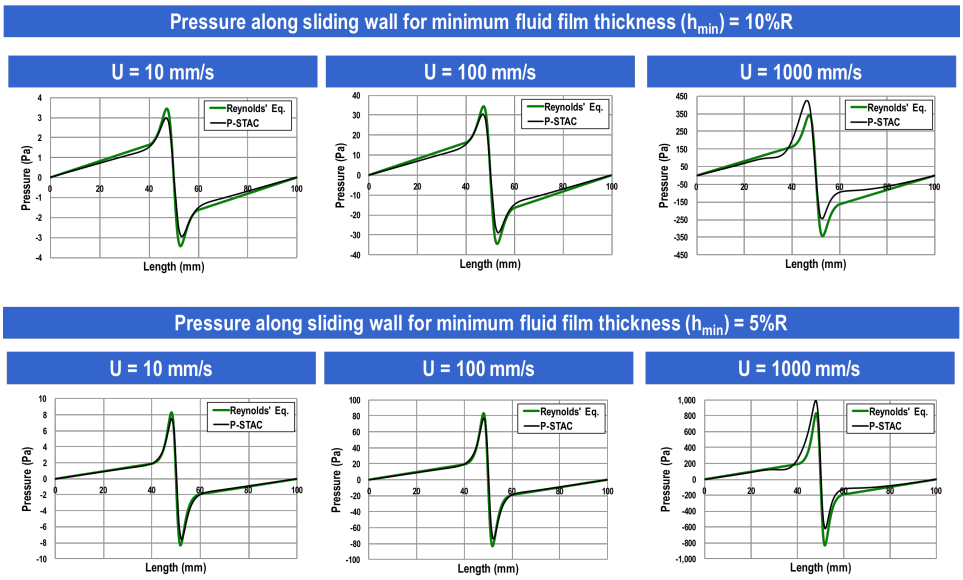

Figure 10.8: Pressure along the bottom sliding wall as a function of fluid film thickness and wall speed

obtained using P-STAC is shown in Fig. 10.7c.

Whenever fluid gets dragged in a converging gap, as in the case of the typical fluid film bearing in Fig. 10.7, a high-pressure zone is developed in the converging gap of the fluid film. This pressure results in the separation of the tribosurfaces. The pressure predicted by P-STAC is compared to the one predicted by Reynolds equation for two film thicknesses and varying speeds of the sliding wall in Fig. 10.8. As the film thickness decreases, the pressure generated in the tribosystem increases. This trend is predicted by both P-STAC and Reynolds equation (which is the simplification of CFD in P-STAC). However, as the speed of sliding wall increases, Reynolds equation under predicts the increase in pressure. At high speeds, often encountered in rock drilling, inertial terms which are neglected in Reynolds equation become important. Hence it is necessary to solve full CFD to predict the

response of drilling fluid in the problem of energy resource rock drilling.

The CFD model introduced in this chapter can be used only for Newtonian fluids. Cavitation phenomenon has not been accounted for so negative pressures, if any in sliding contacts, must be neglected while trying to find the pressure force exerted on the tribosurface because of the presence of fluids.

10.4 Conclusions

A computational weak concrete-like rock has been generated using the concrete-like bonded particle DEM model and tested for point load strength. Larger strengths of sedimentary rocks (which can be modeled as concrete-like rocks) found in nature, mandate extremely high values for the spring stiffness and bond strength of their virtual avatars. This subsequently results in a very low time step and makes the computations which involve 100's of thousands of sub-500μm particles, highly expensive. It is shown how to obtain a low-strength concrete-like rock which can be further used to provide drilling predictions.

CFD based on Newtonian principles and finite differencing in concert with immersed boundary method (IBM) provides promising results when compared to commercial software and experiments involving Newtonian fluids. Use of graded mesh, a form of non-uniform mesh, for local refinement in the regions of interest (regions having vortices or tribosurface interactions) greatly accelerates a CFD simulation. This fluid model can be further made available to predict behavior of water-based or aqueous drilling fluids while studying sustainability of cutters used in energy resource rock drilling.

Acknowledgements

Authors of this work would like to acknowledge the following contributions:

1. Dr. Anirban Jana for his guidance on OpenFOAM simulations

2. Late Dr. Jeremiah Mpagazehe for his guidance on P-STAC simulations

Good management consists in showing average people how to do the work of superior people.
-John D. Rockefeller

Chapter 11

Drilling into sandstone: Experiments and Modeling

11.1 Introduction

Energy resource rock drilling industries typically base the design and lifetime criteria of drill bits on the performance of individual PDC cutters (forming such a PDC drill bit) exposed to a vertical turret lathe (VTL) like testing. This chapter presents a study on a benchtop drilling simulator (shown in Fig. 11.1) which better simulates real life drilling, than a VTL, by making use of real rock cores and a miniaturized drill bit (see Fig. 11.1). While the drilling simulator can perform drilling under high pressure and high temperature conditions with real drilling muds, the scope of the present study was restricted to performing drilling experiments under atmospheric pressure and room temperature conditions using water as a drilling fluid. This chapter also presents the predictions given by employing the CFD-CPD approach described in previous chapters and named in entirety as the

Figure 11.1: Benchtop drilling simulator (left), miniaturized drill bit (center), stl file of the drill bit to be used in simulations (right)

Particle-Surface Tribology Code (P-STAC). Section 11.2 presents experimental and modeling studies related to drilling into Castlegate sandstone cores (from the energy rich state of Texas) in dry conditions. Section 11.3 presents experimental and modeling studies related to drilling into Crab Orchard sandstone cores (from Tennessee) in dry and aqueous conditions.

11.2 Drilling into Castlegate sandstone: Dry conditions

11.2.1 Experiments

A sample Castlegate sandstone core (1.5 inch in diameter and 1 inch tall) is shown in Fig. 11.2. Three drilling tests were conducted on such cores using the drilling simulator shown in Fig. 11.1. The first two tests involved a weight on bit (WoB) of about 275N and the drill bit rotated at 300rpm while the last test was performed at a lower WoB of about 137.5N. The purpose of the first two tests (which was the same test conducted twice) was to check the repeatability of drilling behavior on this benchtop drilling simulator while the last one was conducted to check the effect

(a) Pre-drill (b) Post-drill

Figure 11.2: Typical core of the Castlegate sandstone

of WoB on the drilling rate or rate of penetration (RoP). The drilled core samples looked similar to the one shown in Fig. 11.2. The drill depth as a function of time for these three experimental runs is shown in Fig. 11.3. The data for the first two tests is almost identical indicating the reproducibility of data using this benchtop drilling simulator. Also it can be seen from the curves of Fig. 11.3 that as the WoB decreases by 50%, the time required to drill to the same depth increases by about 50%. Slope of the drill depth vs. drill time curve gives the rate of penetration (RoP). As the WoB decreased, the drilling behavior also changed from being a smooth drilling action (indicated by the smooth yellow and orange curves in Fig 11.3) to a more irratic action (indicated by the jagged black curve in Fig 11.3), representing bit bounce in real drilling conditions.

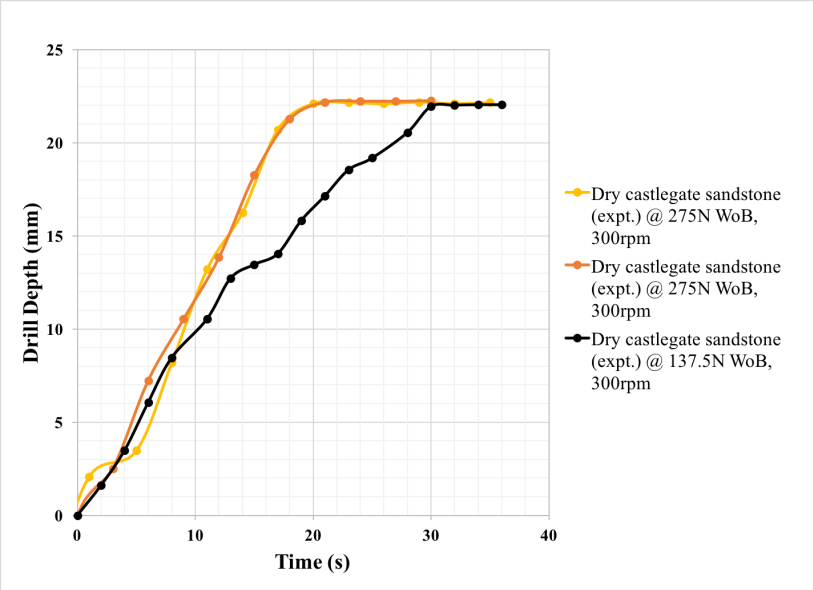

Figure 11.3: Real experimental drilling into Castlegate sandstone: Dry conditions

11.2.2 Modeling

P-STAC simulations were carried out on the weak concrete-like rock at much lower WoB of 2N and 1N. Typical simulation snapshots are shown in Fig. 11.4. Drill depth as a function of time for the P-STAC simulations is shown in Fig. 11.5. It takes longer time to drill as the WoB decreases. This finding is in agreement with the experimental results which are shown in Fig. 11.3 (also reproduced in the inset of Fig. 11.5).

11.3 Drilling into Crab Orcahrd sandstone: Dry and Wet or Lubricated conditions

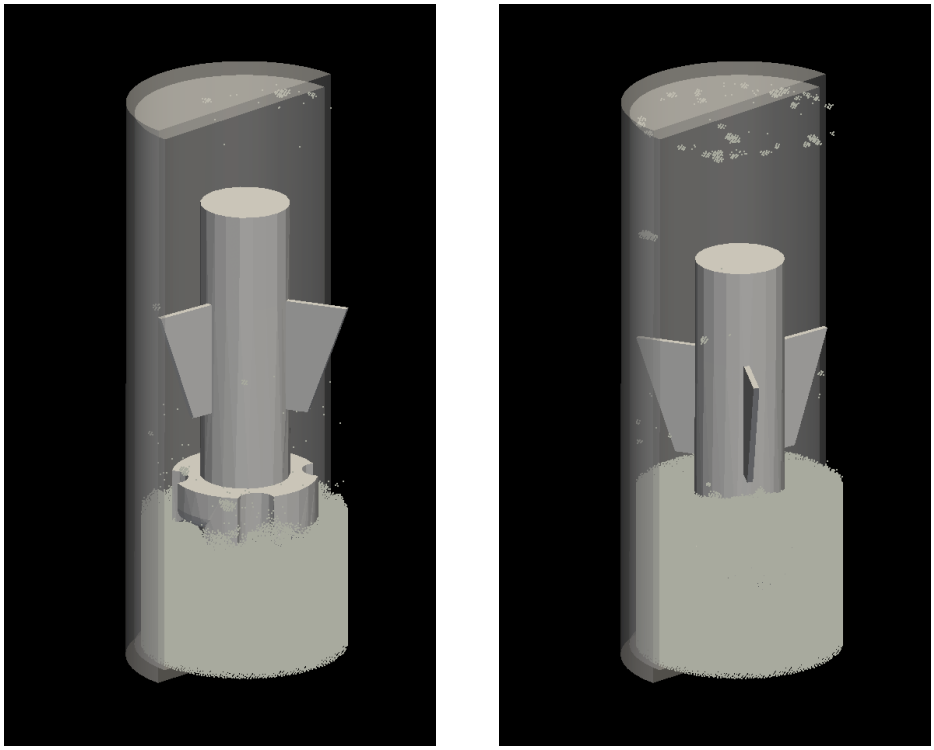

(a) Time1 (b) Time2

Figure 11.4: Simulation snapshots of drilling into concrete-like virtual rock in dry conditions

11.3.1 Experiments

Two drilling tests were conducted on Crab Orchard sandstone: one under dry conditions and the other under wet conditions with water as the drilling fluid. For the wet case, the rock core was soaked in water for 24 hours prior to the test [41]. All the other drilling parameters like WoB and rpms of the drill bit were kept constant for the two tests. Since this sandstone is much stronger than the Castlegate sandstone, the WoB was kept relatively higher at 695N. The drill depth vs. drill time curves are as shown in Fig. 11.6. For the wet case, the drill bit took significantly

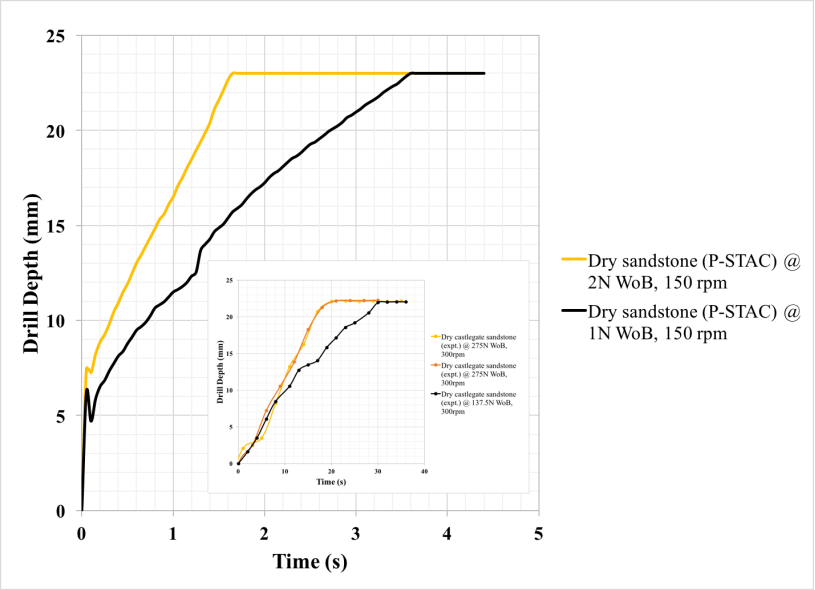

Figure 11.5: Virtual drilling into weak concrete-like rock: Dry conditions

longer time to penetrate to the same depth as compared to the dry case. The sudden jump towards the end of these curves might be due to the failure of the rock samples. It might be useful to investigate drilling in these sandstone cores at a lower WoB.

11.3.2 Modeling

P-STAC simulations were carried out on the weak concrete-like rock at much lower WoB of 0.5N under dry and wet conditions. A standalone CFD simulation was carried out to figure out the hydrodynamic pressure generated against a flat surface separated by a fluid film of the size of a single sandstone grain (500μm). The graded mesh used for this CFD simulation is shown in Fig. 11.7. The positive pressure generated on the bottom flat surface (Fig. 11.8a) is integrated over the flat area to find the upward force acting on the drill bit. This force is subtracted from the total WoB and a full-scale DEM-CFD simulation is carried out as shown in (Fig. 11.8b).

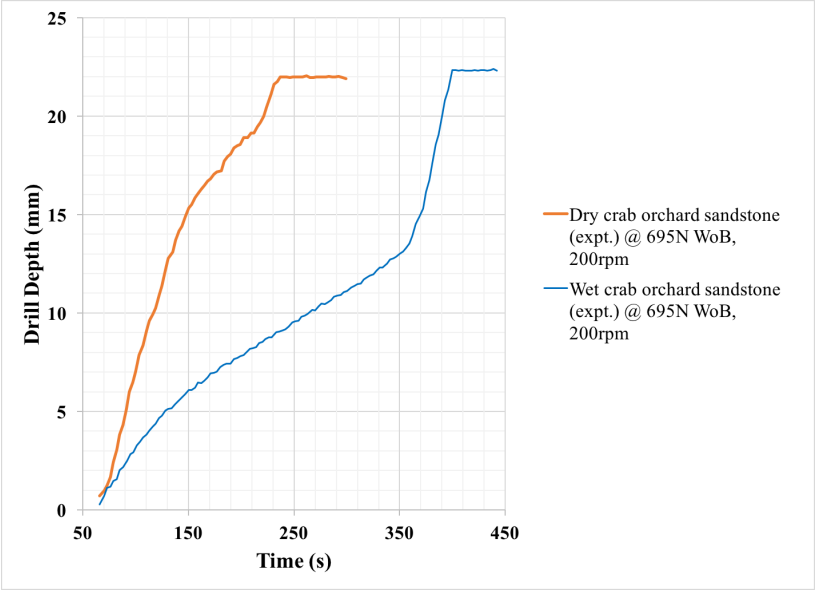

Figure 11.6: Real experimental drilling into Crab Orchard sandstone: Dry and wet or lubricated conditions

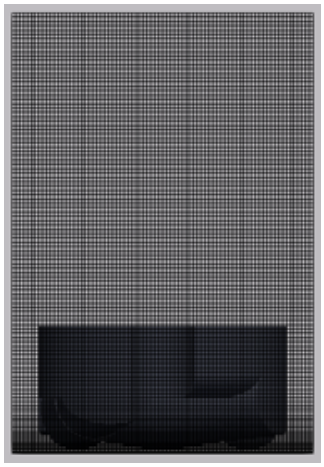

Figure 11.7: Graded mesh used in CFD

The streamlines resulting from the drill bit fluid interaction are shown as black curves in Fig. 11.8b. Drill depth as a function of time for the P-STAC simulations

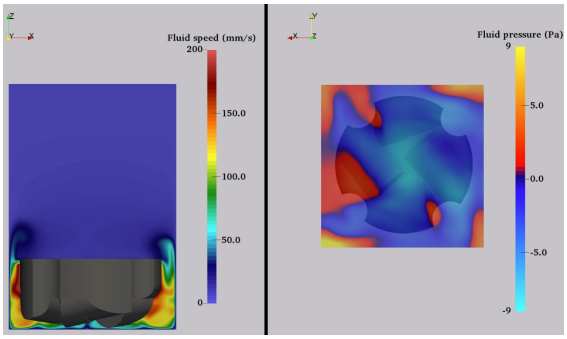

(a) CFD simulation of the hydrodynamic lubrication occuring at the tribosurface

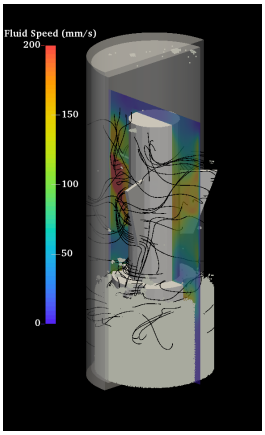

(b) Full scale uncoupled DEM-CFD

Figure 11.8: Simulation snapshots of drilling into concrete-like virtual rock in aqueous conditions

is shown in Fig. 11.9. It takes longer time to drill in the aqueous conditions than in the dry conditions. This finding is in agreement with the experimental results which are shown in Fig. 11.6 (also reproduced in the inset of Fig. 11.9).

11.4 Conclusions

To conclude, drilling experiments were carried out on two types of sandstones (Castlegate from the energy rich state of Texas and Crab Orchard from Tennessee) under dry and wet conditions. For experimental drilling under dry conditions, the rate of penetration decreases as the WoB decreases. Similar results were predicted by the bonded DEM model for a weak concrete-like rock. For experimental drilling under wet conditions, the rate of penetration is lower, due to the possible lubricating action of the drilling fluid, when compared to that for the dry conditions. Similar results were predicted by the bonded DEM model for a weak concrete-like rock in

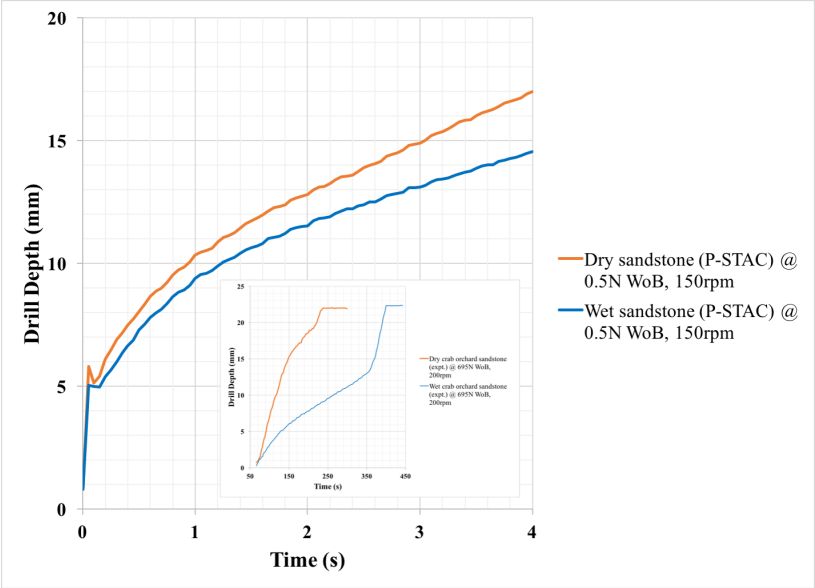

Figure 11.9: Virtual drilling into weak concrete-like rock: Dry and wet or lubricated conditions

concert with a full CFD to account for the hydrodynamic behavior of the drilling fluid trapped in the drill bit and rock interface.

Acknowledgements

Authors of this work would like to acknowledge the following contribution:

1. Joshua Wagner and Nicholas Wolf from Rice University for their help in conducting the drilling experiments

Part IV

Discussion

If I have seen future then it is by standing on the shoulders of great.
-Isaac Newton

Chapter 12

Conclusions

While tribology involves the study of friction, wear, and lubrication of interacting surfaces, the tribosurfaces are the pair of surfaces in sliding contact with a fluid (or particulate) media between. These tribosurfaces together with the intervening media is referred to as the tribosystem. The tribosurface interactions, due to the small length scales, are difficult to model for the physics of contact mechanics, particle dynamics and fluid dynamics, be it via theory, experiments or simulations. Each of this physics involves multiple attributes (e.g., particle size, shape, particle size distribution etc. for particle dynamics) which may or may not affect the behavior of a tribosurface. This thesis presents a synergistic approach which relies on benchtop experiments and modeling; it is comprised of high fidelity physics-based modeling (by including few and approximating the other physical attributes of the multiphysics) and machine learning enabled surrogate modeling, to extend the range of and provide engineering predictions for tribosurface interactions encountered in two key particle matrix industries: metal powder-bed additive manufacturing and energy resource rock drilling. While detailed conclusions for both of these

tribosystems were chalked out in Parts II and III, this chapter tries to summarize the findings of this thesis for the two aforementioned tribosurface interactions.

12.1 Conclusions: Powder spreadability in metal AM

The tribosystem encountered during the spreading step of the powder-bed additive manufacturing process which involves a sliding spreader (rolling and sliding for a roller), has been studied in Part II. The particulate media in this tribosurface is a metal AM powder which does not have a simple and a well-defined constitutive law. To understand the constitutive behavior of metal AM powders, detailed rheometry experiments have been conducted in Chapter 5. Powders which have smooth and large sized spherical particles spread better, indicated by a lower basic flowability energy (BFE) recorded by the rheometer, than those having fine, cohesive particles and irregular shapes. A distinction is made between the flowability and the spreadability of metal powders. It is necessary to understand the flowability of a metal powder under gravimetric loading (flow of a powder out of a storage hopper) and its spreadability under a confined, compressive loading (under a spreader) to better control the uniformity of the spread layer. Owing to the difficulty of studying the spreadability of metal AM powders experimentally, a high-fidelity GPU-based Computational Powder Dynamics (CPD) model has been developed in Chapter 6, based on the industry gold standard of the Discrete Element Method (DEM). A robust DEM calibration technique which makes use of the rheometry findings from Chapter 5 has been presented in Chapter 6 to generate, what is referred to as a virtual avatar of an industry grade AM powder (100-250μm Ti-6Al-4V) as a collection of 1.2 million, uniformly sized (250μm), spherical DEM particles. A state of the

art scheme to detect collisions between DEM particles and solid geometries in introduced and successfully applied to conduct virtual spreading on real substrates in Chapter 7. An added attribute of particle dynamics, namely particle size distribution (PSD) has been accounted for in Chapter 8 to obtain a higher fidelity virtual avatar of the same Ti-6Al-4V powder, but now as a collection of spherical particles with normally distributed particles sizes. Additionally, in Chapter 8, a retrofit to an ExOne Innovent 3D printer has been designed and additively manufactured in plastic to experimentally study the spread of Ti-6Al-4V powder over the surface of a spread coupon (a cuboid) 3D printed using Ti-6Al-4V. Experimental findings suggest that a virtual avatar of AM powder which incorporates PSD is able to better predict the spreading behavior than the one which models the virtual avatar as a collection of uniformly sized spheres.

12.2 Conclusions: Energy resource rock drilling

The tribosystem encountered during the drilling of energy resource rocks which involves a rotary and impacting contact of the drill bit with the rock formation in the presence of drilling fluids has been studied in Part III. This tribosystem involves sliding surfaces with fluid (drilling mud) and particulate (intact and drilled rock particles) media. Again, like the AM tribosurface interactions, the particulate media, viz. the rock formation being drilled into, does not have a simple and a well-defined constitutive law. An index test detailed in ASTM D 5731-16 [93], namely the point load strength test, which involves crushing of rocks of any shape and size using conical plates, has been described as the best suited characterization test while trying to model a rock using bonded particle DEM model in Chapter 10, as this test

can be performed using realistic particle counts. Chapter 10 also presents a model to generate weak concrete-like virtual rock which can be thought of as a representative sandstone comprising of 265,000 uniformly sized, spherical particles or grains with a diameter of 500μm. A prior 3D CFD solver, developed in the lab of Prof. Higgs, based on finite differencing technique of discretization along with relatively less known Immersed Boundary Method (IBM) to treat the immersed solids has been upgraded to work with graded mesh (non-uniform and locally refined Cartesian mesh) and shown to produce promising results in the studies of flow past cylinder and fluid film lubrication. Benchtop drilling experiments have been carried out on two sandstones (Castlegate sandstone from the energy rich state of Texas and Crab Orchard sandstone from Tennessee) in Chapter 11. In the same chapter, Virtual drilling has been carried out on the weak concrete-like virtual rock avatar developed in Chapter 10. The experimental findings revealed that the rate of penetration (RoP) of the drill bit is directly proportional to the weight on bit (WoB) and the drilling in dry conditions results in a higher RoP than the one which involved the use of water as drilling fluid. The bonded DEM + CFD model was able to predict both these findings but only qualitatively.

Art is never finished, only abandoned.
-Leonardo Da Vinci

Chapter 13

Future Work

While the possibility to apply the in-house, multi-purpose and multiphysics software Particle-Surface Tribology Analysis Code (P-STAC) to study myriad particle flow and tribology problems has no limits, this chapter lists down few specific additions to P-STAC which a new PhD student can ponder over.

13.1 Future Work: Powder spreadability in metal AM

Project 1: Incorporating the physics of particle cohesion in the DEM module of P-STAC

The model seems to under predict the BFE response of the calibrated particulate media in a virtual rheometer as well as the mass of powder in the sampling region in a virtual spread, at lower speeds of impeller blade and spreader respectively. This can be attributed to the predominance of cohesive forces at these lower impact speeds. Thus, the very first addition to the DEM module of P-STAC can be a cohesion model.

Project 2: Finding a spreader shape which best spreads the AM powder of interest

Apart from spreader speeds, another important factor which determines the spread layer properties is the shape of the spreader. Even though in thesis P-STAC was only used to study the effect of spreader speeds, the framework of Particle Tessellated Surface Interaction Scheme (refer Chapter 7) is general enough to be used to study the effect of spreader shape as shown in Fig. 13.1. A spreader can be manufactured to have a sinusoidal macroscopic roughness (as seen in the lowermost spreader in Fig. 13.1) and the pitch and amplitude of this sinusoidal roughness can be optimized to produce the best spread layer by generating a neural network similar to the ones introduced in Chapters 7 and 8.

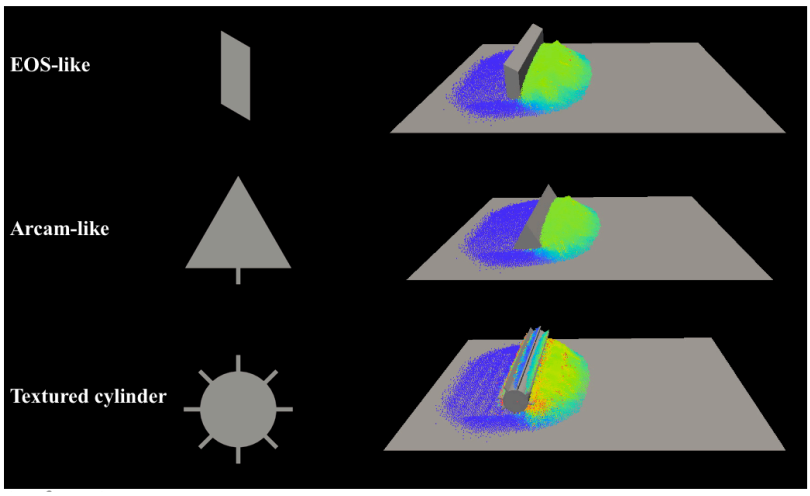

Figure 13.1: Effect of spreader shape on *spreadability* of AM powder

Project 3: Incorporating ALL the attributes of particle dynamics and then determining the most important ones

Further down the line, a PhD student can develop a DEM module which can account for ALL the attributes encountered in the physics of particle dynamics (refer Fig. 4.2) and train a problem-dependent neural network which has all these attributes as input nodes and bulk behavior of the particulate media as the output nodes. A feature selection study using this neural network can help to decipher the most important attributes which must be considered while providing engineering predictions for the problem at hand. P-STAC can then be used to generate higher-fidelity process maps (similar to but better than the ones in Chapters 7 and 8) using only these most important attributes of the physics of particle dynamics.

Project 4: Finding the particle size distribution (PSD) which results in the best spread layers

A 3D printer company usually expresses a tight control on particle sizes and shapes of powder which can be used to build parts, thereby making the production costs of these powders exorbitantly high as the powder manufacturer needs to have a tighter quality control, thus maybe discarding a lot of powder. P-STAC can be used to back-engineer a new powder which has larger particle sizes with larger spread in the PSD and possibly lesser constraints on the particle sizes which can be used in a 3D printer. This is possible if the powder with new PSD can be shown to spread well (viz. has desirable layer properties which were introduced in Chapter 7). This project can help the powder manufacturer to produce spreadable powders for cheap and sell for less compared to existing powders but still make bigger profits. One

way to do this is to introduce a third input node of *PSD* in the neural networks introduced in Chapters 7 and 8.

Project 5: Experiments relating Spreading process to the final part properties using machine learning

A Design of Experiments (DoE), as introduced in Appendix A, can be conducted to see the impact of spreading layers at different spreader speeds on the final 3D printed part.

13.2 Future Work: Energy resource rock drilling

Project 1: Incorporating the parallel bond model in the DEM module of P-STAC

The bonded DEM model developed in this study is different from the parallel bond model proposed by Potyondy and Cundall in 2004 [53]. It will be a good exercise, in future, to compare the present bonded DEM model with the parallel bond model. The shortcoming of the current model, even though highly parallelized using GPU, to extract micro-parameters (of contact model and bonds) which can result in the real world macro-properties (like the point load strength) is partly due to the much lower time step required by such micro-parameters.

Project 2: Faster and better treatment of fluid-structure interactions

CPU-based CFD with graded mesh and IBM which was developed in this thesis can be upgraded to run on a GPU. The CFD module of P-STAC can be expanded

to account for turbulence as this is mostly the flow regime during rock drilling. A non-Newtonian treatment of computational fluids can also be explored.

Project 3: Better treatment of fluid-particle-structure interactions and incorporating wear

A fully two-way coupled CFD + CPD + IBM will be the gold standard required to properly elucidate the phenomena occurring during rock drilling. Wear of drill bit was not accounted for in this thesis. A wear model can be useful when the aforementioned physics of non-Newtonian and turbulent flows has been accounted for in the best possible way, to predict the lifetime of the drill bit.

Project 4: Upgrading the Lagrangian treatment of virtual rocks to an Eulerian-Lagrangian representation

In future, a PhD student can explore the option of an approach called Finite-Discrete Element Method (to model a rock formation) which selectively treats the simulation domain as a continuum or discrete media, based on the local stress intensities [103]. Such a model will always be faster than a model which treats the entire rock formation as a discrete media, as was done in this thesis.

Part V

Supporting Material

Appendices

I don't want to hear the specials. If they're so special, put 'em on the menu.
-Jerry Seinfeld

Appendix A

Experiments relating the spreading process to the final part properties

Figure A.1 shows a possible overview figure of spreading and printing experiments. In this work, a simple CAD geometry like a cuboid was 3D printed at various spreader speeds and part orientation. The goal is to experimentally develop a spreading process map relating spreader speeds (U and ω) and part orientation (θ) to the properties of the green part like part deformation (i.e. the deviation of the printed cuboid from the input CAD geometry), surface roughness and the throughput of the print job or in other words efficiency of the print job.

Such a Design of Experiments (DoE) with only 5 variations per input variable can result in hundreds of cubes and keeping track of almost identical looking cubes can easily get chaotic. So a novel way, made possible only due to 3D printing, was

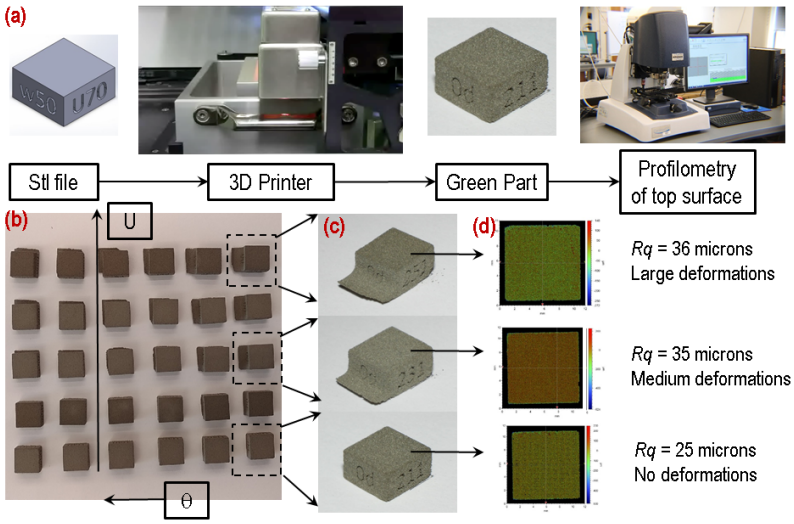

Figure A.1: (a) In the 3D printing process, a CAD file (e.g., a cuboid) of the 3D geometry is input to the 3D printer. The printer directly produces the 'green" solid part. In the case of binder jet printing the 'green" part is pre-sintering. (b) A battery of spreading and printing experiments are conducted where parameters such as the linear speed of spreader U, and rotational speed ω (not shown) and orientation of the cuboid θ with respect to spreader's linear speed are varied and extracted for inspection. (c) and (d) Final part inspection. Extracted parts from the printer bed are inspected using surface metrology (e.g., roughness) and microscopy (e.g., porosity, shape defects).

used to generate a 3-digit *fingerprint* of the cube. This *fingerprint* which was a vector for numbered value $\{\omega$,U,$\theta\}$ was 3D printed on one side of the cube with details of individual parameters on the remaining three sides. ω had values in rpm of $\{200, 150, 100, 50, 0, -50, -100, -150, -200\}$, U had values in mm/s of $\{20, 40, 60, 80, 100\}$ and θ had values of $\{0°, 15°, 30°, 45°, 60°, 75°\}$. So for examples, if ω is 150rpm, U is 20mm/s, and the orientation is parallel to the direction of spread ($\theta = 0°$), then the fingerprint of the cuboid is $\{211\}$ as seen on the lowermost cube in Fig. A.1. An unpacked identity of this cube can be found on the remaining three sides as w150, U20 and 0d respectively.

These green cuboids can then be studied for three properties namely part deformation, surface roughness and throughput of the print job. Once these prints and corresponding measurements will be done then machine learning via back propagation neural network (BP-NN), as the ones used in Chapters 7 and 8, can be employed to interpolate between the data points to obtain the desired maps relating experimental spreader speeds to final 3D printed part properties.

Bibliography

[1] J. Williams, *Engineering tribology*. Cambridge University Press, 2005.

[2] P. Dougherty, "Synthesizing in situ friction and wear with ex situ surface metrology to provide post-mortem tribological analysis: Experiments and modeling," Ph.D. dissertation, Carnegie Mellon University, 2016.

[3] M. C. Marinack Jr, "Sheared granular material: Single and multi-particle experiments and physics-based cellular automata modeling," Ph.D. dissertation, Carnegie Mellon University, 2013.

[4] J. N. Mpagazehe, "A physics-based, eulerian-lagrangian computational modeling framework to predict particle flow and tribological phenomena," Ph.D. dissertation, Carnegie Mellon University, 2013.

[5] G. Srivastava, "A macro-scale, tribological modeling framework for simulating multiple lubrication regimes and engineering applications," Ph.D. dissertation, Carnegie Mellon University, 2015.

[6] K. M. Warren, "Passive mechanical lysis of bioinspired systems: Computational modeling and microfluidic experiments," Ph.D. dissertation, Carnegie Mellon University, 2016.

[7] W. E. Frazier, "Metal additive manufacturing: a review," *Journal of Materials Engineering and Performance*, vol. 23, no. 6, pp. 1917–1928, 2014.

[8] D. Gu, W. Meiners, K. Wissenbach, and R. Poprawe, "Laser additive manufacturing of metallic components: materials, processes and mechanisms," *International materials reviews*, vol. 57, no. 3, pp. 133–164, 2012.

[9] A. Strondl, O. Lyckfeldt, H. Brodin, and U. Ackelid, "Characterization and control of powder properties for additive manufacturing," *Jom*, vol. 67, no. 3, pp. 549–554, 2015.

[10] J. Clayton, "Optimising metal powders for additive manufacturing," *Metal Powder Report*, vol. 69, no. 5, pp. 14–17, 2014.

[11] R. Freeman, "Measuring the flow properties of consolidated, conditioned and aerated powdersa comparative study using a powder rheometer and a rotational shear cell," *Powder Technology*, vol. 174, no. 1, pp. 25–33, 2007.

[12] X. Fu, D. Huck, L. Makein, B. Armstrong, U. Willen, and T. Freeman, "Effect of particle shape and size on flow properties of lactose powders," *Particuology*, vol. 10, no. 2, pp. 203–208, 2012.

[13] M. Qian and F. H. Froes, *Titanium Powder Metallurgy: Science, Technology and Applications*. Butterworth-Heinemann, 2015.

[14] K. Rietema, *The dynamics of fine powders*. Springer Science & Business Media, 2012.

[15] C. Silethelwe, L. M. Mahlatji, and H. K. Chikwanda, "Characterisation of titanium powder flow, shear and bulk properties using the ft4 powder rheometer." *Advanced Materials Research*, no. 1019, 2014.

[16] A. Cooke and J. Slotwinski, *Properties of metal powders for additive manufacturing: a review of the state of the art of metal powder property testing*. US Department of Commerce, National Institute of Standards and Technology, 2012.

[17] M. Leturia, M. Benali, S. Lagarde, I. Ronga, and K. Saleh, "Characterization of flow properties of cohesive powders: a comparative study of traditional and new testing methods," *Powder Technology*, vol. 253, pp. 406–423, 2014.

[18] R. Bharadwaj, W. R. Ketterhagen, and B. C. Hancock, "Discrete element simulation study of a freeman powder rheometer," *Chemical Engineering Science*, vol. 65, no. 21, pp. 5747–5756, 2010.

[19] H. Tang, M. Qian, N. Liu, X. Zhang, G. Yang, and J. Wang, "Effect of powder reuse times on additive manufacturing of ti-6al-4v by selective electron beam melting," *Jom*, vol. 67, no. 3, pp. 555–563, 2015.

[20] S. H. Huang, P. Liu, A. Mokasdar, and L. Hou, "Additive manufacturing and its societal impact: a literature review," *The International Journal of Advanced Manufacturing Technology*, pp. 1–13, 2013.

[21] P. A. Cundall and O. D. Strack, "A discrete numerical model for granular assemblies," *geotechnique*, vol. 29, no. 1, pp. 47–65, 1979.

[22] R. Bharadwaj *et al.*, "Using dem to solve bulk material handling problems," *Chemical Engineering Progress*, vol. 108, no. 9, pp. 54–58, 2012.

[23] C. Hare, U. Zafar, M. Ghadiri, T. Freeman, J. Clayton, and M. Murtagh, "Analysis of the dynamics of the ft4 powder rheometer," *Powder Technology*, vol. 285, pp. 123–127, 2015.

[24] S. Wilkinson, S. Turnbull, Z. Yan, E. H. Stitt, and M. Marigo, "A parametric evaluation of powder flowability using a freeman rheometer through statistical and sensitivity analysis: A discrete element method (dem) study," *Computers & Chemical Engineering*, vol. 97, pp. 161–174, 2017.

[25] M. Yan, S. Wilkinson, S. Turnbull, E. Stitt, and M. Marigo, "Parametric evaluation for powder flowability using a freeman rheometer: a discrete element method study," *Crossroads Part. Sci. Technol*, 2015.

[26] Z. Yan, S. K. Wilkinson, E. H. Stitt, and M. Marigo, "Investigating mixing and segregation using discrete element modelling (dem) in the freeman ft4 rheometer," *International journal of pharmaceutics*, vol. 513, no. 1, pp. 38–48, 2016.

[27] C. Coetzee, "Calibration of the discrete element method," *Powder Technology*, 2017.

[28] W. Nan, M. Ghadiri, and Y. Wang, "Analysis of powder rheometry of ft4: Effect of particle shape," *Chemical Engineering Science*, vol. 173, pp. 374–383, 2017.

[29] A. Di Renzo and F. P. Di Maio, "Comparison of contact-force models for the simulation of collisions in dem-based granular flow codes," *Chemical engineering science*, vol. 59, no. 3, pp. 525–541, 2004.

[30] S. Green, "Particle simulation using cuda," *NVIDIA whitepaper*, vol. 6, pp. 121–128, 2010.

[31] L. Hu, G. Hu, Z. Fang, and Y. Zhang, "A new algorithm for contact detection between spherical particle and triangulated mesh boundary in discrete element method simulations," *International Journal for Numerical Methods in Engineering*, vol. 94, no. 8, pp. 787–804, 2013.

[32] C. Passerello, "Interference detection using barycentric coordinates," *Mechanics Research Communications*, vol. 9, no. 6, pp. 373–378, 1982.

[33] M. Asadi-Eydivand, M. Solati-Hashjin, A. Fathi, M. Padashi, and N. A. A. Osman, "Optimal design of a 3d-printed scaffold using intelligent evolutionary algorithms," *Applied Soft Computing*, vol. 39, pp. 36–47, 2016.

[34] H. Chen and Y. F. Zhao, "Learning algorithm based modeling and process parameters recommendation system for binder jetting additive manufacturing process," in *ASME 2015 International Design Engineering Technical Conferences and Computers and Information in Engineering Conference*. American Society of Mechanical Engineers, 2015, pp. V01AT02A029–V01AT02A029.

[35] Z. Jiang, Y. Liu, H. Chen, and Q. Hu, "Optimization of process parameters for biological 3d printing forming based on bp neural network and genetic algorithm." in *ISPE CE*, 2014, pp. 351–358.

[36] G. Tourloukis, S. Stoyanov, T. Tilford, and C. Bailey, "Predictive modelling for 3d inkjet printing processes," in *Electronics Technology (ISSE), 2016 39th International Spring Seminar on*. IEEE, 2016, pp. 257–262.

[37] K. D. Lyons, S. Honeygan, and T. Mroz, "Netl extreme drilling laboratory studies high pressure high temperature drilling phenomena," *Journal of Energy Resources Technology*, vol. 130, no. 4, p. 043102, 2008.

[38] K. Terzaghi, R. B. Peck, and G. Mesri, *Soil mechanics in engineering practice*. John Wiley & Sons, 1996.

[39] F. Appl, C. C. Wilson, and I. Lakshman, "Measurement of forces, temperatures and wear of pdc cutters in rock cutting," *Wear*, vol. 169, no. 1, pp. 9–24, 1993.

[40] P. S. Dougherty, R. Pudjoprawoto, and C. F. Higgs, "Bit cutter-on-rock tribometry: analyzing friction and rate-of-penetration for deep well drilling substrates," *Tribology International*, vol. 77, pp. 178–185, 2014.

[41] P. S. Dougherty, J. Mpagazehe, J. Shelton, and C. F. Higgs III, "Elucidating pdc rock cutting behavior in dry and aqueous conditions using tribometry," *Journal of Petroleum Science and Engineering*, vol. 133, pp. 529–542, 2015.

[42] J. N. Mpagazehe, A. F. Queiruga, and C. F. Higgs, "Towards an understanding of the drilling process for fossil fuel energy: A continuum-discrete approach," *Tribology International*, vol. 59, pp. 273–283, 2013.

[43] N. Rafatian, S. Z. Miska, L. W. Ledgerwood, M. Yu, R. Ahmed, N. E. Takach *et al.*, "Experimental study of mse of a single pdc cutter interacting with

rock under simulated pressurized conditions," *SPE Drilling & Completion*, vol. 25, no. 01, pp. 10–18, 2010.

[44] R. Teale, "The concept of specific energy in rock drilling," in *International Journal of Rock Mechanics and Mining Sciences & Geomechanics Abstracts*, vol. 2. Elsevier, 1965, pp. 57–73.

[45] E. Broch and J. Franklin, "The point-load strength test," in *International Journal of Rock Mechanics and Mining Sciences & Geomechanics Abstracts*, vol. 9. Elsevier, 1972, pp. 669–676.

[46] L. E. Vallejo, "Fissure parameters in stiff clays under compression," *Journal of geotechnical engineering*, vol. 115, no. 9, pp. 1303–1317, 1989.

[47] S. Lobo-Guerrero and L. E. Vallejo, "Discrete element method evaluation of granular crushing under direct shear test conditions," *Journal of Geotechnical and Geoenvironmental Engineering*, vol. 131, no. 10, pp. 1295–1300, 2005.

[48] S. Lobo-Guerrero, L. E. Vallejo, and L. F. Vesga, "Visualization of crushing evolution in granular materials under compression using dem," *International Journal of Geomechanics*, vol. 6, no. 3, pp. 195–200, 2006.

[49] Z. Bieniawski, "The point-load test in geotechnical practice," *Engineering Geology*, vol. 9, no. 1, pp. 1–11, 1975.

[50] S.-Q. Yang and H.-W. Jing, "Strength failure and crack coalescence behavior of brittle sandstone samples containing a single fissure under uniaxial compression," *International Journal of Fracture*, vol. 168, no. 2, pp. 227–250, 2011.

[51] A. Bobet, "Numerical methods in geomechanics," *The Arabian Journal for Science and Engineering*, vol. 35, no. 1B, pp. 27–48, 2010.

[52] P. A. Cundall and R. D. Hart, "Development of generalized 2-d and 3-d distinct element programs for modeling jointed rock," ITASCA CONSULTING GROUP INC MINNEAPOLISMN, Tech. Rep., 1985.

[53] D. Potyondy and P. Cundall, "A bonded-particle model for rock," *International journal of rock mechanics and mining sciences*, vol. 41, no. 8, pp. 1329–1364, 2004.

[54] P. L. Menezes, M. R. Lovell, I. V. Avdeev, and C. F. Higgs, "Studies on the formation of discontinuous rock fragments during cutting operation," *International Journal of Rock Mechanics and Mining Sciences*, vol. 71, pp. 131–142, 2014.

[55] J. Rojek, E. Onate, C. Labra, and H. Kargl, "Discrete element simulation of rock cutting," *International Journal of Rock Mechanics and Mining Sciences*, vol. 48, no. 6, pp. 996–1010, 2011.

[56] L. F. Vesga, L. E. Vallejo, and S. Lobo-Guerrero, "Dem analysis of the crack propagation in brittle clays under uniaxial compression tests," *International journal for numerical and analytical methods in geomechanics*, vol. 32, no. 11, pp. 1405–1415, 2008.

[57] J. S. Mendoza, "Modelling deformation, porosity and elastic constants in porous rocks," Ph.D. dissertation, Stanford University, 1987.

[58] B. Joodi, M. Sarmadivaleh, V. Rasouli, and A. Nabipour, "Simulation of the cutting action of a single pdc cutter using dem," *WIT Transactions on Engineering Sciences*, vol. 81, pp. 143–150, 2012.

[59] L. A. Endres, "Computation modeling of drill bits: A new method for reproducing bottom hole geometry and a second-order explicit integrator via composition for coupled rotating rigid bodies," Ph.D. dissertation, University of California, San Diego, 2007.

[60] M. Griebel, T. Dornseifer, and T. Neunhoeffer, *Numerical simulation in fluid dynamics: a practical introduction*. SIAM, 1998.

[61] S. Marina, E. K. Imo-Imo, I. Derek, P. Mohamed, and S. Yong, "Modelling of hydraulic fracturing process by coupled discrete element and fluid dynamic methods," *Environmental Earth Sciences*, vol. 72, no. 9, pp. 3383–3399, 2014.

[62] S. Levasseur, Y. Malécot, M. Boulon, and E. Flavigny, "Soil parameter identification using a genetic algorithm," *International Journal for Numerical and Analytical Methods in Geomechanics*, vol. 32, no. 2, pp. 189–213, 2008.

[63] F. Meulenkamp and M. A. Grima, "Application of neural networks for the prediction of the unconfined compressive strength (ucs) from equotip hardness," *International Journal of rock mechanics and mining sciences*, vol. 36, no. 1, pp. 29–39, 1999.

[64] V. Singh, D. Singh, and T. Singh, "Prediction of strength properties of some schistose rocks from petrographic properties using artificial neural networks,"

International Journal of Rock Mechanics and Mining Sciences, vol. 38, no. 2, pp. 269–284, 2001.

[65] Y. Yang and M. Rosenbaum, "The artificial neural network as a tool for assessing geotechnical properties," *Geotechnical and Geological Engineering*, vol. 20, no. 2, pp. 149–168, 2002.

[66] A. Bhatnagar and M. Khandelwal, "An intelligent approach to evaluate drilling performance," *Neural Computing and Applications*, vol. 21, no. 4, pp. 763–770, 2012.

[67] Y. K. Gidh, H. Ibrahim, A. Purwanto *et al.*, "Real-time drilling parameter optimization system increases rop by predicting/managing bit wear," in *SPE Digital Energy conference and Exhibition*. Society of Petroleum Engineers, 2011.

[68] B. Pichler, R. Lackner, and H. A. Mang, "Soft-computing-based parameter identification as the basis for prognoses of the structural behaviour of tunnels," in *Numerical simulation in tunnelling*. Springer, 2003, pp. 201–223.

[69] C. M. Bishop, *Pattern recognition and machine learning*. springer, 2006.

[70] K. V. Wong and A. Hernandez, "A review of additive manufacturing," *ISRN Mechanical Engineering*, vol. 2012, 2012.

[71] J. Gockel, J. Beuth, and K. Taminger, "Integrated control of solidification microstructure and melt pool dimensions in electron beam wire feed additive manufacturing of ti-6al-4v," *Additive Manufacturing*, vol. 1, pp. 119–126, 2014.

[72] J. Beuth, J. Fox, J. Gockel, C. Montgomery, R. Yang, H. Qiao, E. Soylemez, P. Reeseewatt, A. Anvari, S. Narra *et al.*, "Process mapping for qualification across multiple direct metal additive manufacturing processes," in *Proceedings of SFF Symposium., Austin, TX, Aug*, 2013, pp. 655–665.

[73] J.-A. Ferrez, "Dynamic triangulations for efficient 3d simulation of granular materials," Master's thesis, EPFL, 2001.

[74] J.-A. Ferrez and T. M. Lieblin3g, "Dynamic triangulations for efficient detection of collisions between spheres with applications in granular media simulations," *Philosophical Magazine B*, vol. 82, no. 8, pp. 905–929, 2002.

[75] B. Mishra and C. Murty, "On the determination of contact parameters for realistic dem simulations of ball mills," *Powder Technology*, vol. 115, no. 3, pp. 290–297, 2001.

[76] C. Coetzee and D. Els, "Calibration of discrete element parameters and the modelling of silo discharge and bucket filling," *Computers and electronics in agriculture*, vol. 65, no. 2, pp. 198–212, 2009.

[77] C. Coetzee, "Calibration of the discrete element method and the effect of particle shape," *Powder Technology*, vol. 297, pp. 50–70, 2016.

[78] S. Cook, *CUDA programming: a developer's guide to parallel computing with GPUs*. Newnes, 2012.

[79] M. Ucgul, J. M. Fielke, and C. Saunders, "Three-dimensional discrete element modelling of tillage: Determination of a suitable contact model and

parameters for a cohesionless soil," *Biosystems Engineering*, vol. 121, pp. 105–117, 2014.

[80] P. Frankowski and M. Morgeneyer, "Calibration and validation of dem rolling and sliding friction coefficients in angle of repose and shear measurements," in *AIP Conference Proceedings*, vol. 1542, no. 1. AIP, 2013, pp. 851–854.

[81] E. Hoek and J. D. Bray, *Rock slope engineering*. CRC Press, 1981.

[82] W. Zhang, A. Mehta, P. S. Desai, and C. F. Higgs III, "Machine learning enabled powder spreading process map for metal additive manufacturing (am)," in *Proceedings of SFF Symposium., Austin, TX, Aug*, 2017, pp. 1235–1249.

[83] E. Herbold, O. Walton, and M. Homel, "Simulation of powder layer deposition in additive manufacturing processes using the discrete element method," Lawrence Livermore National Lab.(LLNL), Livermore, CA (United States), Tech. Rep., 2015.

[84] S. Haeri, Y. Wang, O. Ghita, and J. Sun, "Discrete element simulation and experimental study of powder spreading process in additive manufacturing," *Powder Technology*, vol. 306, pp. 45–54, 2017.

[85] E. J. Parteli and T. Pöschel, "Particle-based simulation of powder application in additive manufacturing," *Powder Technology*, vol. 288, pp. 96–102, 2016.

[86] H. Mindt, M. Megahed, N. Lavery, M. Holmes, and S. Brown, "Powder bed layer characteristics: the overseen first-order process input," *Metallurgical and Materials Transactions A*, vol. 47, no. 8, pp. 3811–3822, 2016.

[87] C. Ho and Y. Lee, "Temperature fields in the fusion zone induced by a moving electron beam," *Journal of mechanical science and technology*, vol. 21, no. 10, pp. 1707–1713, 2007.

[88] I. Basheer and M. Hajmeer, "Artificial neural networks: fundamentals, computing, design, and application," *Journal of microbiological methods*, vol. 43, no. 1, pp. 3–31, 2000.

[89] S. P. Moylan, J. A. Slotwinski, A. Cooke, K. Jurrens, and M. A. Donmez, "Lessons learned in establishing the nist metal additive manufacturing laboratory," *NIST Technical Note*, 2013.

[90] J. D. Hamilton, "Understanding crude oil prices," National Bureau of Economic Research, Tech. Rep., 2008.

[91] J. M. Griffin and D. J. Teece, *OPEC behaviour and world oil prices*. Routledge, 2016.

[92] J. Baffes, M. A. Kose, F. Ohnsorge, and M. Stocker, "The great plunge in oil prices: Causes, consequences, and policy responses," 2015.

[93] D5731-16, "Standard test method for determination of the point load strength index of rock and application to rock strength classifications," ASTM International, West Conshohocken, PA, Standard, 2016.

[94] O. Reynolds, "On the theory of lubrication and its application to mr. beauchamp tower's experiments, including an experimental determination of the viscosity of olive oil." *Proceedings of the Royal Society of London*, vol. 40, no. 242-245, pp. 191–203, 1886.

[95] E. Sanmiguel-Rojas, J. Ortega-Casanova, C. del Pino, and R. Fernandez-Feria, "A cartesian grid finite-difference method for 2d incompressible viscous flows in irregular geometries," *Journal of Computational Physics*, vol. 204, no. 1, pp. 302–318, 2005.

[96] C. S. Peskin, "The immersed boundary method," *Acta numerica*, vol. 11, pp. 479–517, 2002.

[97] A. Roshko, "On the drag and shedding frequency of two-dimensional bluff bodies," 1954.

[98] M. Hammache and M. Gharib, "An experimental study of the parallel and oblique vortex shedding from circular cylinders," *Journal of Fluid Mechanics*, vol. 232, pp. 567–590, 1991.

[99] C. Williamson, "Oblique and parallel modes of vortex shedding in the wake of a circular cylinder at low reynolds numbers," *Journal of Fluid Mechanics*, vol. 206, pp. 579–627, 1989.

[100] J. Park, K. Kwon, and H. Choi, "Numerical solutions of flow past a circular cylinder at reynolds numbers up to 160," *Journal of Mechanical Science and Technology*, vol. 12, no. 6, pp. 1200–1205, 1998.

[101] A. L. E. Silva, A. Silveira-Neto, and J. Damasceno, "Numerical simulation of two-dimensional flows over a circular cylinder using the immersed boundary method," *Journal of Computational Physics*, vol. 189, no. 2, pp. 351–370, 2003.

[102] M. Nishioka and H. Sato, "Mechanism of determination of the shedding frequency of vortices behind a cylinder at low reynolds numbers," *Journal of Fluid Mechanics*, vol. 89, no. 1, pp. 49–60, 1978.

[103] A. A. Munjiza, *The combined finite-discrete element method*. John Wiley & Sons, 2004.